

Fabrication and Properties of Novel Hybrid Thermoelectric Materials

Yanan Wang

July 2022

Fabrication and Properties of Novel Hybrid Thermoelectric
Materials

Yanan Wang

Doctoral Program in Materials Science and Engineering

Submitted to the Graduate School of
Pure and Applied Sciences
in Partial Fulfillment of the Requirements
for the Degree of Doctor of Philosophy in
Engineering

at the

University of Tsukuba

Acknowledgement

My study at University of Tsukuba and National Institute for Materials Science is drawing to a close. Looking back on the past, it is full of memories. I wish to express my sincere appreciation to all those who have offered me invaluable help and warm care during the three years of my doctoral study here.

First, I would like to express my heartfelt gratitude to my supervisor, Professor Takao Mori. He has offered me valuable ideas, suggestions and criticisms with profound knowledge and rich research experience. His patience and kindness are greatly appreciated. Not only the selfless encouragement and guidance in scientific research, he also gave me meticulous concern in my life. His serious scientific attitude, realistic spirit of learning, and professional ethics have deeply infected me and become an example for me to learn from all my life.

Second, I should give my hearty thanks to all my group members for their unselfish assistance and meticulous guidance. Thanks for the wonderful serendipity to brought us together to laugh, grow and forge ahead, and every moment of getting along with each other has been turned into eternal memories. I wish you have a bright future.

Third, I want to express my gratitude to the members of PhD committee, Prof. Sakurai Takeaki, Prof. Takeuchi Masayuki, and Prof. Ishii Satishi for their kind advices for the improvement of my PhD defense.

Lastly, my thanks would go to my beloved family for their thoughtfulness, understanding and encouragement for me all through these years. My gratitude will remain in my heart forever.

Yanan Wang at MANA 503

2022. 06. 21

Abstract

As one of the prominent energy harvesting technologies, thermoelectric (TE) devices are attracting increasing attention because its ability that realizing direct mutual conversion between thermal and electrical energy. TE device is usually constituted by n- and p-type legs (materials) in the connection way of electrical series and thermal parallel. Through the transport characteristics of carriers and phonons in thermoelectric materials, TE device can achieve power generation or refrigeration. Thus, developing TE materials with higher TE performance is a never-ending scientific perusing. On the other hand, TE devices have a series of advantages of small size, simple structure, no noise and emission-free, no moving parts and extra-maintenance, good reliability, fast response, long service life, etc., making themselves a promising application prospect in the industry and human life.

For power generation, Bi_2Te_3 -based bulk materials are still the most promising TE candidates at the room and low temperature range to date. For mid and high temperature range, most efforts are dedicating to the inorganic TE materials because of their excellent TE properties and high figure of merit (ZT). However, the development of inorganic TE materials is greatly limited due to the disadvantages of high preparation cost, complicated process, poor flexibility, rare resources and high price. On the other hand, with the ever-growing development of multifunctional and miniature electronics, powering the sensors in the future IoT (internet of things) society is one of important applications for thermoelectric materials as well as devices. Therefore, it requires that the TE materials and its devices are light and easy processability, which is as important as improving its performance. These requirements have stimulated a strong interest in the preparation of lightweight, non-toxic organic or composite flexible thermoelectric materials and devices using a simple and inexpensive solution method.

In this thesis, (1) we first report an n-type $\text{MoS}_2/\text{Bi}_2\text{Te}_3$ nanocomposites prepared by hydrothermal reaction combined with reactive electric field-assisted sintering method, the influence of phase integrity of $\text{MoS}_2/\text{Bi}_2\text{Te}_3$ nanocomposites on TE properties was investigated. The optimized hybrid exhibits a three-fold enhancement in ZT due to enhanced electrical conductivity without affecting Seebeck coefficient; (2) aiming to fabricate flexible TE materials constituted of Te free and less toxic, organic-inorganic hybrid strategy was adapted to fabricate flexible TE film constituted by abundant chalcopyrite, poly(3,4-ethylenedioxythiophene) polystyrenesulfonate (PEDOT:PSS), and graphene was fabricated and its prototype module was demonstrated; (3) to match the obtained n-type flexible TE leg for the flexible TE device, a p-type flexible $\text{Mg}_{0.99}\text{Cu}_{0.01}\text{Ag}_{0.97}\text{Sb}_{0.99}$ /graphene/PEDOT:PSS TE film was fabricated by a strategically-designed hybrid method.

Hybrid is an important method for designing and optimizing materials. The study of hybrid effect and mechanism of materials has important scientific interest, which also laid the foundation for the fabrication and application of thermoelectric devices.

Contents

Acknowledgement	I
Abstract.....	II
Chapter 1 Introduction.....	1
1.1 Thermoelectricity.....	1
1.2 Thermoelectric effects	2
1.2.1 Seebeck effect.....	2
1.2.2 Peltier effect.....	3
1.2.3 Thomson effect	4
1.2.4 Relation between Seebeck, Peltier and Thomson coefficients.....	5
1.3 The principles of thermoelectric device and evaluation parameters of thermoelectric performance.....	5
1.3.1 The principle of thermoelectric device	5
1.3.2 The evaluation parameters of thermoelectric performance.....	7
1.3.3 The interconnection between thermoelectric parameters.....	9
1.4 The progress in thermoelectric materials.....	9
1.4.1 Inorganic materials	9
1.4.2 Organic thermoelectric materials.....	17
Reference.....	28
Chapter 2 Fabrication and thermoelectric Properties of MoS₂/Bi₂Te₃ composites.....	35
2.1 Introduction	35
2.2 Experimental section	35
2.2.1 Synthesis of hexagonal nanoplatelets of Bi ₂ Te ₃ and Bi ₂ Te ₃ /MoS ₂ composites	35
2.2.2 Synthesis of Bi ₂ Te ₃ /X mol% MoS ₂ bulk samples.....	36
2.2.3 Chemical and structural characterization.....	37
2.2.4 Physical property measurements.....	37
2.3 Results and discussion	38
2.4 Summary.....	45
Reference.....	45
Chapter 3 Fabrication and TE Properties of <i>n</i>-Type Chalcopyrite/PEDOT:PSS/Graphene Hybrid Film	47
3.1 Introduction	47
3.2 Experimental section	48
3.2.1 Materials	48
3.2.2 Preparation of chalcopyrite powder	48

3.2.3 Fabrication of the binary chalcopyrite/PEDOT:PSS and ternary chalcopyrite/PEDOT:PSS/graphene films	49
3.3 Measurement and characterization	50
3.4 Results and discussion	50
3.5 Summary.....	62
Reference.....	63
Chapter 4 Fabrication and TE Properties of <i>p</i>-Type $\text{Mg}_{0.99}\text{Cu}_{0.01}\text{Ag}_{0.99}\text{Sb}_{0.97}$/graphene/PEDOT:PSS Hybrid Film	66
4.1 Introduction	66
4.2 Experimental method.....	68
4.2.1 Materials	68
4.2.2 Synthesis of $\text{Mg}_{0.99}\text{Cu}_{0.01}\text{Ag}_{0.97}\text{Sb}_{0.99}$ (MCAS) powder	68
4.2.3 Synthesis of $\text{Mg}_{0.99}\text{Cu}_{0.01}\text{Ag}_{0.97}\text{Sb}_{0.99}$ /graphene/PEDOT:PSS films	69
4.3 Measurement and characterization	70
4.4 Results and discussion	71
4.5 Summary.....	83
Reference.....	83
Chapter 5 Conclusion and outlook.....	88
5.1 Conclusion.....	88
5.2 Outlook	89
List of Publications.....	90

Chapter 1 Introduction

1.1 Thermoelectricity

The development and advancement of technology have made human life increasingly comfortable and intelligent, meanwhile which has put forward unprecedented demand for energy. However, the available utilizing energy produced by burning fossil fuels is only around 30-40%, whereas the rest is waste in the form of heat[1]. Besides, the traditional energy sources are exhausting and causing severe environmental trouble. Therefore, it is urgent to develop self-charging technologies to address these issues. Currently, various technologies have been developed to dynamically harvest energy from the surroundings to generate electrical power, such as piezoelectric, perovskite and thermoelectric (TE) energy harvester. As one of the prominent energy harvesting technologies, TE materials and its devices are attracting increasing attention.

On the one hand, TE devices are an important part of new energy development because of its ability that realizing direct mutual conversion between thermal and electric energy through the transport characteristics of carriers and phonons in thermoelectric materials[2-5]. On the other hand, TE devices have a small size, simple structure, no noise and emission-free, no moving parts and extra-maintenance, good reliability, fast response, long service life and a series of advantages, exhibiting promising application prospects in the industry and human life[6-10].

To date, most attention is attracted by the inorganic TE materials because of their excellent TE properties and high figure of merit (ZT)[3,11-15]. However, inorganic thermoelectric materials due to the disadvantages of high preparation cost, complicated process, poor flexibility, rare resources and high price, which greatly limit their development and wide application[1,16-18]. Besides, with the ever-growing development of multifunctional and miniature electronics, powering the sensors in the future IoT (internet of things) society is one of important applications for TE devices[1,9]. Therefore, developing light and easy-processable TE legs (materials) is as important as improving their performance. The requirements have stimulated a strong interest in the preparation of lightweight, non-toxic TE materials as well as devices by a simple and inexpensive solution method.

Recently, the TE properties of organic materials are widely studied due to they are lightweight, inexpensive, inherently flexible, and mass-fabricated by liquid phase methods, what is exactly lacking in the inorganic materials[19-23]. Furthermore, the thermal conductivity of the organic materials is in the range of 0.1 ~ 1 W/m K that is 1 to 2 orders of magnitude lower than inorganic materials, which is beneficial to obtain a high ZT [24]. Although the great progresses have been done, organic TE materials compared to the inorganic TE materials are still in the infant stage due to the poor TE performance, especially for n-type organic materials.

To realize high TE performance as well as good mechanical flexibility, the studies on an exploration of new materials systems combined with novel fabrication technologies and rational structure design are required.

1.2 Thermoelectric effects

Thermoelectric effect is a phenomenon by which a temperature difference is directly converted to electric voltage and vice versa. It includes *Seebeck effect*, *Peltier effect* and *Thomson effect*, which are closely linked by the *Kelvin relation*.

1.2.1 Seebeck effect

The first of thermoelectric effects was discovered in 1821 by *T.J. Seebeck*. As illustrated in **Figure 1.1 (a)**, a ΔV is generated between two nodes consisted of two different conductors (A and B) when a different temperature ($T_0, T_0 + \Delta T$) is applied on the nodes. Consequently, a current is produced in the circuit. This phenomenon is named *Seebeck effect*, which is mainly related to the carrier diffusion in the material. As shown in **Figure 1.1(b)**, the physical transport mechanism of carriers is illustrated: the different temperature at the ends of the material leads to the uneven distribution of carriers, based on this particular physical phenomenon, the ΔT will be directly converted into ΔV .

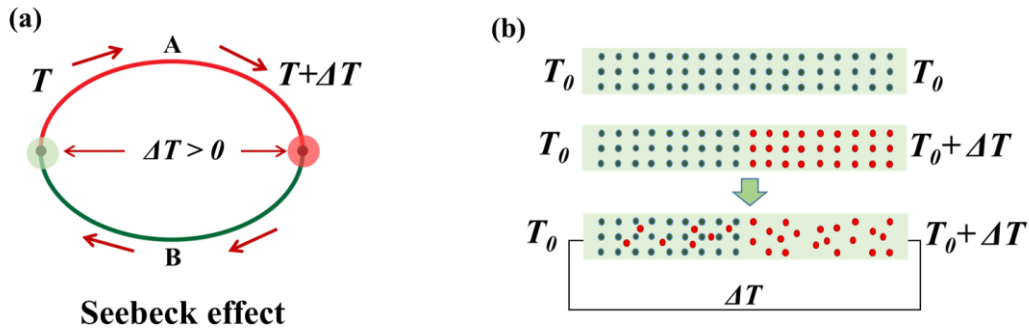


Figure 1.1 Schematic diagrams of (a) Seebeck effect and (b) the corresponding physical mechanism.

The relation between ΔV and ΔT between two ends is expressed as,

$$\Delta V = S_{AB} \Delta T \quad (1.1)$$

where S_{AB} is the differential Seebeck coefficient of the two conductors with the unit of $\mu\text{V/K}$, which is only related to the energy band structure of material. Moreover, ΔV is directional that depends on the intrinsic properties of two conductors and the direction of temperature gradient. When the ΔT is small, S_{AB} is expressed as,

$$S_{AB} = \lim_{\Delta T \rightarrow 0} \left(\frac{\Delta V}{\Delta T} \right) = \frac{dV}{dT} \quad (1.2)$$

As a result, the directional ΔV leads to directional S_{AB} determined as:

in the semiconductor,

(1) if the holes are the main carriers and thermoelectric current flows from semiconductor A to B at the cold end, $S_{AB} > 0$, and the semiconductor is named p-type.

(2) if the main carriers are electrons, the thermoelectric current flows from semiconductor B to A at the cold end, $S_{AB} < 0$, the semiconductor is named n-type.

1.2.2 Peltier effect

Peltier effect is the inverse process of *Seebeck effect*, which is discovered in the 1834 by a French scientist, C.A. Peltier, thus named as the *Peltier effect*. The definition is described as directly pumping heat by carriers (holes and/or electrons). As shown in **Figure 1.2a**, when a current is passed through circuit composed of two different conductors A and B, excepting the *Joule heat* is generated, the extra heat will be released or absorbed at these two junctions connecting A and B, which is called *Peltier heat*, and this phenomenon is called *Peltier effect*. It is experimental found that the *Peltier heat* is proportional to electric current, and the relation is expressed as

$$d_Q = I \pi_{AB} dt, \tag{1.3}$$

the Q , I , t , and π_{AB} denotes absorbed or released heat, current in the circuit, powering time, and differential Peltier coefficient with the unit of V. Similar to the directional S_{AB} , at the junctions, when current flows from conductor A to B, heat is absorbed, and π_{AB} is positive, conversely, it is negative. Apparently,

$$\pi_{AB} = -\pi_{BA} \tag{1.4}$$

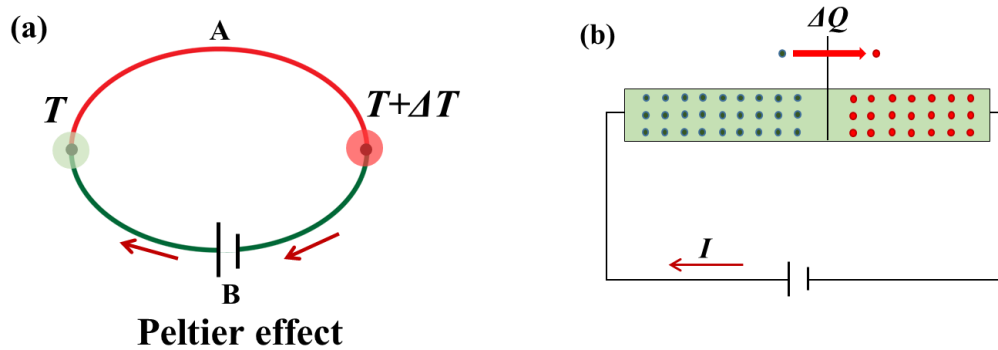


Figure 1.2 Schematic diagrams of (a) Peltier effect and (b) the corresponding physical mechanism

The mechanism of the *Peltier effect* is related to the difference in carrier concentration and Fermi energy levels of two conductors. **Figure 1.2(b)** is diagram of the physical mechanism of the *Peltier effect*. When two pieces of conductors with different Fermi levels are connected and an electric current is applied on this circuit, the carriers flow from one conductor to the other through the junction under the applied electric field. When carriers are transported (1) from a conductor with low Fermi energy level to a conductor with high Fermi energy level, at the interface, the

carriers have to exchange energy with lattice through thermal vibrations to absorb enough energy to pass the potential barrier generated by band bending, which macroscopically behaves as absorbing heat. (2) from a conductor with high Fermi energy level to a conductor with low Fermi energy level, the carriers with high energy will release energy at the contact interface through lattice vibrations, which macroscopically behaves as releasing heat.

1.2.3 Thomson effect

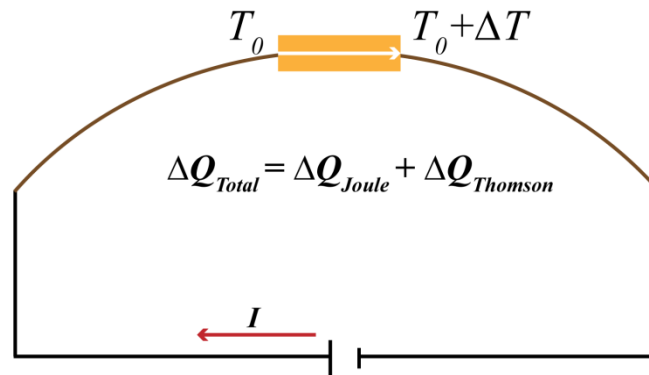


Figure 1.3 Schematic diagram of Thomson effect.

The *Seebeck effect* and the *Peltier effect* are both occurring in a circuit consisted of two different conductors, while the other thermoelectric conversion phenomenon presented in a single conductor is defined as *Thomson effect*. As the schematic diagram shown in **Figure 1.3**, when a current is applied a conductor with a temperature gradient, the original balance of temperature gradient is changed in the conductor. For maintaining this balance, the conductor needs to absorb or release heat: in addition to the Joule heat caused by the resistance, additional heat absorption or exothermic are happened in the conductor. The heat released or absorbed per unit time is defined as

$$\frac{dQ}{dt} = \beta I \Delta T \quad (1.5)$$

where Q , t , β , I , and ΔT is the absorbed or released heat, time, *Thomson coefficient* with the unit of V/K, current, and temperature difference between the two junctions of the conductor.

The *Thomson effect* has a similar physical mechanism to the *Peltier effect* excepting the different energy source of carriers:

(1) for the *Peltier effect*, energy difference in carriers is caused by the different potential energy of carriers from two different conductors;

(2) for the *Thomson effect*, the difference in carrier energy is caused by temperature gradient leading to the potential energy difference.

1.2.4 Relation between Seebeck, Peltier and Thomson coefficients

The *Seebeck coefficient* ($S(T)$), *Peltier coefficient* (π_{AB}), and *Thomson coefficient* (β) are related to each other. The relation among these three coefficients can be expressed by the *Kelvin relations*,

$$\pi_{AB} = S(T) \times T \quad (1.6)$$

$$\frac{dS(T)}{dT} = \frac{\beta(T_A) - \beta(T_B)}{T} \quad (1.7)$$

The relationship shows that the three thermoelectric effects are interrelated, reflecting the thermal and electrical properties of conducting materials. This formula has been applicable to most metallic and semiconductor materials, which also provides a solid theoretical foundation for modern thermoelectric energy conversion technology.

1.3 The principles of thermoelectric device and evaluation parameters of thermoelectric performance

1.3.1 The principle of thermoelectric device

Based on the *Seebeck* and *Peltier effect*, TE devices consist of TE materials can generate electricity or pumping heat. **Figure 1.4 (a)** is the schematic diagram of a thermoelectric unit based on the Seebeck effect. When a temperature gradient ΔT is applied on the TE unit, the carriers (holes) in the p -type semiconductor and the carriers (electrons) in the n -type semiconductor move from the high-temperature side ($T+\Delta T$) to the low-temperature side (T), and then recombine at the cold end by releasing heat. As the holes/electrons moving, a *Seebeck* voltage is generated between the two ends of the device meanwhile a current is generated in the circuit, enabling conversion between heat and electricity. For the schematic diagram of refrigeration based on *Peltier effect*, applying an electric current on the unit shown in **Figure 1.4 (b)**, electron/hole pairs are generated at one of the ends and flow out, resulting in temperature increasing at one end of the junction and temperature decreasing at the other, enabling refrigeration.

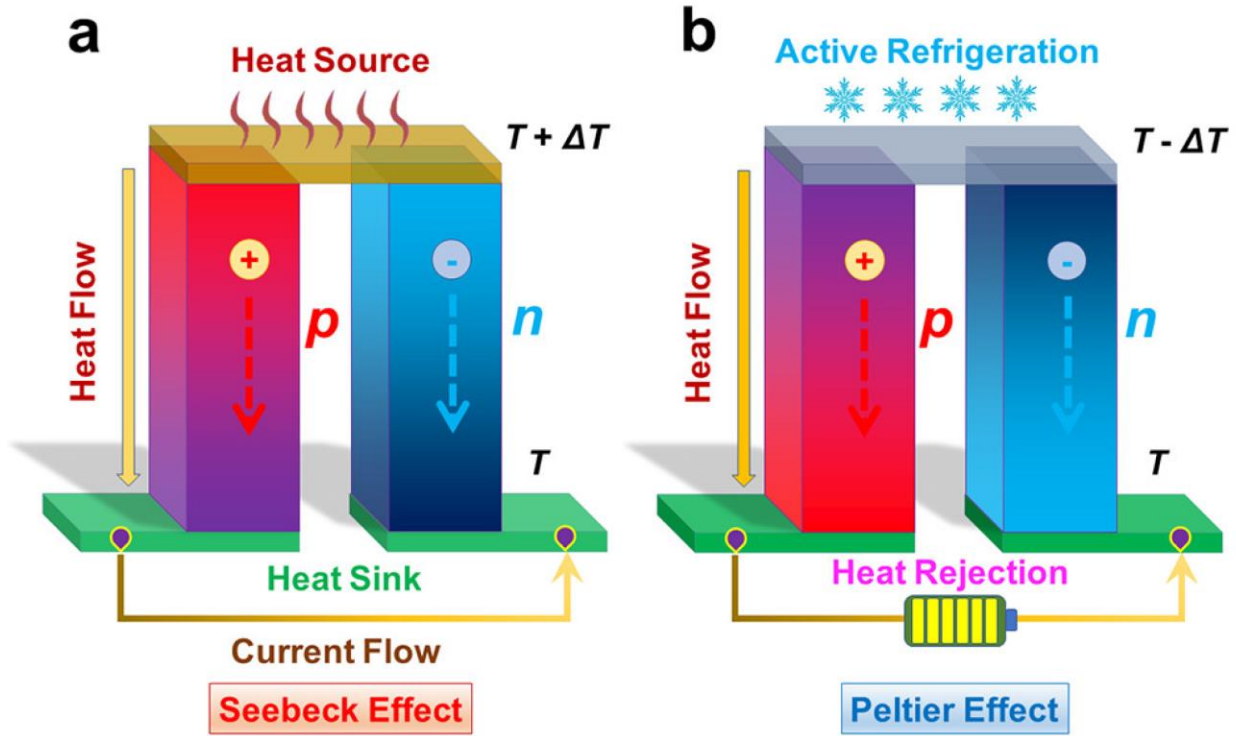


Figure 1.4 Thermoelectric effects. Schematic diagrams of (a) the *Seebeck effect* for power generation, and (b) the *Peltier effect* for refrigeration[25]

In practical, a TE device is generally is constituted by n- and p-type legs in the connection form of thermal parallel and electrical series. In order to improve the energy conversion efficiency of thermoelectric devices, multiple units shown in **Figure 1.4** are connected in thermal parallel and electrical series to form an electrical circuit[2]. It is noticed that in the process of power generation or refrigeration, the TE material itself will generate *Joule heat* when the circuit is formed due to the internal resistance of the material. Therefore, for either of thermoelectric effects, the heat exchange between the material and the environment includes three parts: heat conduction, *Joule heat* and thermoelectric effect heat. The maximum power generation efficiency and the maximum refrigeration efficiency of thermoelectric materials can be obtained by equations 1.8 to 1.10. The maximum power-generation efficiency can be calculated by the equation 1.8,

$$\eta_{max} = \frac{T_h - T_c}{T_h} \left[\frac{\sqrt{1 + ZT} - 1}{\sqrt{1 + ZT} + \frac{T_c}{T_h}} \right] \quad (1.8)$$

And the maximum refrigeration efficiency can be calculated by the equation 1.9,

$$\eta_{max} = \frac{T_c}{T_h - T_c} \left[\frac{\sqrt{1 + ZT} - \frac{T_h}{T_c}}{\sqrt{1 + ZT} + 1} \right] \quad (1.9)$$

where T_h and T_c are the temperature at the hot and cold ends, respectively; \bar{T} is obtained by

$$\bar{T} = \frac{T_h + T_c}{2} \quad (1.10)$$

The equations represents that, at a given T_h and T_c , highly efficient TE power generation and refrigeration determined by the parameter of $Z\bar{T}$, which is defined as dimensionless of figure of merit. ZT is the main parameter to evaluate the TE performance of a TE material.

1.3.2 The evaluation parameters of thermoelectric performance

1.3.2.1 Electrical conductivity

At a given T_h and T_c , the maximum conversion efficiency of the TE materials is only related to the figure of merit (ZT), thus, ZT is the most important index of TE properties of TE materials. ZT is defined as

$$ZT = \frac{\sigma S^2 T}{\kappa} \quad (1.11)$$

σ , S , T and κ is the electrical conductivity, Seebeck coefficient, absolute temperature and thermal conductivity. The definition equation suggests that ZT is mainly related to the electrical and thermal properties of TE materials. The combined parameter of $\sigma^2 S$ is named power factor (PF), which can be used to evaluate the conversion efficiency of TE materials when their κ is similar.

In materials, electrons and/or holes are the main transport carriers. Generally, at a high temperature, the intrinsic excitation of a semiconductor generates equal electrons and holes, while the extrinsic semiconductors under relative low temperatures, the most majority carriers will be electrons or holes depending on the different doping elements. The σ of a material is related to the concentration and mobility of the most majority carriers in the materials

$$\sigma = ne\mu \quad (1.12)$$

where n , e , μ is the carrier concentration, charge constant, and carrier mobility. Therefore, simultaneous optimization of carrier concentration and mobility can improve the σ of a material, thereby improving the ZT .

1.3.2.2 Seebeck coefficient

The equation 1.11 shows that ZT of a material is proportional to its S^2 , thus, it is important to improve the Seebeck coefficient to optimize the ZT of TE materials. For metals and semiconductors, the definition of Seebeck coefficient is

$$S = \frac{8\pi^2 \kappa_B^2}{3eh^2} m^* T \left(\frac{\pi}{3n}\right)^{2/3} \quad (1.13)$$

where κ_B , e , h , m^* , n is Boltzmann constant, charge constant, Planck's constant, effective mass, and carrier concentration. The definition equation suggests that the S is proportional to the effective mass (m^*) but inversely

proportional to the carrier concentration (n) of materials, indicating that the S can be optimized by simultaneously enhancing m^* but reducing the n .

1.3.2.3 Thermal conductivity

The thermal conductivity (κ) of a TE material consists of electronic thermal conductivity (κ_e) and phonon thermal conductivity (κ_l), the equation is expressed as

$$\kappa = \kappa_e + \kappa_l \quad (1.14)$$

The κ in metallic materials is mainly contributed by the κ_e and is estimated by Wiedemann-Franz relation,

$$\kappa_e = L\sigma T = ne\mu LT \quad (1.15)$$

where L is Lorentz number, calculated by the equation:

$$L = 1.5 + \exp[-|s|/116] \quad (1.16)$$

The equation 1.15 suggests that the κ of a material is closely related to its σ , that is, the thermal conductivity increases as the electrical conductivity increasing. In contrast, in the case of semiconductor and insulator, the overall thermal conductivity mainly results from lattice thermal conductivity except the situation that the σ is very high, where, the contribution of κ_e can not be ingored in the materials.

The κ_l is generated by the energy transfer of phonons through the lattice, and thus κ_l is also called phonon thermal conductivity. According to the classical phonon dynamics theory, an approximate formula for the lattice thermal conductivity can be obtained as

$$\kappa_l = \frac{1}{3} C_v v_s l \quad (1.17)$$

where C_v is specific heat of a material at a constant volume, v_s is the average speed of phonon transmission, l is free path of phonon scattering. In general, κ_l and κ_e is independent of each other. In most organic materials and semiconductors, heat conduction is achieved mainly through the transmission of phonons, thus, reducing the lattice thermal conductivity plays an important role in reducing the thermal conductivity of the materials. The lattice thermal conductivity is related to the mean free path of phnonon, however, the mean free path of phonons is influenced by various factors such as crystal structure, composition and defects in the crystal, indicating that increasing phonon scattering by increasing interfaces and defects in materials is an effective way to reduce lattice thermal conductivity[14,15,26].

1.3.3 The interconnection between thermoelectric parameters

The electrical conductivity, thermal conductivity and Seebeck coefficient of the material are coupled with each other and are related to the carrier concentration. The main challenge in optimizing the thermoelectric properties is the inconsistent variation trend of these three properties as carrier concentration varying. These three parameters interact with each other as well as constrain each other. To achieve high TE performance, the n should be in the optimal range, as shown in **Figure 1.5**. As n increasing, σ and κ increase while S decreases. The peak value of ZT is obtained at the carrier concentration range of 10^{19} to 10^{21} carriers per cm^{-3} . The relation between TE performance parameters as a function of n indicates that the TE properties of the material can be optimized by a compromise between its S , σ and κ .

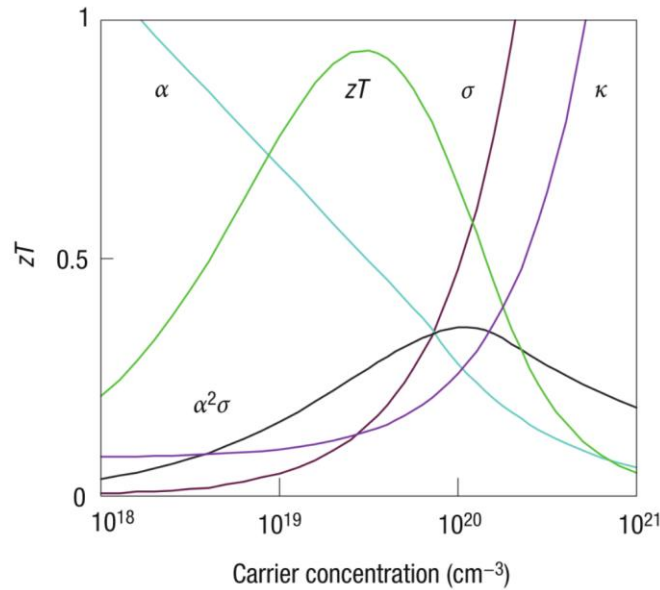


Figure 1.5 Optimizing ZT through carrier concentration tuning. Maximizing the efficiency (ZT) of a thermoelectric involves a compromise of thermal conductivity (κ , plotted on the y axis from 0 to a top value of $10 \text{ W m}^{-1} \text{ K}^{-1}$) and Seebeck coefficient (α , 0 to $500 \mu\text{V K}^{-1}$) with electrical conductivity (σ , 0 to $5000 \Omega^{-1}\text{cm}^{-1}$)[27].

1.4 The progress in thermoelectric materials

1.4.1 Inorganic materials

So far, numerous families of TE materials have been studied and reviewed for a wide range of applications targeting different operating temperature ranges since the first observation of the *Seebeck effect* in 1821[28,29]. For low temperature (less than 500 K) applications, the Bi_2Te_3 families are widely used, as shown in **Figure 1.6**. In a desired temperature range, ZT was enhanced by adjusting the carrier concentration through material composition in p-type $\text{Bi}_{2-x}\text{Sb}_x\text{Te}_3$ and n-type $\text{Bi}_2\text{Te}_{3-y}\text{Se}_y$. It is reported that p-type $(\text{Sb}_{0.8}\text{Bi}_{0.2})_2\text{Te}_3$ compositions and n-type $\text{Bi}_2(\text{Te}_{0.8}\text{Se}_{0.2})_3$ compositions provide the highest ZT , ~ 1.1 for p-type and ~ 0.8 for n-type[27]. Recently, a study has

reported peak ZT of 1.4 at 100 °C for p-type nanocrystalline BiSbTe bulk alloy[11]. In contrast, BiSb alloys have been suggested for applications below room temperature[30]. For mid-temperature range application (500-900 K), TE materials based on group-IV tellurides, such as PbTe[31], GeTe [32,33], and SnTe[34,35] are normally suggested. Silicon-germanium alloys (SiGe) are mostly used for high-temperature (> 900 K) thermoelectric applications. However, the ZT of these TE materials is lower than 1 (**Figure 1.6**) because of the relatively high lattice thermal conductivity of the diamond structure[36].

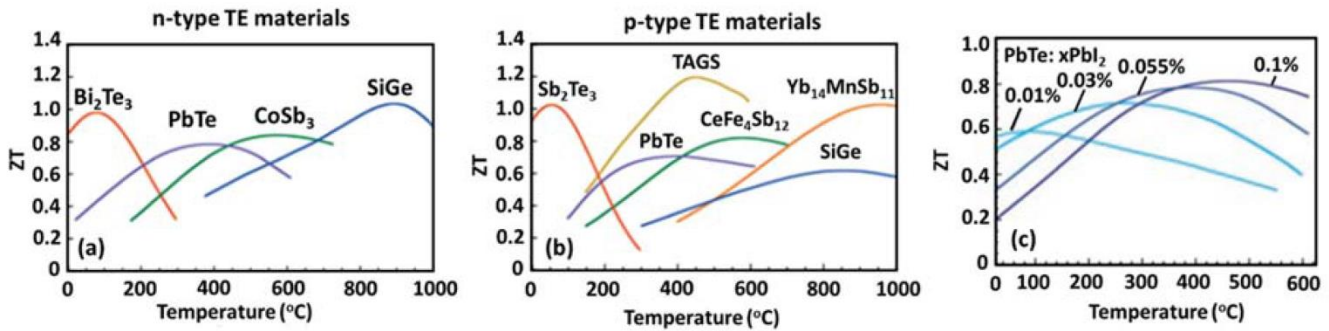


Figure 1.6 Some of the widely used TE materials with their operating temperature and figure-of-merit, ZT. (a) n-type TE materials; (b) p-type TE materials. Most of the TE materials shown here are complex alloys with dopants and compositions approximated; (c) Variation in peak ZT and the optimal temperature with change in dopant concentration for n-type PbTe. Changing the dopant concentration not only alters the peak ZT but also the optimal temperature where the peak occurs[29].

Although some TE materials have been successfully applied to thermoelectric devices[6,10,37], their efficiency is still not competitive with other energy sources, such as solar cells and fuel cells. Thus, improving the ZT of materials is still a major goal in the TE field. On the other hand, the commercial application of TE materials is also an important aspect of research in the TE field. The development of non-toxic, low-cost thermoelectric materials is considered as the key factors to realizing the commercial application of TE materials in the future. Many non-toxic and abundant materials such as CuFeS₂[26,38-40], MgAgSb[10,12,41,42], and Pb-free SnTe[43] have become hot spots in the TE research field.

Recent years, various methods have been utilized to improve the ZT value of inorganic thermoelectrics. The most effective methods include the optimization of carrier concentration and energy band structure to decouple the electrical conductivity and Seebeck coefficient to increase the power factor, and nanostructure engineering to significantly reduce the thermal conductivity of the material while maintaining superior electrical properties to increase the ZT. The following mainly summarizes the current methods for optimizing the ZT value of inorganic thermoelectric materials.

1.4.1.1 Optimizing carrier concentration

Since the electrical conductivity, Seebeck coefficient and thermal conductivity are all related to the carrier concentration, and in turn the carrier concentration has different effects on them, the regulation of the carrier concentration is one of the important methods to improve the ZT value. In practical applications, the carrier concentration of the material can be tuned by external doping and internal defects. For instance, Q.Zhang[44] reported that by controlling the doping concentration of potassium (K), the carrier concentration of $K_xPb_{1-x}Se$ was enhanced to more than $1.5 \times 10^{20} \text{ cm}^{-3}$, thus σ increasing while S decreasing, leading to the ZT value increases with the doping concentration increasing. When $x = 0.0125$, the ZT value of the material reaches the maximum value of 1.2. However, as the carrier concentration keep increasing, the Seebeck coefficient of the material will decrease greatly, which damages the resultant TE performance.

In general, the optimal carrier concentration of TE materials strongly depends on the temperature and the properties of the material itself. Significant theoretical investigation and experimental demonstrations have been dedicated to obtain the optimum carrier concentration for enhancing the TE performance. A. F. Ioffe et al.[45] predicted the optimal concentration of carriers based on the single-band model, and considered that the optimal concentration of n^* was proportional to $(m_d^*T)^{1.5}$, where n^* is the optimal carrier concentration, and m_d is effective mass of density of states. m_d varies with the different band structure. In the doped PbTe system by La and I elements, Y.Z. et al. proved that the relationship of $n^* \propto (m_d^*T)^{1.5}$ is suitable for accurately evaluating the optimal carrier concentration in the doped PbTe system. Usually, T becomes the main factor influencing n^* since m_d^* is small, indicating that, for different aims, the optimal carrier concentration can be obtained by adjusting the temperatures.

1.4.1.2 Nanostructuring

When the power factor of a TE material is increased by doping or alloying, the κ_l will decrease due to phonon scattering caused by the introduction of dopant ions or atoms. However, the introduction of ions or atoms increase the carrier concentration meanwhile increases κ_e . Accordingly, to achieve high ZT, reducing both κ_l and κ through nanoengineering is an efficient way[14,46,47]. Nanoengineering mainly improves the thermoelectric properties by developing low-dimensional nanomaterials and introducing nanocomposites/nanostructures into bulk materials[15,48]. The improvement of ZT value of low-dimensional TE materials is mainly through the quantum effect of nanomaterials[49]. The improvement of ZT value in bulk materials containing nanocomposites/nanostructures is mainly through the complex phonon scattering mechanism and the filtering effect of low-energy carriers[50,51].

(a) Low-dimensional nano-thermoelectric materials

In 1993, L. D. Hicks et al. [49] proposed that low-dimensional/nanocrystalline materials can reduce the κ_l caused by increased phonon scattering to achieve an increase in ZT value through quantum size effect. The reduction of dimensionality changes the density of states (DOS) of nanomaterials and leads to the creation of quantum confinement in the nanostructure, thereby increasing the Seebeck coefficient. According to the assumption, many theoretical calculations and experiments have been carried out and obtain the thermoelectric materials with enhanced

TE performance. For instance, J. J. Urban et al [52] reported that synergism in binary nanocrystal superlattices leads to enhanced p -type conductivity in self-assembled PbTe/Ag₂Te thin films. A. Ishida et al [53] demonstrated the electrical conductivity of SnTe-based films and superlattices. T. C. Harman et al [54] reported that the PbSeTe-based quantum dot superlattices were fabricated by molecular beam epitaxy, and its maximum ZT value was close to 1.6.

On the other hand, quantum nanowires predicted to yield ultra-high ZT values based on lateral dimensions. For instance, Bi₂Te₃ in a quantum-well structure has the potential to increase ZT by a factor of 13 over the bulk value[55]. A. Boukai et al[56] investigated that the dependence of the electrical and thermal transport properties of a single Bi nanowire in the size of nanowire. Moreover, they also fabricated the Si nanowire with a diameter at 20 nm, whose maximum ZT value is around 1 at 200 K that is higher than the value obtained from the Si nanowire with a diameter of 50 nm ($ZT = 0.6$). Besides, M. S. Dresselhaus et al.[57] and Y. M. Lin et al.[58] proposed that the better TE properties could be obtained by heterostructure-nanowire, suggesting that the promising potential of TE materials in the form of low-dimensional nanowire. However, the ultra-high thermoelectric properties of low-dimensional materials have not been well demonstrated yet, mainly due to the following reasons:

- (1) completed synthesis methods and high-cost for Low-dimensional TE materials, such as methods of superlattice nanowire pattern transfer[59], metallic-organic chemistry vapor-deposition[60], and molecular beam epitaxy[54], ect.
- (2) TE materials in nanoscale can not suffer the high ΔT at two different ends.
- (3) it is difficult to accurately measure the TE properties of low-dimensional materials.

However, with the increasing demand for low-dimensional materials for small thermoelectric material devices, it is necessary to develop the low-dimensional materials[61,62], which has become an important research part for TE materials.

- (b) full-scale hierarchical structure

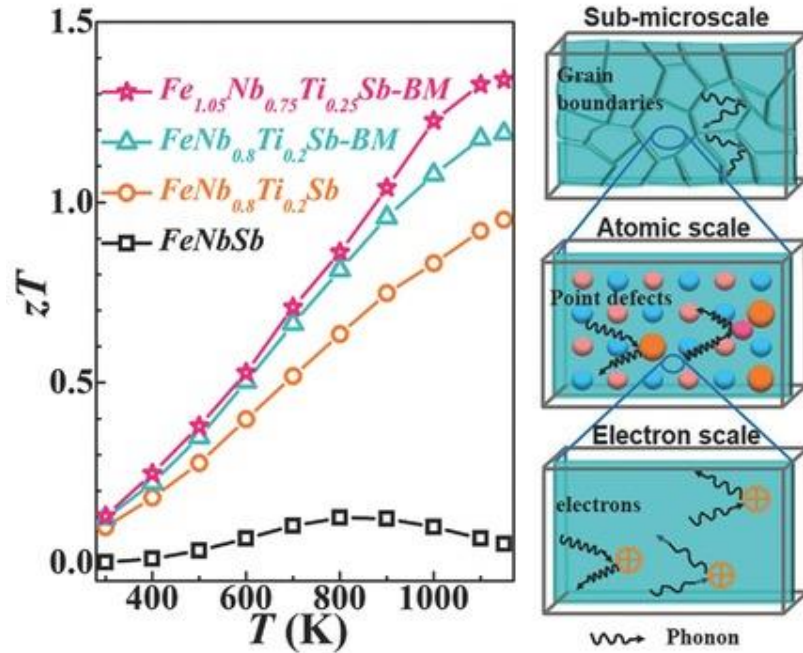


Figure 1.7 Heavy-band FeNbSb half-Heusler system with intrinsically low carrier mean free path is demonstrated as a paradigm. An enhanced zT of 1.34 is obtained at 1150 K for the $Fe_{1.05}Nb_{0.75}Ti_{0.25}Sb$ compound with intentionally designed hierarchical scattering centers[63].

Since the lattice thermal conductivity κ_l mainly depends on the phonon scattering frequency, κ_l can be considered as the sum of phonon scattering at short-wavelength, mid-wavelength and long-wavelength. Through rational design, a full-scale hierarchical structure can be provided for full-spectrum phonon scattering, which can significantly improve the thermoelectric performance of the material, as shown in **Figure 1.7**. The principles of full-scale hierarchical structure that reduces the κ_l including[64-67]:

- (1) Scattering phonons at short-wavelength by point defects.
 - (2) Scattering phonons at mid-wavelength using grain boundaries, dislocations (dislocation arrays), and thin/multilayer structures.
 - (3) Scattering phonons at long-wavelength by nano-micron grains. Since the scale of the phonon scattering is much larger than the mean free path of electron, therefore, the electron transport properties can remain stable, thereby enhancing the TE properties of the material.
- (c) Bulk nanocomposites

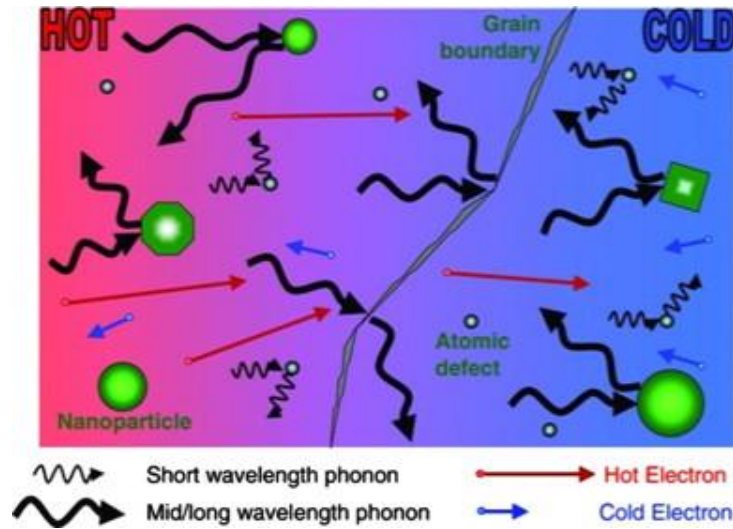


Figure 1.8 Schematic diagram illustrating phonon scattering mechanisms and electronic transport of hot and cold electrons within a thermoelectric material[4]

Compared with the nano TE materials, it is easier to fabricate the nanocomposites and/or TE materials with nanofillers. Besides, there are many options for fabricating bulk TE materials with nanostructure. A high density of interfaces (grain boundaries), lattice distortions, dislocations, and defects are created after introducing nanostructures into the bulk samples which can scatter phonons thus reduce κ_l , thereby reducing overall thermal conductivity. The phonons at mid- and long-wavelength as well as have a similar size with nanograins and grain boundaries can be strongly scattered while the phonons at short-wavelength can be scattered by defects and dislocations, which can achieve 2 times enhancement of ZT[68]. Meanwhile, electrons do not scatter significantly due to their shorter wavelengths, which means that the conductivity of the composite will not drop significantly (see **Figure 1.8**). For example, L. Yang et al [69] reported that with the existence of full-spectrum phonon scattering mechanism benefited from the nanostructuring, the stoichiometric Cu_2Se nanoplates synthesized by a facile and controllable solvothermal method, showed an outstanding ZT of 1.82 at ~ 850 K due to its significantly reduced thermal conductivity.

1.4.1.3 Band structure

The transport behavior of carriers is mainly determined by the energy band structure of materials, thus, tuning the energy band structure can optimize the overall TE performance of the material. The main band-engineering methods include: 1) expand the forbidden band width (E_g) [70]; 2) Adjusting m^* or reaching a resonant state near the Fermi level[71,72]; 3) achieve band convergence[73-75].

(a) Adjusting bandgap

At high temperature, the thermal excitation of minority carriers will increase the total carrier concentration, leading to the Seebeck coefficient decreasing and the electronic thermal conductivity increasing, thus resulting in a decrease

in ZT. Both theoretical and experimental results show that the doping of semiconductors can effectively adjust the width of forbidden band (E_g), and the increased E_g can make the temperature being higher that required for the thermal excitation of minority carriers[76-78], thereby suppressing the carrier concentration increasing in minority [79]. Y. Z. Pei et al.[80] studied the effect of Cd doping on the E_g of PbTe, and the results show that the Cd doping can enlarge E_g of PbTe, so that the doped PbTe can still maintain a stable carrier concentration at high temperature, which can keep relative stable Seebeck coefficient while behaving a low electronic thermal conductivity[80]. As a result, the ZT of 1.7 was achieved at 775 K. It is note that the minority carriers can also act as thermal transport carriers, resulting in bipolarized thermal conductivity (κ_{bi}) thus leading to the increased thermal conductivity as well as reduced ZT. Since κ_{bi} increases with temperature increasing, as temperature increasing, the ZT value of TE materials at intermediate or high temperature will be limited by κ_{bi} increasing [81]. On the other hand, since the thermal excitation of minority carriers decreases with the increase of E_g , the increased E_g will suppress κ_{bi} , thus keeping the resultant thermal conductivity in a stable range.

(b) obtain a resonant state by adjusting the effective mass

Given a carrier concentration, a large effective mass (m^*) will increase the Seebeck coefficient (equation 1.13). The principle of increasing m^* by doping is to increase the effective mass of the energy band (m_b^*) of a single valley due to

$$m^* = N_v^{2/3} m_b^* \quad (1.18)$$

N_v is band degeneracy. However, the relation between m^* and μ ,

$$\mu \propto \frac{1}{m_b^{*5/2}} \quad (1.19)$$

indicates that large m^* does not directly lead to increased ZT value due to a decrease in σ may reduce the power factor of the material[82]. Y. Z. Pei et al.[80,82] reported that the power factor of La-doped PbTe was lower than that of I-doped PbTe under similar carrier concentration, which is mainly due to the fact that La dopants can increase m^* than I dopants. At similar doping levels, the Seebeck coefficient is larger due to the higher m^* of La-doped PbTe, while in I-doped PbTe, it has a higher mobility μ thus leading to a higher power factor, making a higher ZT than that of La-doped PbTe. Thus, it is important to adjust the m^* and μ to improve σ and S , obtaining an optimum ZT.

(c) Band convergence

The large band degeneracy N_v can also increase m^* without affecting the mobility, thereby increasing the ZT[73]. Through optimal doping, temperature increasing and the changing of crystal symmetry, the multiple electron energy band of the material can be converged and N_v increasing[73,83]. M. Hong et al[75] showed that the power factor and ZT values of rock-salt-structured chalcogenides increased significantly when band convergence occurred: when ΔE decreases, the power factor of SnTe increases; at 900 K, ΔE is 0 eV (two valence bands converge), and the power

factor reaches the maximum value. The maximum ZT values for band-converged PbTe, PbSe and SnTe have been predicted to be 2.2, 1.8 and 1.6. If κ_l can be kept small, by optimizing the carrier concentration, the ZT value of the material can be increased even further. In addition, band convergence can also be achieved in other materials, such as $Mg_2Si_{1-x}Sn_x$ solid solutions[84], $Bi_{2-x}Sb_xSe_3$ [85], and the tetragonal chalcopyrite structure[86,87], etc.

1.4.1.4 Energy filtering effect

When a band shift occurs between the main matrix and nanofillers, their boundaries filter low-energy or secondary carriers due to the energy filtering effect. The main reason of the energy filtering effect can increase the Seebeck coefficient is that the seebeck coefficient strongly depends on the transport behavior of carriers.

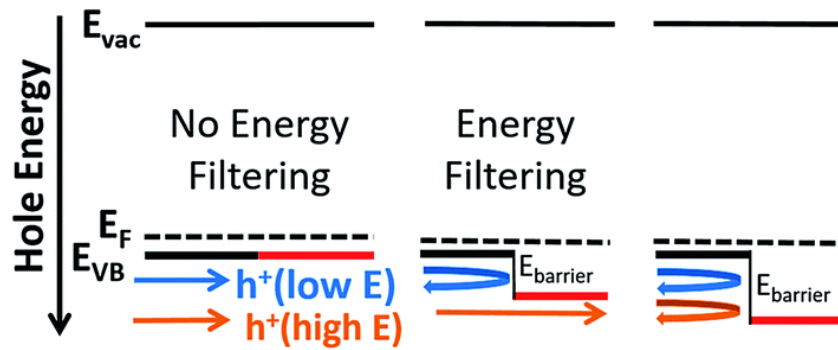


Figure 1.9 Schematic of how an appropriate energy barrier (center) can lead to energy filtering. E_{vac} is the vacuum level, E_F is the Fermi energy, and E_{VB} is the valence band energy. The black and red lines for E_{VB} represent the matrix and nanoparticles[88].

Figure 1.9 schematically illustrates that the carriers with high energy pass the energy barrier while the carriers with low energy is filtered. According to the calculation results[89], it is proposed that the Seebeck coefficient of low-energy carriers is negative, which will reduce the resultant Seebeck coefficient, in contrast, the carriers with energy in the range of 0.05-0.1 eV make the greatest contribution to a high Seebeck coefficient. By introducing potential barriers at the grain boundaries, low-energy carriers can be filtered out[90], thereby increasing the average energy of carriers, causing the Seebeck coefficient increases without a significant decrease in conductivity. J. Kim et al.[91] proved this conclusion experimentally. They prepared Ag-doped Sb_2Te_3 by electrodeposition, the power factor of $1870 \mu W/m K^2$ of $Ag_{3.9}Sb_{33.6}Te_{62.5}$ was achieved at 300 K.

1.4.1.5 Defect control

The effects of defects on the TE properties in materials are mainly reflected from the following aspects: 1) influencing carrier concentration of the intrinsic or extrinsic of thermoelectric materials; 2) influencing the carrier mobility through carrier scattering; 3) reducing lattice thermal conductivity through phonon scattering; 4) improving

the mechanical properties of materials. Therefore, adjusting the defects in materials is one of the important methods to improve the performance of thermoelectric materials.

The effects of defects on the electronic transport properties are ascribed to their effects on electronic states and band structures[92,93]. C. Xiao et al.[94] found that magnetic dopants such as Ni can introduce more electron spins into $\text{Cu}_2\text{ZnSnS}_4$ and enhance the electron-electron interaction to generate spin entropy[95], thereby increasing the Seebeck coefficient. In addition, the magnetic dopant induces a decreased E_g and an enhanced anomalous resonance of the energy band, resulting in a substantial increase in the ZT value of $\text{Cu}_2\text{ZnSnS}_4$. K. Park et al.[96] prepared K^+ -doped non-stoichiometric $\text{Bi}_2\text{Te}_{3,14}$ by solution method, in which K^+ did not replace Bi^{3+} but existed in the gap and interlayer sites of $\text{Bi}_2\text{Te}_{3,14}$, and acted as electron donor raising the Fermi level of $\text{Bi}_2\text{Te}_{3,14}$ to the conduction band, so that the doped $\text{Bi}_2\text{Te}_{3,14}$ exhibits *n*-type conductivity. In addition, the dopant K^+ can provide phonon scattering, which increases the ZT value of $\text{Bi}_2\text{Te}_{3,14}$ to 1.14 at 350 K. Another important role of crystal defects is to provide phonon scattering. Z. W. Chen et al. [97] used cation holes to induce a large number of dislocations in $\text{Pb}_{1-x}\text{Sb}_{2x/3}\text{Se}$, which reduced the thermal conductivity of the material to 0.4 W/m K. S. I. Kim et al.[98] introduced a high density of dislocations into the grain boundaries of $\text{Bi}_{0.5}\text{Sb}_{1.5}\text{Te}_3$ to scatter low- and high-frequency phonons, so that decreasing the thermal conductivity of the material, and the ZT was increased to 1.86 at 320 K. The optimization of material porosity also contributes to improve the TE properties [99,100].

1.4.2 Organic thermoelectric materials

Despite the high ZT value of inorganic thermoelectric materials, new materials that can replace inorganic thermoelectric materials are required due to the complex preparation process, high raw material cost, inflexibility, and disadvantages such as toxicity. The emergence of conductive polymers provides a new idea for the development of thermoelectric materials. Since the polymer with remarkably high conductivity was firstly discovered in 1977[101], conducting polymers and their derivatives have been arising increasing attention in the fields of organic photovoltaics[102,103] and sensors[104,105] because of their tunable σ , good flexibility, low cost, and low toxicity. Owing to their intrinsic low κ of $\sim 0.1\text{--}0.5 \text{ W m}^{-1} \text{ K}^{-1}$ [106-109], tunable σ , and good flexibility, conducting polymers have been regarded as the promising next-generation flexible TEs. However, insufficient σ and S of conducting polymers is similar to that of conventional intrinsic thermoelectric materials. Doping has been widely used to activate extra electrons (*n*-type doping) or holes (*p*-type doping) to tune the carrier concentrations of the host.

1.4.2.1 Carrier transport mechanism in conductive polymers

Saturated insulating polymers consist of covalently bonded atoms and sp^3 -hybridized carbons, where shared electrons are located in the lower-energy orbitals of the chain molecules, resulting in their poor electrical conductivity. In conjugated polymers, carbon atoms are sp^2 hybridized. The three electrons in the outer shell of each carbon atom form three σ bonds to form the polymer backbone and provide a 2p electron. This electron is delocalized in the π orbital which dominates the electron density of the vertical σ bond skeleton. Delocalized electrons move easily along

the polymer backbone due to overlapping carbon atoms[9]. In carbon atoms with alternating σ and π bonds, due to Peierls instability (a result of the coupling of electronic and elastic properties), the π band is divided into a π band (full band) and a π^* band (empty band), both of which have a band gap E_g in the electronic excitation spectrum. Compared to conventional semiconductors, the bonding orbital (π) corresponds to the valence band of the semiconductor, and the antibonding orbital (π^*) corresponds to the conduction band of the semiconductor. In the conjugated part of the polymer molecule, between the highest occupied orbital (HOMO) and the lowest unoccupied orbital (LUMO), this band-like energy, the distribution lies between the densities of electronic states with an energy gap, similar to the energy distribution of intrinsic semiconductors[9]. This conjugated structure results in poor conductivity of conductive polymers, which cannot meet the needs of practical applications.

(a) The electrical conductivity of conductive polymers

Typically, conducting polymers can be chemically/electrochemically doped. In polymers, doping is a redox reaction that converts an initially non-conductive polymer into an ionic complex consisting of a counter-ion formed by the cation/anion of the polymer and the reduced/oxidized form of the oxidant/reductant [110]. This reaction is well suited for π -bonded unsaturated polymers with π -electrons that readily delocalize without disrupting the σ -bonds that maintain the integrity of the polymer chain. The mechanism by which carriers are generated to enhance conductivity after doping of conductive polymers mainly includes:

1) The redox reaction of monomers by losing/gaining electrons starts from the π system of the main chain, resulting in free radicals or generation of spin-free positive/negative charge. The oxidizing/reducing agents converts into counter ions neutralizing the positive/negative charges introduced in the π -electron system;

2) The local resonance of charges (lattice distortion) and radicals leads to the coupling of charge sites to groups, forming polarons;

3) Polarons formed by radical cations or anions enable new electronic localized states in the band gap, where lower energy states are occupied by a single unpaired electron;

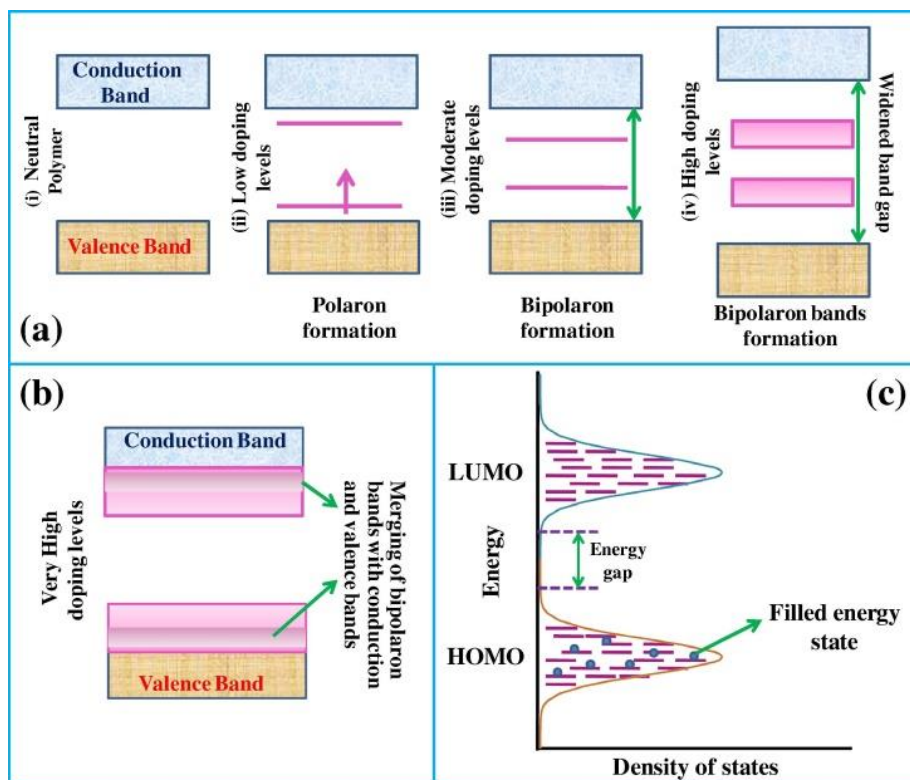


Figure 1.10 Schematic showing (a) formation of polaron, bipolaron and bipolaron bands as a function of doping for CPs; (b) Merging of bipolaron bands with conduction and valence bands at very high doping levels; (c) Gaussian distribution of localized states in HOMO and LUMO orbitals of CPs[111].

4) removing/adding an electron to a polaron can create new spin-free defects called bipolarons. It is a radical ion pair associated with polaron twist. Depending on the chemical structure of the polymer, bipolarons can affect three to four monomers. Bipolarons are thermodynamically easier to generate than two polarons, thus at higher doping levels, two polarons are more likely to combine to form bipolarons. **Figure 1.10** shows the relation between generation of polarons, bipolarons, and bipolaron bands in different polymers and doping level. At low doping levels, polarons with $1/2$ spin are formed. As the doping level increases, the polarons recombine to form non-spin bipolarons. Further increasing the polarization degree, the energy levels of the bipolarons overlap, form polarized subbands.

The conduction mechanism of conjugated conducting polymers with degenerate ground states such as polyacetylene can be explained by a different mechanism[112]. In addition to polarons, solitary wave defects called solitons exist as charge carriers. Solitons are able to move freely along molecular chains by pairing with neighboring electrons. In the conduction mechanism, the solitons generated by doping are more important than those generated by defects caused by bond alternating. After doping, the two charges forming the bipolaron are weakly bound and easily separated due to the degradation of the conducting polymer. Since the energy between the charges is the same as on both sides, they propagate like a soliton wave without any distortion and energy loss. In pure polyacetylene, when the

number of conjugated carbon atoms is odd, lone electrons are called neutral lone electrons[113]. When another unpaired electron is added to it, the charged soliton is called a negative electron, while removing the electron gives to the positive solitary. The generation of solitons forms new localized states in the energy gap. As the doping level increases, charged solitons interact to form soliton bands that can eventually merge with the valence/conduction band edges, resulting in metallic conductivity[114].

This conduction mechanism of conducting polymers is influenced by the space and energy of the molecular chains in the polymer. The extra charge carriers generated by doping in the polymer are trapped into the chains due to the electrostatic attraction of the counter ions[115]. In low-doped organic materials, the trap problem is very significant and large in size. These traps reduce the mobility of carriers. As the doping level increases, the traps overlap and the energy barrier between them tends to decrease, and the decrease in the energy disorder in the π orbital can increase the mobility[112]. Spatial disorder such as counterion position, chain spacing, chain configuration, size of crystalline and amorphous regions, and crystallite orientation can all affect carrier transport.

In conducting polymers, charge transport by jumping[116,117]. In undoped/lightly doped polymers, the polaron transitions to the adjacent neutral part of the chain due to the applied electric field. In doped disordered polymers, charge carriers (polaron and counterion pairs) transition from one polarization site to another without causing deformation of the polymer chains. When the density of states is assumed to be constant, in disordered or amorphous conducting polymers, the variation of conductivity with temperature is mainly described by the variable-range transition (VRH) conduction model,

$$\sigma(T) = \sigma_0 \text{EXP}\left[-\left(\frac{T_0}{T}\right)^{1/(1+d)}\right] \quad (1.20)$$

where d is the jumping dimension, and T_0 is Mott temperature. Conductivity of moderately doped and structurally ordered polymers enables transition from insulating to metallic states[118]. The electrical conductivity of highly doped and highly ordered conducting polymers such as camphorsulfonic acid-doped polyaniline (PANI) exhibits metal-temperature dependence with decreasing temperature[119].

(b) Seebeck coefficient

The Seebeck coefficient of the material is mainly generated by three contributions: electron, phonon, and electron-phonon[120]. Highly conductive polymers with good crystal structures may exhibit significant phonon-electron scattering at low temperatures[116]. Heavily doped polymers such as polyacetylene (PA), PANI, and polypyrrole (PPy) have small Seebeck coefficients (below 14 $\mu\text{V/K}$ around room temperature) decreasing with increasing temperature[121]. For lightly doped conducting polymers, the Seebeck coefficient may be several orders of magnitude higher than for heavily doped polymers[117] and increases or decreases nonlinearly with temperature. In some cases, the nonlinear reduction of the Seebeck coefficient may follow the $T^{1/2}$ relationship and can be explained by the Mott transition theory of carriers between localized states. Nearest-neighbor transitions of carriers in localized states cause

the Seebeck coefficient to exhibit a $1/T$ dependence with temperature, while in heavily doped states, the variation of the Seebeck coefficient is linearly related to the temperature variation[121].

(c) Thermal conductivity

Unlike in inorganic materials where electronic thermal conductivity correlates with electrical conductivity, in conducting polymers, this synergy is ineffective (violating the Wiedemann-Franz law) mainly due to the presence of stronger ions in conducting polymers. Since the thermal conductivity of polymers is much lower than that of inorganic materials, the contribution of electronic thermal conductivity to thermal conductivity is very small[108,122]. Therefore, in conducting polymers, most of the heat is conducted through phonon vibrations rather than charge carriers, i.e., $\kappa_l > \kappa_e$. Furthermore, the thermal conductivity of polymers is not only dependent on the molecular weight and shape of the polymer, but also related to the chain structure of the polymer. There are four main structures of polymers: linear, branched, cross-linked and network. The difference in polymer structure determines its thermal conductivity and diffusion anisotropy[123]. For certain conducting polymers, this anisotropy is more pronounced when the molecular chains are more ordered. Furthermore, for amorphous polymers with ordered polymer chains, this anisotropy still exists, and the main reason results from the changes in the heat transport mechanism in different directions[124]. The strength along the polymer chain C-C covalent bonds are more efficient for thermal energy transfer than van der Waals forces along the vertical direction[123]. In thin film materials, more molecules are arranged in the in-plane direction of the film than in the vertical direction, which is the main reason for the higher in-plane thermal conductivity of thin-film materials. It is worth noting that although the thermal conductivity of conducting polymers is anisotropic and affected by many factors, even if the conductivity of the polymer is increased by 3 orders of magnitude, its thermal conductivity only increases from 0.1 to 1.0 W/m K, and the thermal conductivity of conductive polymers is still lower compared to inorganic materials.

1.4.2.2 Thermoelectric properties of conductive polymers

At present, the more mature research in conductive polymers mainly include PA, PANI, PPy, polythiophene(PTh), poly 3,4 ethylenedioxythiophene (PEDOT) and its derivatives, poly3,4 ethylene-dioxythiophene-polystyrene sulfonate (PEDOT:PSS), polycarbazole, etc. Compared with inorganic materials, the thermal conductivity of conductive polymers is lower and more stable, so the improvement of the ZT value of conductive polymers is mainly achieved through the optimization between the conductivity and the Seebeck coefficient. In addition, conductive polymers are typically used at temperatures below 150 °C due to their poor stability at high temperatures. At present, many researches are devoted to the preparation of organic-inorganic composite thermoelectric materials to combine the advantages of organic and inorganic materials through synergistic effects[125,126]. In addition, structural regulation of polymers and addition of fillers are also important methods to improve their thermoelectric properties[118,127,128]. The main methods for improving the thermoelectric properties of conductive polymers are reviewed below.

(a) Doping

Redox-Based Doping: to achieve appreciable σ , polymers or organic semiconductors can be oxidized into p-type or reduced into n-type by introducing charge carriers via chemical[129] or electrochemical reactions[130], which is carried out using p-type or n-type dopant to carry through electron transferring. The energy levels of the dopant and polymer determine electron transfer. **Figure 1.11(a)** illustrates the charge transfer mechanism of doping polymers, where electron transfer from highest occupied molecular orbital (HOMO) of polymer to the lowest unoccupied molecular orbital (LUMO) of dopant in the process of p-doping, while electron transfer from HOMO of dopant to the LUMO of the polymer causes n-doping. As a result, p-doping requires the polymer's HOMO to be higher than the dopant's LUMO, and it presents n-doping when the HOMO of dopant is higher than the LUMO of the polymer. To make the energy levels matching, chemical redox dopants, i.e., I_2 [131], $FeCl_3$ [132] and 2,3,5,6-tetrafluoro-7,7,8,8-tetracyanoquinodimethane (F4TCNQ)[133], are treated as efficient dopants for P3HT possessing high HOMO level[134]. Besides tunable carrier concentration by doping, the doping process significantly impacts the microstructure and resultant charge transport of polymer. The p-doping can be realized in solution-processed doping, vapor-phase doping[135], or electrochemical doping[130]. For example, F4TCNQ doped P3HT behaves poor σ because of the aggregates in solution doping. The morphology of P3HT was maintained during vapor-doping[135]. **Figure 1.11(b)** illustrated the vapor-doped process of P3HT film by F4TCNQ. It was found that F4TCNQ entered the side chains of P3HT for maintaining its crystalline order, which contributes to the high σ compared to the films obtained by solution-processed. Electrochemical doping is an alternative approach to precisely control the doping level in the polymer[136]. Recently, the *ex situ* electrochemical bulk doping approach was developed to fine-tuning σ of P3HT film[130]. P3HT film was first electrochemically doped and then dried outside for 4-line probe conductivity measurements. With the increase of electrochemical potential, the maximum σ of 224 S cm^{-1} was achieved in P3HT film. The highly conducting states can be maintained at potentials between 0.4 to 0.8 V (vs Fc/Fc^+).

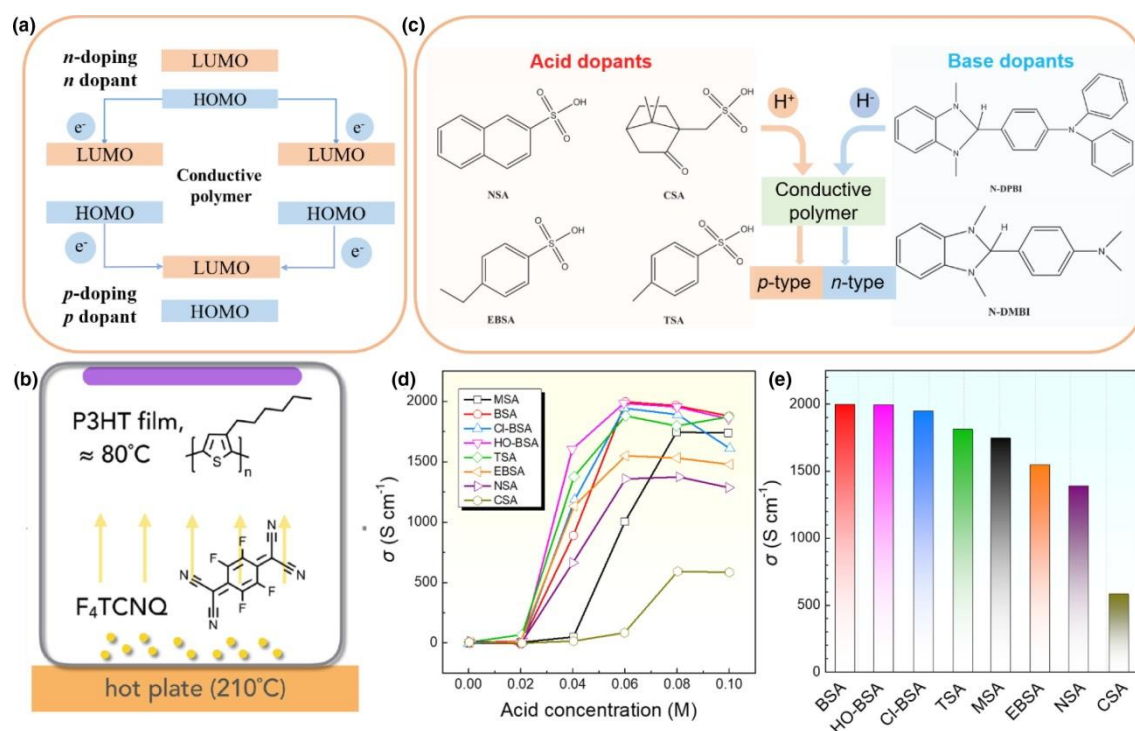


Figure 1.11 (a) Schematic illustration of the charge transfer mechanism in p- or n-doping polymers. (b) Schematic of F4TCNQ vapor doped P3HT film and chemical structures of P3HT and F4TCNQ. (c) Representative acid/base dopants and typical acid-base reactions. (d) Acid concentrations dependent σ for various sulfonic acids doped PEDOT:PSS films. (e) Average σ of various sulfonic acids doped PEDOT:PSS films at the optimum doping concentration[137].

Acid-Base doping: For conductive polymers, acid-base doping can improve σ of conducting polymers by inducing protonation or deprotonation reactions. Acid-base reactions involve transferring a proton (H^+) or hydride (H^-) between the conjugated polymer and the dopant. The driving force is mainly determined by the frontier orbital energy. A higher HOMO level facilitates proton (H^+) to transfer to the conjugated polymer accompanying with p-type doping, while a lower LUMO level of the conjugated polymer benefits the n-type doping by hydride (H^-) transferring[116]. **Figure 1.11(c)** shows several representative molecular structures of acid and base dopants and illustrates charge transfer during the acid-base reaction process. For PEDOT:PSS polymers, the interaction within the polymer backbone was weakened by the acid, which affects the packing of PEDOT chains[138]. Generally, one acid with a more negative acid association constant (pK_a) can provide more H^+ protons to bind with PSS, and in turn promote the weakened or disappeared Coulombic combination and even phase separation between PEDOT and PSS, leading to improved σ [139]. However, the σ values were found to be strongly affected by the functional groups of acids other than pK_a [139]. Taking sulfonic acid as an example, including methanesulfonic acid (MSA), p-toluenesulfonic acid (TSA), b-naphthalene sulfonic acid (NSA), camphorsulfonic acid (CSA), benzenesulfonic acid (BSA), 4-chlorobenzenesulfonic acid (Cl-BSA), p-hydroxybenzenesulfonic acid (HO-BSA), and 4-ethylbenzenesulfonic acid (EBSA), are used to dope into PEDOT:PSS polymers and the corresponding σ variations have been investigated in detail [139]. Compared to 0.6 S cm^{-1} of pristine PEDOT:PSS film, σ of PEDOT:PSS film doped by the acid increases significantly and also progressively increases with increasing acid doping concentration until saturated, as shown in **Figure 1.11(d)**. **Figure 1.11(e)** shows that a highest σ of 1996 S cm^{-1} was obtained from the BSA doped PEDOT:PSS film[139]. The increased μ and oxidation level was contributed through the acid doping, leading to dramatically enhanced σ in the acid doped PEDOT:PSS film. However, as expected in this scenario, among the various acid doped PEDOT:PSS films, σ values are found to be not changed with the pK_a values of various sulfonic acids. Specifically, the MSA with the most negative pK_a (-2.6) exhibits a moderate σ of $1755.1 \pm 134.1 \text{ S cm}^{-1}$ while the HOBSA with the highest pK_a (9.1) has a higher σ value of $1988.3 \pm 61.4 \text{ S cm}^{-1}$ [139]. After deeply comparing and analyzing the spatial structures of the acids and the structures of doped films, the different enhancements of σ should be attributed to the stereo and conjugated structures of the different sulfonic acid dopants[139]. This indicates that the steric effects induced by the functional groups from various sulfonic acids have great influences on σ . Furthermore, the pH-dependent thermoelectric properties of free-standing PEDOT:PSS films were systematically studied under acids and alkalis conditions[140]. The experiment results indicate that the acidic conditions with lower pH values can enhance the thermoelectric performance of PEDOT:PSS films, while the increased pH value in alkaline solutions rapidly

degrades the thermoelectric performance of PEDOT:PSS films[140]. Compared to p-type acid-base doping, n-type acid-base doping is less developed due to low σ [141] and the lack of air-stable dopants[142].

(b) Conducting polymer/nanocarbon composites

Owing to outstanding properties such as high σ , high chemical and thermal stability, high flexibility, good mechanical properties, light weight, easy modification or functionalization as well as scalable synthesis, carbon materials such as graphene and carbon nanotubes (CNTs) show great potentials in the flexible TEGs. For instance, μ of intrinsic exfoliated graphene can be up to $\sim 150,000\text{-}200,000 \text{ cm}^2 \text{ V}^{-1} \text{ s}^{-1}$ [143]. The p- and n-type CVD-grown graphene show ultrahigh $S^2\sigma$ of 6930 and 3290 $\text{mW m}^{-1} \text{ K}^{-2}$ [144], respectively, which are the best values among the reported flexible TE materials. The theoretical calculated $S^2\sigma$ of single-walled carbon nanotube (SWCNT) can reach up to 700 $\mu\text{W m}^{-1} \text{ K}^{-2}$ [145]. Therefore, introducing carbon materials into conductive polymers as inorganic fillers is an effective approach to improve their thermoelectric performance by synergistically combining advantages of the individual component.

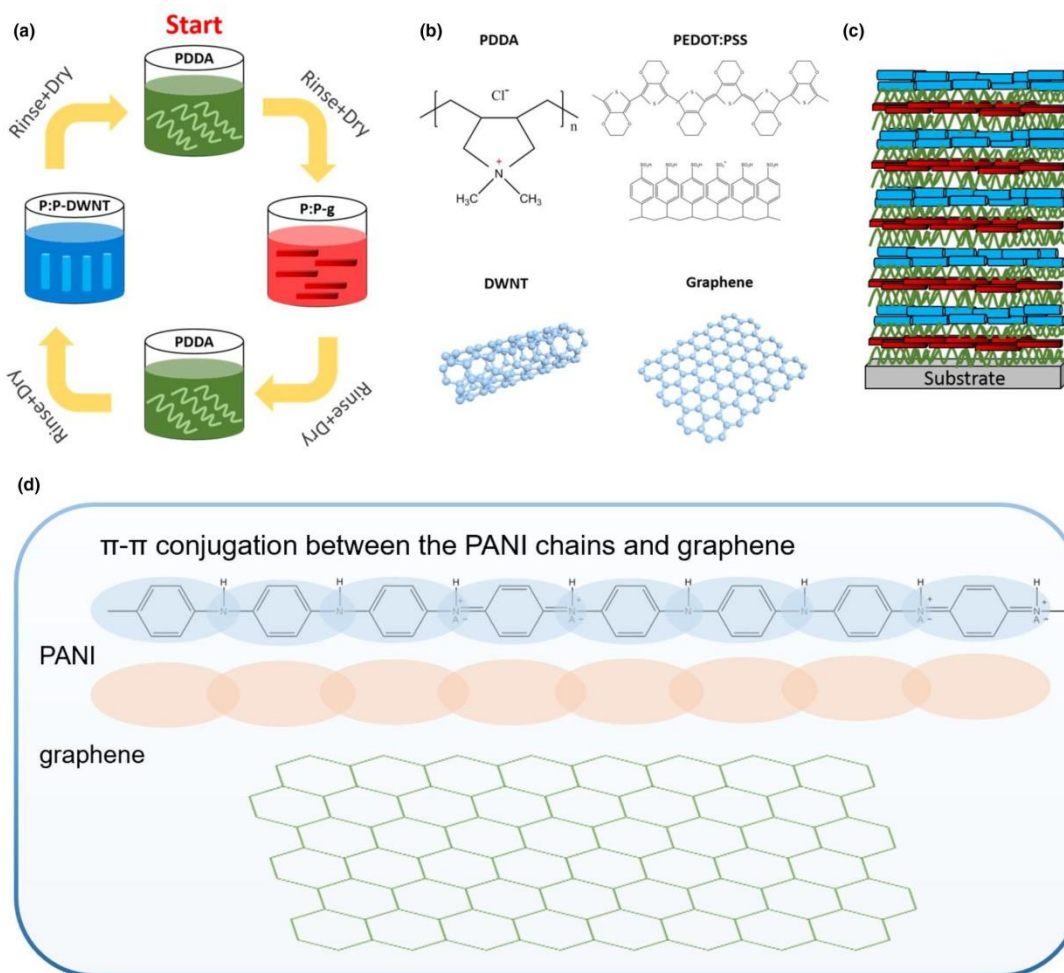


Figure 1.12 (a) A typical LBL fabrication process for PDDA/PEDOT:PSS-graphene/PDDA/PEDOT:PSS-DWNT thin film. (b) Molecule structures of PDDA, PEDOT:PSS, DWNT, and graphene. (c) The LBL-assembled multilayer films. (d) $\pi - \pi$ conjugation between the PANI chains and graphene.[146]

Exfoliated graphene nanoplatelets can be incorporated into PANI by the mechanical mixing method[147]. However, it is difficult to obtain homogenous dispersion of graphene fillers in conducting polymer matrix through the physical mixing, where the ZT values of composites are greatly limited. To uniformly disperse carbon materials, various methods, such as drop-casting[148], in situ polymerization[149], and layer-by-layer (LBL) deposition[150], has been developed to fabricate well-dispersed carbon based fillers. For instance, Zhou et al used ultrasonication to dissolve poly(benzo[1,2-b:4,5-b']dithiophene-alt-3,4-ethylenedioxythiophene) (PBDT-EDOT) and SWCNT in a solution[148]. Uniform composite films fabricated by the mixture of PBDT-EDOT and SWCNT solutions were obtained by drop-cast method. The composite PBDT-EDOT/SWCNT film with > 90% SWCNT content shows a high $S^2\sigma$ of $74.6 \mu\text{W m}^{-1} \text{K}^{-2}$ at 400 K. In addition, a facile and effective in situ polymerization method was reported to improve TE properties of PEDOT:PSS/graphene composite. The PSS is not only used as a dispersant for graphene but also as a dopant for PEDOT[149]. A homogeneous dispersed PEDOT:PSS/graphene composite without obvious aggregation was obtained and employed in a thermoelectric device with a $S^2\sigma$ of $45.7 \mu\text{W m}^{-1}\text{K}^{-2}$. The LBL assembly can achieve highly tunable ordered structures and controlled thickness of composites. **Figure 1.12(a-c)** illustrate a typical LBL fabrication process for preparing PDDA/PEDOT:PSS-graphene/PDDA/PEDOT:PSS-DWNT thin film[150]. Graphene and DWNT were firstly mixed with PEDOT:PSS under repeat sonication to form PEDOT:PSS-graphene and PEDOT:PSS/DWNT solutions, respectively. In the first cycle deposition, the pre-cleaned substrate was initially immersed into 0.25 wt% PDDA solution following with rinse and dry, then the film dipped to PDDA, PEDOT:PSS-graphene, PDDA, and PEDOT:PSS/DWNT solution in sequence. For the subsequent cycles, each step followed with the same rinsing and drying procedure. The LBL-assembled multilayer films maintain a highly internal ordered network structure, where graphene and double walled carbon nanotube (DWCNTs) are self-assembled by their $\pi - \pi$ interactions with PEDOT:PSS and PDDA. The PANI/graphene/PANI/DWNT nanocomposite with ordered molecular structure shows a remarkable $S^2\sigma$ of $1825 \mu\text{W m}^{-1} \text{K}^{-2}$ [151]. Apart from the above methods, an unconventional route was adopted to prepare uniform and intimately interfaced P3HT-grafted DWCNT composite film via covalent grafting with an amidation reaction[152]. Experiment results show that a well-defined P3HT/DWCNT interface can effectively strict the aggregation of DWCNTs, leading to an enhanced S of $116.6 \mu\text{V K}^{-1}$ and a high power output of 14.5 nW. A newly dilution-filtration method was used to prepared *p*-type composite by integrating SWCNTs into the PEDOT:PSS matrix[152], which avoids the drawbacks of time-consuming and complicated process of drop-casting or spin-coating. A $S^2\sigma$ value of $83.9 \mu\text{W m}^{-1}\text{K}^{-2}$ can be observed in the PEDOT:PSS/SWCNTs composites[152].

Graphene or CNT provides a 2D platform or 1D template to extend the conformation of conducting polymer from coil-like to linear-like along the surface of graphene or CNT through $\pi - \pi$ interaction between conducting polymer and graphene or CNT[153]. **Figure 1.12(d)** shows the $\pi - \pi$ conjugation between PANI and graphene, where PANI

molecules adsorb on graphene nanosheets surface and tend to extend its intrinsic twist structure[154]. Meanwhile, owing to the $\pi - \pi$ interactions with PANI, the graphene nanosheets facilitate the carrier transport to increase μ and σ , leading to the highest ZT value of 1.95×10^{-3} , which is 70 time higher than that of PANI. A free-standing PANI/3D graphene composite was proposed by growing PANI on 3D graphene, where the exchanged role between PANI and 3D graphene is unlike usual: 3D graphene as a host matrix and PANI as fillers[155]. Such a behavior prevents the aggregation of graphene and facilitates the PANI homogeneously disperse into 3D graphene. A $S^2\sigma$ of $81.9 \mu\text{W m}^{-1}\text{K}^{-2}$ can be observed in the PANI/3D graphene composite with 80 wt% PANI loading. Such high $S^2\sigma$ is attributed to the synergistic effect of strong $\pi - \pi$ interactions between PANI and graphene and energy filtering effect at interfaces of PANI and graphene. Similar to organics/2D layer materials, the organic/inorganic nanocarbon materials also show great potential for realizing both high thermoelectric and mechanical properties by proper rational material and synthesis design.

(c) Conducting polymer/inorganic composites

Although some remarkable progresses have been made to enhance thermoelectric properties of conducting polymers, the improvements of ZT values, especially for n-type conducting polymers, are still limited. To achieve higher ZT values, the hybrids of conducting polymers and inorganic materials have been developed in recent years, which take advantage of intrinsic low κ and flexibility from polymers and superior S from inorganic materials. In conducting polymer/inorganic thermoelectric composites, inorganic materials are acting as fillers, and conducting polymers are host matrices. Specifically, inorganic materials disperse/embed uniformly in the matrix of conducting polymers to create abundant organic–inorganic interfaces. An energy barrier is produced at these interfaces due to an energy offset between the bands of the inorganic filler and conducting polymer. Carriers can pass the barrier when the carrying energy is higher than the energy barrier. Otherwise, carriers with lower energy can be blocked. Calculation results indicated that carriers with higher energy contribute to S particularly for carriers with the energy of 0.05–0.1 eV while low-energy carriers lower S [89]. Such an energy filter effect promotes S and slightly reduces σ due to the reduction of n , which still benefits to the enhancement of $S^2\sigma$.

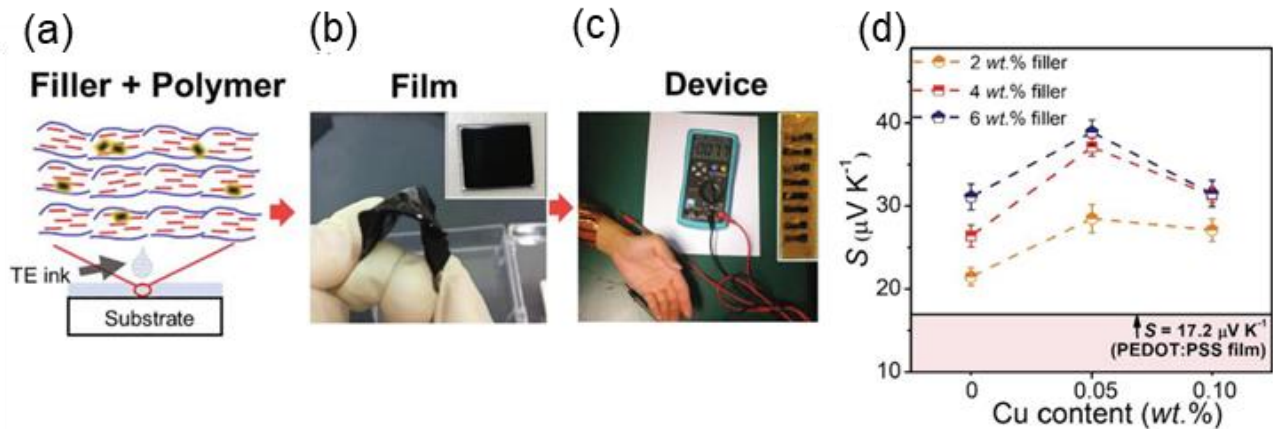


Figure 1.13 (a) Illustrated PEDOT:PSS/Cu-BST composite. The fabricated PEDOT:PSS/Cu-BST FTE materials (b) and (c) FTEG. (d) S of PEDOT:PSS/Cu-BST composite with Cu content between 0~0.1 wt% (BST filler content 2 wt%, 4 wt% and 6 wt%). [146]

On the other hand, surface engineering of inorganic fillers, such as surface treatment, can further optimize interfacial carrier transports to decouple the interrelated thermoelectric parameters of conducting polymers/inorganic composites. For instance, highly conductive CuTe layer was coated on surface of $\text{Bi}_{0.5}\text{Sb}_{1.5}\text{Te}_3$ (BST) fillers to optimize interfacial carrier transport of PEDOT:PSS/ BST, as illustrated in **Figure 1.13(a)** [156]. **Figure 1.13 (b–d)** shows the fabricated FTE material and FTEG. To enhance σ , highly crystallized PEDOT:PSS was obtained by subsequent treatment of DMSO polar solvent and concentrated H_2SO_4 . Meanwhile, the CuTe layer between PEDOT:PSS and BST decreases the interfacial contact resistance, which enables more carriers to transport through the interface, thereby further boosting σ to 2270 S cm^{-1} . Owing to the interfacial energy filtering effect, S reached up to $37.1 \mu\text{V K}^{-1}$, leading to a high $S^2\sigma$ value of $312 \mu\text{W m}^{-1} \text{K}^{-2}$ at room temperature with 0.05 wt% Cu coating and 4 wt% BST filler content, as shown in **Figure 1.13(d)**. The based FTEG can generate a remarkably thermovoltage of $\sim 7.7 \text{ mV}$ at ΔT of 15 K. A proton irradiation method was adopted to treat the surface of Bi_2Te_3 fillers[157], creating additional structure defects in Bi_2Te_3 , which facilitates the decoupling σ and S of the PEDOT:PSS/ Bi_2Te_3 composite. In addition, the interfacial barrier energy can be appropriate tuned by controlling the PSS/PEDOT ratio and the work function of PEDOT:PSS via a polar solvent vapor annealing technique, leading to the decoupling of σ and S with maximum $S^2\sigma$ of $226 \mu\text{W m}^{-1} \text{K}^{-2}$ in PEDOT:PSS/ Bi_2Te_3 NWs composites[158]. A double-carrier filtering effect can be realized in Te/PEDOT: PSS/ Cu_7Te_4 ternary composites, which consist of PEDOT:PSS coated Te (PC-Te) nanorods and PEDOT:PSS-coated Cu_7Te_4 (PC- Cu_7Te_4) nanorods[159]. Such ternary composite has an increased $S^2\sigma$ value of $112.3 \mu\text{W m}^{-1} \text{K}^{-2}$ at 380 K. The improved thermoelectric performance can be attributed to the synergetic effect of the individual thermoelectric properties of PC-Te and PC- Cu_7Te_4 nanorods and the double-carrier filtering effect at interfaces between them. In summary, despite some advanced fabrications or approaches have been explored, the optimization of interfacial carrier transport is still the barriers to effectively enhance the thermoelectric performance of organic/inorganic hybrids.

Conducting polymer/tellurium-based composites: Due to their superior TE performance at room temperature (RT), Te-based (Bi_2Te_3 , Te) inorganic materials are one of the best RT TE materials[160-162], which have been widely used in conducting polymers/inorganic composites. For examples, PEDOT NWs/Te NWs composite was fabricated with different Te NWs loadings[163]. The $S^2\sigma$ value of $29.05 \mu\text{W m}^{-1} \text{K}^{-2}$ was observed in the PEDOT NWs/Te NWs composite with 30 wt% Te NWs[163]. A free-standing Te-coated PEDOT NW film shows an excellent $S^2\sigma$ value of $240 \mu\text{W m}^{-1} \text{K}^2$ [164]. Another PEDOT:PSS/ Bi_2Te_3 based FTEGs can generate output voltage of 4.8 mV and output power of 16.9 nW at a ΔT of 47.2 K[165].

Conducting polymer/2D layer material composites: 2D layer materials, including black phosphorus (BP) [165], transition metal dichalcogenides (TMDs) (MoS_2 , TiS_2)[166], selenide or sulfide compounds (SnSe [167],

Cu₂Se[156,168], SnS[169]), MXene (Ti₃C₂T_x)[170], and layered double hydroxides (LDHs)[171], are important families of thermoelectric materials. The transports of carriers and phonons in these materials have been confined within in-plane 2D layers[172]. For examples, low cost BP shows potential thermoelectric application because of its intrinsically high μ ($\sim 1000 \text{ cm}^2 \text{ V}^{-1} \text{ s}^{-1}$) and S [173]. Chemically exfoliated MoS₂ nanosheets with metallic 1 T phase show a $S^2\sigma$ value of $73.1 \text{ } \mu\text{W m}^{-1} \text{ K}^{-2}$ at room temperature[174]. Furthermore, the thermoelectric properties of exfoliated 2D TMDs have been reported to depend on their thickness. For examples, few-layer (two-layer) MoS₂ exhibits 6-times larger σ than 23 layer MoS₂[175]. Monolayer MoS₂ shows enhanced $S^2\sigma$ due to the higher T induced by compressive strain[176]. Therefore, a hybrid of conducting polymer and 2D layer material is expected to have enhanced thermoelectric properties with maintained high flexibility. Novak et al used BP as nanofillers to improve $S^2\sigma$ of PEDOT:PSS from $17.3 \text{ } \mu\text{W m}^{-1} \text{ K}^{-2}$ to $36.2 \text{ } \mu\text{W m}^{-1} \text{ K}^{-2}$ [177]. A simple layer-by-layer (LBL) assembly approach was developed to construct PEDOT:PSS/MoS₂ nanosheets to achieve high $S^2\sigma$ of $41.6 \text{ } \mu\text{W m}^{-1} \text{ K}^{-2}$ [178].

Reference

- [1] T. Mori, S. Priya, MRS Bull. 43 (2018) 176-180.
- [2] L.E. Bell, Science 321 (2008) 1457-1461.
- [3] J.R. Sootsman, C. Duck Young, K. Mercouri G., Angew. Chem. Int. Ed. 48 (2009) 8616-8639.
- [4] Z.-G. Chen, G. Han, L. Yang, L. Cheng, J. Zou, Prog. Nat. Sci. 22 (2012) 535-549.
- [5] W. Liu, X. Yan, G. Chen, Z. Ren, Nano Energy 1 (2012) 42-56.
- [6] Q. Xu, B. Deng, L. Zhang, S. Lin, Z. Han, Q. Zhou, J. Li, Y. Zhu, F. Jiang, Q. Li, P. Zhang, X. Zhang, G. Chen, W. Liu, Cell Rep. Physical Science 3 (2022) 100780.
- [7] L. Li, W.D. Liu, Q. Liu, Z.G. Chen, Adv. Funct. Mater. 32 (2022) 2200548.
- [8] B. Hu, X.-L. Shi, J. Zou, Z.-G. Chen, Chem. Eng. J. 437 (2022) 135268.
- [9] L. Zhang, X.-L. Shi, Y.-L. Yang, Z.-G. Chen, Mater. Today 46 (2021) 62-108.
- [10] Z. Liu, N. Sato, W. Gao, K. Yubuta, N. Kawamoto, M. Mitome, K. Kurashima, Y. Owada, K. Nagase, C.-H. Lee, J. Yi, K. Tsuchiya, T. Mori, Joule 5 (2021) 1196-1208.
- [11] B. Poudel, Q. Hao, Y. Ma, Y. Lan, A. Minnich, B. Yu, X. Yan, D. Wang, A. Muto, D. Vashaee, X. Chen, J. Liu, M.S. Dresselhaus, G. Chen, Z. Ren, Science 320 (2008) 634-638.
- [12] Z. Liu, W. Gao, H. Oshima, K. Nagase, C.H. Lee, T. Mori, Nat. Commun. 13 (2022) 1120.
- [13] L. Su, D. Wang, S. Wang, B. Qin, Y. Wang, Y. Qin, Y. Jin, C. Chang, L.-D. Zhao, Science 375 (2022) 1385-1389.
- [14] T. Mori, Small 13 (2017) 1702013.
- [15] A.U. Khan, K. Kobayashi, D.-M. Tang, Y. Yamauchi, K. Hasegawa, M. Mitome, Y. Xue, B. Jiang, K. Tsuchiya, D. Golberg, Y. Bando, T. Mori, Nano Energy 31 (2017) 152-159.
- [16] T.G. Novak, K. Kim, S. Jeon, Nanoscale 11 (2019) 19684-19699.
- [17] K. Pietrzyk, J. Soares, B. Ohara, H. Lee, Appl. Energy 183 (2016) 218-228.
- [18] I. Petsagkourakisa, K. Tybrandta, X. Crispin, I. Ohkubo, N. Satoh, T. Mori, Sci. Technol. Adv. Mater. 19 (2018) 836-862.
- [19] S. Wang, G. Zuo, J. Kim, H. Sirringhaus, Prog. Polym. Sci. 129 (2022) 101548.

- [20] S. Masoumi, S. O'Shaughnessy, A. Pakdel, *Nano Energy* 92 (2022) 106774.
- [21] G. Prunet, F. Pawula, G. Fleury, E. Cloutet, A.J. Robinson, G. Hadziioannou, A. Pakdel, *Mater. Today Phys.* 18 (2021) 100402.
- [22] D. Park, M. Kim, J. Kim, *Polymers* 13 (2021) 210.
- [23] N. Nandihalli, C.-J. Liu, T. Mori, *Nano Energy* 78 (2020) 105186.
- [24] S. Lee, S. Kim, A. Pathak, A. Tripathi, T. Qiao, Y. Lee, H. Lee, H.Y. Woo, *Macromol. Res.* 28 (2020) 531-552.
- [25] X.L. Shi, J. Zou, Z.G. Chen, *Chem. Rev.* 120 (2020) 7399-7515.
- [26] N. Tsujii, F. Meng, K. Tsuchiya, S. Maruyama, T. Mori, *J. Electron. Mater.* 45 (2015) 1642-1647.
- [27] G.J. Snyder, E.S. Toberer, *Complex thermoelectric materials*, In: *Materials for Sustainable Energy*, World Scientific Publishing Co. Pte. Ltd, Singapore, (2010) 101-110.
- [28] H.J. Goldsmid, *Introduction to thermoelectricity*, Springer, (2010).
- [29] R.A. Kishore, S. Priya, *Materials* 11 (2018) 1433.
- [30] N.A. Sidorenko, L.D. Ivanova, *Inorg. Mater.* 37 (2001) 331-335.
- [31] Y. Gelbstein, Z. Dashevsky, M.P. Dariel, *Phys. Rev., B Condens. Matter* 363 (2005) 196-205.
- [32] D. Wu, L.-D. Zhao, S. Hao, Q. Jiang, F. Zheng, J.W. Doak, H. Wu, H. Chi, Y. Gelbstein, C. Uher, C. Wolverton, M. Kanatzidis, J. He, *J. Am. Chem. Soc.* 136 (2014) 11412-11419.
- [33] J. Li, X. Zhang, S. Lin, Z. Chen, Y. Pei, *Chem. Mater.* 29 (2017) 605-611.
- [34] L.-D. Zhao, X. Zhang, H. Wu, G. Tan, Y. Pei, Y. Xiao, C. Chang, D. Wu, H. Chi, L. Zheng, S. Gong, C. Uher, J. He, M.G. Kanatzidis, *J. Am. Chem. Soc.* 138 (2016) 2366-2373.
- [35] M. Zhou, Z.M. Gibbs, H. Wang, Y. Han, L. Li, G.J. Snyder, *Appl. Phys. Lett.* 109 (2016) 042102.
- [36] G.J. Snyder, E.S. Toberer, *Nat Mater* 7 (2008) 105-114.
- [37] J. Wei, L. Yang, Z. Ma, P. Song, M. Zhang, J. Ma, F. Yang, X. Wang, *J. Mater. Sci.* 55 (2020) 12642-12704.
- [38] N. Tsujii, T. Mori, Y. Isoda, *J. Electron. Mater.* 43 (2014) 2371-2375.
- [39] N. Tsujii, T. Mori, *Appl. Phys. Express* 6 (2013) 043001.
- [40] T. N., *J. Electron. Mater.* 6 (2013) 1974-1977.
- [41] N. Oueldna, A. Portavoce, M. Bertoglio, A. Campos, A. Kammouni, K. Hoummada, *J. Alloys Compd.* 900 (2022) 163534.
- [42] Y. Liao, J.-L. Chen, C. Liu, J. Liang, Q. Zhou, P. Wang, L. Miao, *J. Mater. Chem. C* 10 (2022) 3360-3367.
- [43] G. Tan, F. Shi, J.W. Doak, H. Sun, L.-D. Zhao, P. Wang, C. Uher, C. Wolverton, V.P. Dravid, M.G. Kanatzidis, *Energy Environ. Sci.* 8 (2015) 267-277.
- [44] Q. Zhang, F. Cao, W. Liu, K. Lukas, B. Yu, S. Chen, C. Opeil, D. Broido, G. Chen, Z. Ren, *J. Am. Chem. Soc.* 134 (2012) 10031-10038.
- [45] A.F. Ioffe, L.S. Stil'bans, E.K. Iordanishvili, T.S. Stavitskaya, A. Gelbtuch, G. Vineyard, *Phys. Today* 12 (1959) 42.
- [46] Q. Tao, F. Meng, Z. Zhang, Y. Cao, Y. Tang, J. Zhao, X. Su, C. Uher, X. Tang, *Mater. Today Phys.* 20 (2021) 100472.
- [47] B. Abeles, *Phys. Rev.* 131 (1963) 1906-1911.
- [48] S. Liu, G. Li, M. Lan, T. Baba, T. Baba, T. Mori, Q. Wang, *Small* 17 (2021) e2100554.
- [49] L.D. Hicks, M.S. Dresselhaus, *MRS Online Proceedings Library* 326 (2011) 413.

- [50] K. Biswas, J. He, I.D. Blum, C.I. Wu, T.P. Hogan, D.N. Seidman, V.P. Dravid, M.G. Kanatzidis, *Nature* 489 (2012) 414-418.
- [51] A. Pakdel, Q. Guo, V. Nicolosi, T. Mori, *J. Mater. Chem. A* 6 (2018) 21341-21349.
- [52] J.J. Urban, D.V. Talapin, E.V. Shevchenko, C.R. Kagan, C.B. Murray, *Nat. Mater.* 6 (2007) 115-121.
- [53] A. Ishida, T. Yamada, T. Tsuchiya, Y. Inoue, S. Takaoka, T. Kita, *Appl. Phys. Lett.* 95 (2009) 122106.
- [54] T.C. Harman, P.J. Taylor, M.P. Walsh, B.E. LaForge, *Science* 297 (2002) 2229-2232.
- [55] L.D. Hicks, M.S. Dresselhaus, *Phys. Rev. B* 47 (1993) 12727-12731.
- [56] A. Boukai, K. Xu, J.R. Heath, *Adv. Mater.* 18 (2006) 864-869.
- [57] M. S. Dresselhaus, G. Dresselhaus, X. Sun, Z. Zhang, S. B. Cronin, T. Koga, J.Y. Ying, G. Chen, *Microscale Thermophys. Eng.* 3 (1999) 89-100.
- [58] Y.-M. Lin, M.S. Dresselhaus, *Phys. Rev. B* 68 (2003) 075304.
- [59] A.I. Boukai, Y. Bunimovich, J. Tahir-Kheli, J.-K. Yu, W.A. Goddard Iii, J.R. Heath, *Nature* 451 (2008) 168-171.
- [60] R. Venkatasubramanian, E. Siivola, T. Colpitts, B. O'Quinn, *Nature* 413 (2001) 597-602.
- [61] F. Suarez, A. Nozariasbmarz, D. Vashaee, M.C. Öztürk, *Energy Environ. Sci.* 9 (2016) 2099-2113.
- [62] J. Zhang, P. Cheng, C. Zhang, G. Ding, L. Duan, J. Shao, Q. Wang, *The Journal of Engineering* 2016 (2016) 315-317.
- [63] C. Fu, H. Wu, Y. Liu, J. He, X. Zhao, T. Zhu, *Adv. Sci.* 3 (2016) 1600035.
- [64] G.H. Zhu, H. Lee, Y.C. Lan, X.W. Wang, G. Joshi, D.Z. Wang, J. Yang, D. Vashaee, H. Guilbert, A. Pillitteri, M.S. Dresselhaus, G. Chen, Z.F. Ren, *Phys. Rev. Lett.* 102 (2009) 196803.
- [65] H.-S. Kim, S.D. Kang, Y. Tang, R. Hanus, G. Jeffrey Snyder, *Mater. Horizons* 3 (2016) 234-240.
- [66] B.F. Donovan, B.M. Foley, J.F. Ihlefeld, J.-P. Maria, P.E. Hopkins, *Appl. Phys. Lett.* 105 (2014) 082907.
- [67] Q. Zhu, S. Wang, X. Wang, A. Suwardi, M.H. Chua, X.Y.D. Soo, J. Xu, *Nanomicro Lett.* 13 (2021) 119.
- [68] W. Kim, J. Zide, A. Gossard, D. Klenov, S. Stemmer, A. Shakouri, A. Majumdar, *Phys. Rev. Lett.* 96 (2006) 045901.
- [69] L. Yang, Z.-G. Chen, G. Han, M. Hong, J. Zou, *Acta Mater.* 113 (2016) 140-146.
- [70] Y. Pei, N.A. Heinz, G.J. Snyder, *J. Mater. Chem.* 21 (2011) 18256.
- [71] J.P. Heremans, B. Wiendlocha, A.M. Chamoire, *Energy Environ. Sci.* 5 (2012) 5510-5530.
- [72] D. Bilc, S.D. Mahanti, E. Quarez, K.F. Hsu, R. Pcionek, M.G. Kanatzidis, *Phys. Rev. Lett.* 93 (2004) 146403.
- [73] Y. Pei, X. Shi, A. LaLonde, H. Wang, L. Chen, G.J. Snyder, *Nature* 473 (2011) 66-69.
- [74] G. Tan, F. Shi, S. Hao, H. Chi, L.-D. Zhao, C. Uher, C. Wolverton, V.P. Dravid, M.G. Kanatzidis, *J. Am. Chem. Soc.* 137 (2015) 5100-5112.
- [75] M. Hong, Z.-G. Chen, Y. Pei, L. Yang, J. Zou, *Phys. Rev. B* 94 (2016) 161201.
- [76] N. Boukhris, H. Meradji, S. Ghemid, S. Drablia, F. El Haj Hassan, *Phys. Scr.* 83 (2011) 065701.
- [77] K. Hoang, S.D. Mahanti, M.G. Kanatzidis, *Phys. Rev. B* 81 (2010) 115106.
- [78] L.D. Zhao, H.J. Wu, S.Q. Hao, C.I. Wu, X.Y. Zhou, K. Biswas, J.Q. He, T.P. Hogan, C. Uher, C. Wolverton, V.P. Dravid, M.G. Kanatzidis, *Energy Environ. Sci.* 6 (2013) 3346.
- [79] T. Zhu, Y. Liu, C. Fu, J.P. Heremans, J.G. Snyder, X. Zhao, *Adv. Mater.* 29 (2017) 1605884.
- [80] Y. Pei, A.D. LaLonde, N.A. Heinz, G.J. Snyder, *Adv. Energy Mater.* 2 (2012) 670-675.
- [81] J.-H. Bahk, A. Shakouri, *Appl. Phys. Lett.* 105 (2014) 052106.
- [82] Y. Pei, Z.M. Gibbs, A. Gloskovskii, B. Balke, W.G. Zeier, G.J. Snyder, *Adv. Energy Mater.* 4 (2014) 1400486.

- [83] G. Nimtz, B. Schlicht, *Narrow gap lead salts Narrow Gap Semiconductors* ed G Hohler. Berlin: Springer: (1983) 1-117.
- [84] W. Liu, X. Tan, K. Yin, H. Liu, X. Tang, J. Shi, Q. Zhang, C. Uher, *Phys. Rev. Lett.* 108 (2012) 166601.
- [85] S. Wang, Y. Sun, J. Yang, B. Duan, L. Wu, W. Zhang, J. Yang, *Energy Environ. Sci.* 9 (2016) 3436-3447.
- [86] J. Zhang, R. Liu, N. Cheng, Y. Zhang, J. Yang, C. Uher, X. Shi, L. Chen, W. Zhang, *Adv. Mater.* 26 (2014) 3848-3853.
- [87] W.G. Zeier, H. Zhu, Z.M. Gibbs, G. Ceder, W. Tremel, G.J. Snyder, *J. Mater. Chem. C* 2 (2014) 10189-10194.
- [88] Z. Liang, M.J. Boland, K. Butrouna, D.R. Strachan, K.R. Graham, *J. Mater. Chem. A* 5 (2017) 15891-15900.
- [89] A.J. Minnich, M.S. Dresselhaus, Z.F. Ren, G. Chen, *Energy Environ. Sci.* 2 (2009) 466.
- [90] S.V. Faleev, F. Léonard, *Phys. Rev. B* 77 (2008) 214304.
- [91] J. Kim, K.H. Lee, S.-D. Kim, J.-H. Lim, Nosang V. Myung, *J. Mater. Chem. A* 6 (2018) 349-356.
- [92] J.H. Kim, S. Oh, W.H. Sohn, J.-S. Rhyee, S.-D. Park, H. Kang, D. Ahn, *Acta Mater.* 100 (2015) 32-38.
- [93] M. Hong, Z.-G. Chen, L. Yang, G. Han, J. Zou, *Adv. Electron. Mater.* 1 (2015) 1500025.
- [94] C. Xiao, K. Li, J. Zhang, W. Tong, Y. Liu, Z. Li, P. Huang, B. Pan, H. Su, Y. Xie, *Mater. Horiz.* 1 (2014) 81-86.
- [95] Y. Wang, N.S. Rogado, R.J. Cava, N.P. Ong, *Nature* 423 (2003) 425-428.
- [96] K. Park, K. Ahn, J. Cha, S. Lee, S.I. Chae, S.-P. Cho, S. Rye, J. Im, J. Lee, S.-D. Park, M.J. Han, I. Chung, T. Hyeon, *J. Am. Chem. Soc.* 138 (2016) 14458-14468.
- [97] Z. Chen, B. Ge, W. Li, S. Lin, J. Shen, Y. Chang, R. Hanus, G.J. Snyder, Y. Pei, *Nat. Commun.* 8 (2017) 13828.
- [98] S.I. Kim, K.H. Lee, H.A. Mun, H.S. Kim, S.W. Hwang, J.W. Roh, D.J. Yang, W.H. Shin, X.S. Li, Y.H. Lee, G.J. Snyder, S.W. Kim, *Science* 348 (2015) 109-114.
- [99] Y. Zheng, Y. Luo, C. Du, B. Zhu, Q. Liang, H.H. Hng, K. Hippalgaonkar, J. Xu, Q. Yan, *Mater. Chem. Front.* 1 (2017) 2457-2473.
- [100] B. Xu, T. Feng, M.T. Agne, L. Zhou, X. Ruan, G.J. Snyder, Y. Wu, *Angew. Chem. Int. Ed.* 56 (2017) 3546-3551.
- [101] Hideki Shirakawa, Edwin J. Louis, Alan G. Macdiarmid, Chwan K. Ching, A.J. Heeger, *J. Chem. Soc., Chem. Commun.* 16 (1977) 578-580.
- [102] L. Zhang, K. Yang, R. Chen, Y. Zhou, S. Chen, Y. Zheng, M. Li, C. Xu, X. Tang, Z. Zang, K. Sun, *Adv. Electron. Mater.* 6 (2020) 1900648.
- [103] K. Yu, S. Rich, S. Lee, K. Fukuda, T. Yokota, T. Someya, *Proc. IEEE* 107 (2019) 2137-2154.
- [104] Z. Ma, W. Shi, K. Yan, L. Pan, G. Yu, *Chem. Sci.* 10 (2019) 6232-6244.
- [105] Y. Lu, M.C. Biswas, Z. Guo, J.-W. Jeon, E.K. Wujcik, *Biosens. Bioelectron.* 123 (2019) 167-177.
- [106] H. Song, K. Cai, *Energy* 125 (2017) 519-525.
- [107] O. Bubnova, Z.U. Khan, A. Malti, S. Braun, M. Fahlman, M. Berggren, X. Crispin, *Nat. Mater.* 10 (2011) 429-433.
- [108] Z. Han, A. Fina, *Prog. Polym. Sci.* 36 (2011) 914-944.
- [109] T. Zhang, K. Li, C. Li, S. Ma, H.H. Hng, L. Wei, *Adv. Electron. Mater.* 3 (2017) 1600554.
- [110] J. L. Bredas, G.B. Street, *Acc. Chem. Res.* 18 (1985) 309-315.
- [111] M. Bharti, A. Singh, S. Samanta, D.K. Aswal, *Prog. Mater Sci.* 93 (2018) 270-310.
- [112] Y. Zhang, B. de Boer, P.W.M. Blom, *Phys. Rev. B* 81 (2010) 085201.
- [113] Y.W. Park, C.O. Yoon, B.C. Na, H. Shirakawa, K. Akagi, *Synth. Met.* 41 (1991) 27-32.
- [114] C.K. Chiang, C.R. Fincher, Y.W. Park, A.J. Heeger, H. Shirakawa, E.J. Louis, S.C. Gau, A.G. MacDiarmid, *Phys. Rev. Lett.* 39 (1977) 1098-1101.

- [115] A.B. Kaiser, *Adv. Mater.* 13 (2001) 927-941.
- [116] R. Kroon, D.A. Mengistie, D. Kiefer, J. Hynynen, J.D. Ryan, L. Yu, C. Muller, *Chem. Soc. Rev.* 45 (2016) 6147-6164.
- [117] B. Russ, A. Glaudell, J.J. Urban, M.L. Chabiny, R.A. Segalman, *Nat. Rev. Mater.* 1 (2016) 16050.
- [118] Q. Wang, Q. Yao, J. Chang, L. Chen, *J. Mater. Chem.* 22 (2012) 17612.
- [119] K. Lee, S. Cho, S. Heum Park, A.J. Heeger, C.-W. Lee, S.-H. Lee, *Nature* 441 (2006) 65-68.
- [120] J. Tarascon, M. Armand, *World Scientific* (2011) 171-179.
- [121] Q. Jiang, H. Yan, J. Khaliq, H. Ning, S. Grasso, K. Simpson, M.J. Reece, *J. Mater. Chem. A* 2 (2014) 5785-5790.
- [122] Y. Zhou, L. Wang, H. Zhang, Y. Bai, Y. Niu, H. Wang, *Appl. Phys. Lett.* 101 (2012) 012903.
- [123] C.L. Choy, *Polymer* 18 (1977) 984-1004.
- [124] K. Kurabayashi, *Int. J. Thermophys.* 22 (2001) 277-288.
- [125] M. He, J. Ge, Z. Lin, X. Feng, X. Wang, H. Lu, Y. Yang, F. Qiu, *Energy Environ. Sci.* 5 (2012) 8351.
- [126] T. Stöcker, A. Köhler, R. Moos, *J. Polym. Sci., Part B: Polym. Phys.* 50 (2012) 976-983.
- [127] H.J. Lee, G. Anoop, H.J. Lee, C. Kim, J.-W. Park, J. Choi, H. Kim, Y.-J. Kim, E. Lee, S.-G. Lee, Y.-M. Kim, J.-H. Lee, J.Y. Jo, *Energy Environ. Sci.* 9 (2016) 2806-2811.
- [128] K. Zhang, Y. Zhang, S. Wang, *Sci. Rep.* 3 (2013) 3448.
- [129] Y. Du, K.F. Cai, S.Z. Shen, R. Donelsonand, J.Y. Xu, H.X. Wang, T. Lin, *RSC Adv.* 7 (2017) 43737-43742.
- [130] D. Neusser, C. Malacrida, M. Kern, Y.M. Gross, J. van Slageren, S. Ludwigs, *Chem. Mater.* 32 (2020) 6003-6013.
- [131] C.J. Boyle, M. Upadhyaya, P. Wang, L.A. Renna, M. Lu-Díaz, S. Pyo Jeong, N. Hight-Huf, L. Korugic-Karasz, M.D. Barnes, Z. Aksamija, D. Venkataraman, *Nat. Commun.* 10 (2019) 2827.
- [132] R.B. Aïch, N. Blouin, A. Bouchard, M. Leclerc, *Chem. Mater.* 21 (2009) 751-757.
- [133] J. Hynynen, D. Kiefer, L. Yu, R. Kroon, R. Munir, A. Amassian, M. Kemerink, C. Müller, *Macromolecules* 50 (2017) 8140-8148.
- [134] I. Salzmann, G. Heimel, M. Oehzelt, S. Winkler, N. Koch, *Acc. Chem. Res.* 49 (2016) 370-378.
- [135] E. Lim, K.A. Peterson, G.M. Su, M.L. Chabiny, *Chem. Mater.* 30 (2018) 998-1010.
- [136] D. Rawlings, E.M. Thomas, R.A. Segalman, M.L. Chabiny, *Chem. Mater.* 31 (2019) 8820-8829.
- [137] L. Zhang, X.-L. Shi, Y.-L. Yang, Z.-G. Chen, *Mater. Today* 46 (2021) 62-108.
- [138] Z.U. Khan, O. Bubnova, M.J. Jafari, R. Brooke, X. Liu, R. Gabrielsson, T. Ederth, D.R. Evans, J.W. Andreasen, M. Fahlman, X. Crispin, *J. Mater. Chem. C* 3 (2015) 10616-10623.
- [139] C. Wang, K. Sun, J. Fu, R. Chen, M. Li, Z. Zang, X. Liu, B. Li, H. Gong, J. Ouyang, *Adv. Sustain. Syst.* 2 (2018) 1800085.
- [140] F. Kong, C. Liu, H. Song, J. Xu, Y. Huang, H. Zhu, J. Wang, *Synth. Met.* 185-186 (2013) 31-37.
- [141] Y. Lu, J.-Y. Wang, J. Pei, *Chem. Mater.* 31 (2019) 6412-6423.
- [142] B.D. Naab, S. Guo, S. Olthof, E.G.B. Evans, P. Wei, G.L. Millhauser, A. Kahn, S. Barlow, S.R. Marder, Z. Bao, *J. Am. Chem. Soc.* 135 (2013) 15018-15025.
- [143] K.I. Bolotin, K.J. Sikes, Z. Jiang, M. Klima, G. Fudenberg, J. Hone, P. Kim, H.L. Stormer, *Solid State Commun.* 146 (2008) 351-355.
- [144] K. Kanahashi, M. Ishihara, M. Hasegawa, H. Ohta, T. Takenobu, *NPJ 2D Mater. Appl.* 3 (2019) 44.

- [145] B.A. MacLeod, N.J. Stanton, I.E. Gould, D. Wesenberg, R. Ihly, Z.R. Owczarczyk, K.E. Hurst, C.S. Fewox, C.N. Folmar, K. Holman Hughes, B.L. Zink, J.L. Blackburn, A.J. Ferguson, *Energy Environ. Sci.* 10 (2017) 2168-2179.
- [146] Y. Wang, L. Yang, X.L. Shi, X. Shi, L. Chen, M.S. Dargusch, J. Zou, Z.G. Chen, *Adv. Mater.* 31 (2019) 1807916.
- [147] B. Abad, I. Alda, P. Díaz-Chao, H. Kawakami, A. Almarza, D. Amantia, D. Gutierrez, L. Aubouy, M. Martín-González, *J. Mater. Chem. A* 1 (2013) 10450-10457.
- [148] X. Zhou, C. Pan, A. Liang, L. Wang, W.-Y. Wong, *Compos. Sci. Technol.* 145 (2017) 40-45.
- [149] D. Yoo, J. Kim, J.H. Kim, *Nano Res.* 7 (2014) 717-730.
- [150] D.L. Stevens, A. Parra, J.C. Grunlan, *ACS Appl. Energy Mater.* 2 (2019) 5975-5982.
- [151] C. Cho, B. Stevens, J.-H. Hsu, R. Bureau, D.A. Hagen, O. Regev, C. Yu, J.C. Grunlan, *Adv. Mater.* 27 (2015) 2996-3001.
- [152] C.J. An, Y.C. Lee, Y.H. Kang, S.Y. Cho, *Carbon* 124 (2017) 662-668.
- [153] P.-a. Zong, J. Liang, P. Zhang, C. Wan, Y. Wang, K. Koumoto, *ACS Appl. Energy Mater.* 3 (2020) 2224-2239.
- [154] Y. Lu, Y. Song, F. Wang, *Mater. Chem. Phys.* 138 (2013) 238-244.
- [155] Y.Y. Hsieh, Y. Zhang, L. Zhang, Y. Fang, S.N. Kanakaraaj, J.H. Bahk, V. Shanov, *Nanoscale* 11 (2019) 6552-6560.
- [156] Y. Wang, M. Hong, W.-D. Liu, X.-L. Shi, S.-D. Xu, Q. Sun, H. Gao, S. Lu, J. Zou, Z.-G. Chen, *Chem. Eng. J.* 397 (2020) 125360.
- [157] G. Goo, G. Anoop, S. Unithrattil, W.S. Kim, H.J. Lee, H.B. Kim, M.H. Jung, J. Park, H.C. Ko, J.Y. Jo, *Adv. Electron. Mater.* 5 (2019) 1800786.
- [158] W.S. Kim, G. Anoop, I.-S. Jeong, H.J. Lee, H.B. Kim, S.H. Kim, G.W. Goo, H. Lee, H.J. Lee, C. Kim, J.-H. Lee, B.S. Mun, J.-W. Park, E. Lee, J.Y. Jo, *Nano Energy* 67 (2020) 104207.
- [159] Y. Lu, Y. Qiu, Q. Jiang, K. Cai, Y. Du, H. Song, M. Gao, C. Huang, J. He, D. Hu, *ACS Appl. Mater. Interfaces* 10 (2018) 42310-42319.
- [160] Y. Wang, W.-D. Liu, X.-L. Shi, M. Hong, L.-J. Wang, M. Li, H. Wang, J. Zou, Z.-G. Chen, *Chem. Eng. J.* 391 (2020) 123513.
- [161] Y. Wang, W.-D. Liu, H. Gao, L.-J. Wang, M. Li, X.-L. Shi, M. Hong, H. Wang, J. Zou, Z.-G. Chen, *ACS Appl. Mater. Interfaces* 11 (2019) 31237-31244.
- [162] M. Tan, W.-D. Liu, X.-L. Shi, J. Shang, H. Li, X. Liu, L. Kou, M. Dargusch, Y. Deng, Z.-G. Chen, *Nano Energy* 78 (2020) 105379.
- [163] X. Hu, K. Zhang, J. Zhang, S. Wang, Y. Qiu, *ACS Appl. Energy Mater.* 1 (2018) 4883-4890.
- [164] D. Ni, H. Song, Y. Chen, K. Cai, *J. Materiomics* 6 (2020) 364-370.
- [165] Yong Du, Xin Liu, Jiayue Xu, S.Z. Shen, *Mater. Chem. Front.* 3 (2019) 1328.
- [166] T.G. Novak, H. Shin, J. Kim, K. Kim, A. Azam, C.V. Nguyen, S.H. Park, J.Y. Song, S. Jeon, *ACS Appl. Mater. Interfaces* 10 (2018) 17957-17962.
- [167] X.-L. Shi, W.-Y. Chen, X. Tao, J. Zou, Z.-G. Chen, *Mater. Horizons* 7 (2020) 3065-3096.
- [168] W.-D. Liu, X.-L. Shi, R. Moshwan, L. Yang, Z.-G. Chen, J. Zou, *Chem. Eng. J.* 375 (2019) 121996.
- [169] W.-D. Liu, X.-L. Shi, Z.-J. Lin, Q. Sun, G. Han, Z.-G. Chen, J. Zou, *ACS Appl. Energy Mater.* 3 (2020) 2192-2199.
- [170] X. Guan, W. Feng, X. Wang, R. Venkatesh, J. Ouyang, *ACS Appl. Mater. Interfaces* 12 (2020) 13013-13020.
- [171] Q. Xu, S.-M. Xu, R. Tian, C. Lu, *ACS Appl. Mater. Interfaces* 12 (2020) 13371-13377.

- [172] M. Ahmadi, O. Zabihi, S. Jeon, M. Yoonessi, A. Dasari, S. Ramakrishna, M. Naebe, *J. Mater. Chem. A* 8 (2020) 845-883.
- [173] L. Li, Y. Yu, G.J. Ye, Q. Ge, X. Ou, H. Wu, D. Feng, X.H. Chen, Y. Zhang, *Nat. Nanotechnol.* 9 (2014) 372-377.
- [174] H. Huang, Y. Cui, Q. Li, C. Dun, W. Zhou, W. Huang, L. Chen, C.A. Hewitt, D.L. Carroll, *Nano Energy* 26 (2016) 172-179.
- [175] M. Kayyalha, J. Maassen, M. Lundstrom, L. Shi, Y.P. Chen, *J. Appl. Phys.* 120 (2016) 134305.
- [176] Dimple, N. Jena, A. De Sarkar, *J. Phys.: Condens. Matter* 29 (2017) 225501.
- [177] T.G. Novak, H. Shin, J. Kim, K. Kim, A. Azam, C.V. Nguyen, S.H. Park, J.Y. Song, S. Jeon, *ACS Appl Mater Interfaces* 10 (2018) 17957-17962.
- [178] X. Wang, F. Meng, Q. Jiang, W. Zhou, F. Jiang, T. Wang, X. Li, S. Li, Y. Lin, J. Xu, *ACS Appl. Energy Mater.* 1 (2018) 3123-3133.

Chapter 2 Fabrication and thermoelectric Properties of MoS₂/Bi₂Te₃ composites

2.1 Introduction

Bi₂Te₃-based compounds are well-known as the best thermoelectric materials for room temperature applications. So far, significant progress has been made in enhancing ZT of Bi₂Te₃-based nanostructure[1-6]. Among of them, Bi₂Te₃/MoS₂ nanocomposites have attracted more and more attention because of its graphene-analogous structure MoS₂[7]and its physical properties, such as discretized density of states as well as high mobility, which provides the foundation for its high TE performance[8-10].

Recent studies reported that the mobility of monolayer MoS₂ can be increased by several times. Moreover, MoS₂ was reported to have very notable values of thermopower, but poor electrical conductivity, leading to a negligibly small value of the dimensionless thermoelectric figure of merit (ZT ~ 0.006 at the optimal doping and working temperature)[11]. To date, the studies of MoS₂ are limited as a thermoelectric material. Thus, similar to Bi₂Te₃/graphene heterostructures[12,13], the design and fabrication of Bi₂Te₃/MoS₂ composite materials seem to be a potentially attractive strategy for exploring novel TE nanocomposite to improve TE properties.

In this work, a series of Bi₂Te₃/X mol% MoS₂ (X = 0, 25, 50, 75) bulk nanocomposites have been prepared by hydrothermal reaction followed by reactive Spark Plasma Sintering (SPS). X-ray diffraction analysis (XRD) indicates that the native nanopowders, comprising of Bi₂Te₃/MoS₂ heterostructure, are highly reactive during the electric field-assisted sintering by SPS. The nano-sized MoS₂ particles react with the Bi₂Te₃ plates matrix forming a mixed-anion compound Bi₂Te₂S at the interface between the nanoplates. The transport properties characterizations revealed a significant influence of the nanocomposite structure formation on the native electrical conductivity, Seebeck coefficient, and thermal conductivity of the initial Bi₂Te₃ matrix. As a result, enhanced ZT values have been obtained in Bi₂Te₃/25 mol% MoS₂ over the temperature range of 300 - 475 K induced mainly by a significant increase of the electrical conductivity

2.2 Experimental section

2.2.1 Synthesis of hexagonal nanoplatelets of Bi₂Te₃ and Bi₂Te₃/MoS₂ composites

Hexagonal nanoplatelets of Bi₂Te₃ and Bi₂Te₃/MoS₂ heterostructures were synthesized as reported by our prior paper[14]. First, Bi₂O₃ (0.5515 g, 1.18 mmol), TeO₂ (0.5745 g, 3.60 mmol), and 4 M NaOH solution (6 mL) were added into a solution of PVP (0.96 g) in ethylene glycol (42 mL). The mixed yellow suspension was stirred vigorously for 30 min and transferred into a 50 mL Teflon-lined autoclave then sealed in a stainless-steel canister, which was heated at 200 °C for 4 h. After that, centrifugation was employed to the resulted gray precipitate, which was washed several times with distilled water followed by acetone, and dried in air at room temperature.

Second, $\text{Bi}_2\text{Te}_3/\text{MoS}_2$ heterostructure with 75 mol% MoS_2 was prepared as follows. The obtained Bi_2Te_3 (0.205 g, 2.56×10^{-4} mol) was added into 45 mL water and stirred for 30 min to get a dispersion. Ammonium tetrathiomolybdate (0.2 g, equivalent to 7.68×10^{-4} mol of MoS_2) was added to this dispersion following 15 min stirring. Hydrazine hydrate (5 mL) was added to the mixture and the stirring continued for another 15 min. The mixture was then transferred into a Teflon-lined autoclave, sealed, and heated in a hot air oven at 200 °C for 24 h. The black solid obtained was separated by centrifugation, washed several times with distilled water followed by acetone, and dried under ambient conditions. $\text{Bi}_2\text{Te}_3/\text{X}$ mol% MoS_2 heterostructures with X=0, 25, 50 were also synthesized. In all the cases, the mass of ammonium tetrathiomolybdate used was kept constant (200 mg).

2.2.2 Synthesis of $\text{Bi}_2\text{Te}_3/\text{X}$ mol% MoS_2 bulk samples

The resulting powders were loaded into a graphite die (Φ 10 mm) and sintered by spark plasma sintering (Dr. Sinter, SPS-322Lx) under a uniaxial pressure of 50 MPa. The sintering was performed in a partial argon atmosphere at 623 K for 5 min (heating and cooling rate of 100 K min^{-1}). The sintered pellets were then cut and polished to the required shapes and dimensions for the different characterizations. The densities measured by Archimedes' method were 6.58, 6.28, 5.74, and 4.64, respectively, for X = 0, 25, 50, and 75.

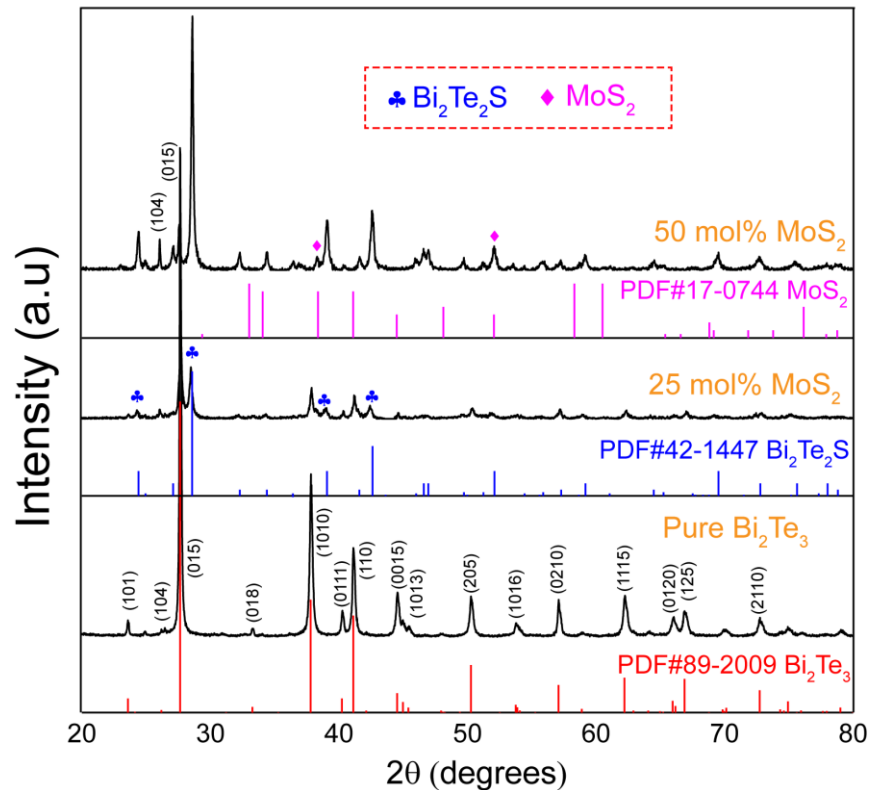


Figure 2.1 PXRD patterns of the $\text{Bi}_2\text{Te}_3/\text{X}$ mol% MoS_2 heterostructures (X=0, 25, 50) after SPS.

2.2.3 Chemical and structural characterization

The phase compositions were characterized by powder X-ray diffraction (Rigaku, Ultima III) with Cu K_{α} radiation. Microstructural and analysis of the samples were performed by a field-emission ultra-high resolution scanning electron microscope (SEM; SU4800 Hitachi) equipped with an energy-dispersive spectrometer (EDS).

2.2.4 Physical property measurements

The thermal diffusivity α and heat capacity C_p were measured using LFA-467 Hyperflash (Netzsch) under a flowing argon atmosphere (50 ml/min). The thermal conductivity κ was derived as a product of the sample's density (measured by Archimedes' method), thermal diffusivity, and heat capacity C_p . The sintered disks were cut into rectangular bars for simultaneous electrical conductivity and Seebeck coefficient measurements using a commercial instrument (ZEM-2, ULVAC Shinku-Riko, Japan) with a standard four-probe configuration under a helium atmosphere.

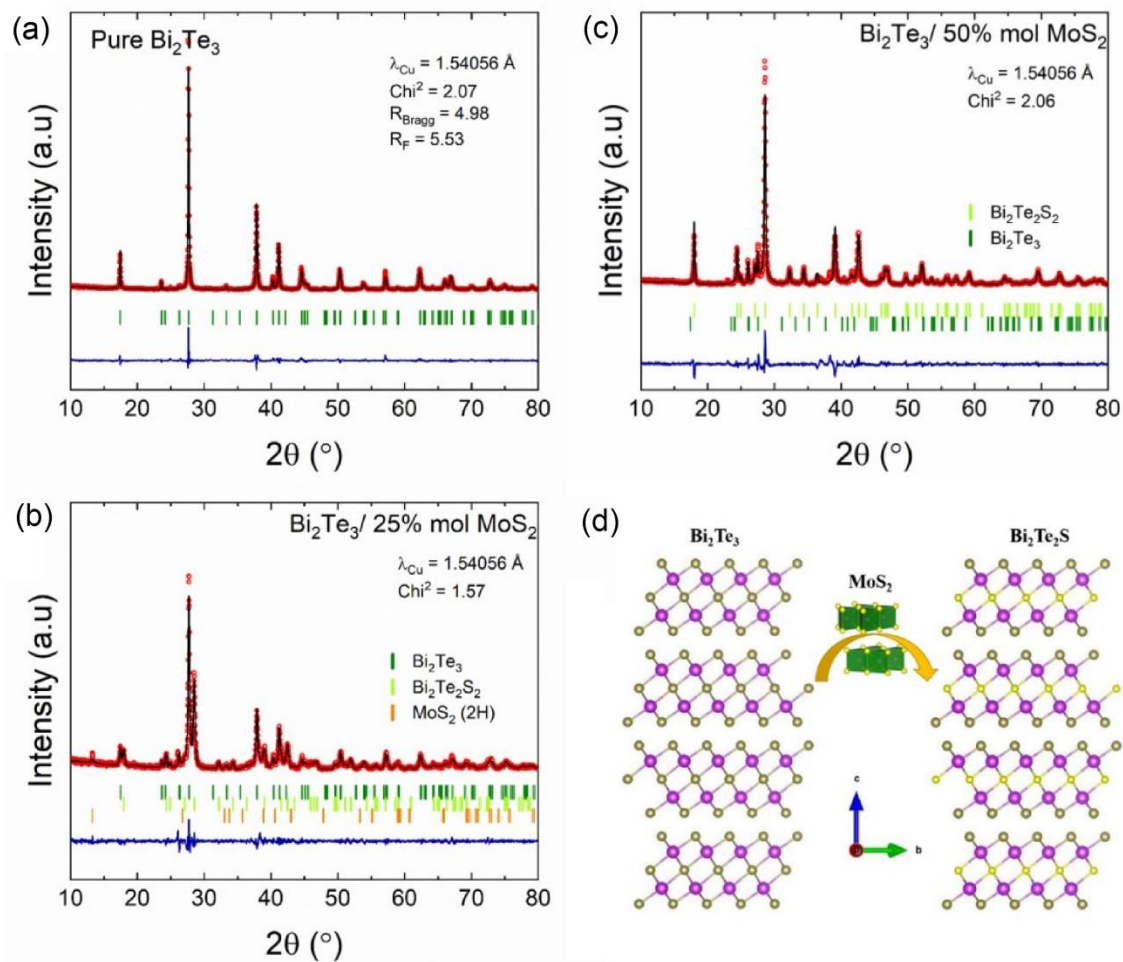


Figure 2.2 Refinement of the PXRD pattern of the $\text{Bi}_2\text{Te}_3/\text{X mol\% MoS}_2$ nanocomposite for a) $X = 0$, b) $X = 25$, c) $X = 50$, and d) Schematic structural representation of the Bi_2Te_3 , $\text{Bi}_2\text{Te}_2\text{S}$, and 2H-MoS_2

Table 2.1 Cell parameters, reliability factors, and atomic coordination obtained from Rietveld refinement of PXRD patterns of the pure Bi₂Te₃

Pure Bi ₂ Te ₃ ; $R\bar{3}m$; $\lambda_{Cu} = 1.54056 \text{ \AA}$; 300 K					
a (Å)	c (Å)	V (Å ³)	Chi ²	R _{Bragg}	R _F
4.3851(1)	30.4791(1)	507.6(1)	2.07	4.98	5.53
Atom	x	y	z	Biso	Occ.
Bi	0	0	0.4005(1)	1.564(80)	1
Te1	0	0	0	0.891(197)	1
Te2	0	0	0.2088(1)	0.589(172)	1

2.3 Results and discussion

The powder X-ray diffraction (PXRD) patterns of the Bi₂Te₃/X mol%MoS₂ (X = 0, 25, 50) nanocomposites after SPS are shown in **Figure 2.1**, and its corresponding phase purity is confirmed through the Rietveld refinement (**Figure 2.2**). **Figure 2.1 - 2.2** combining **Table 2.1** shows that the diffraction peaks of the pristine sample X = 0 are in good agreement with the standard data for Bi₂Te₃ (JCPDS no. 89-2009), which highlight low-reliability factors attesting to the non-degradation of the native powder during the sintering process at the select temperature (T = 623 K). However, despite the low sintering temperature, the presence of MoS₂ nanoflake on the Bi₂Te₃ matrix induces the formation of the Bi₂Te₂S-tetradymite phases as visible in the X = 25 and 50 PXRD patterns (**Figure 2.1**), which, unexpectedly, suggests a reaction/degradation occurred during the sintering process. The tetradymite phase (Bi₂Te₂S) is likely obtained by the reaction of the metastable 1T-MoS₂ nanoparticle with the Bi₂Te₃ main matrix surface, affecting the respective microstructure of the sample as further discussed in the next section with the scanning electron microscopy (SEM) images (**Figure 2.3**). In the native powder (X > 0), the surface of Bi₂Te₃ nanoplatelets is uniformly covered with layers of metallic 1T-MoS₂ (**Figure 2.3(d)**)[14]. It is well known that the chemical reactivity of nanoparticles is enhanced on account of the far larger surface areas than similar masses of larger-scale materials. A combination of the enhanced reactivity and the high energy available during electric-field assisted sintering by SPS makes the surface ionic exchange between MoS₂/Bi₂Te₃ nanoplatelets become propitious leading to the formation of tetradymite phase as well as off-stoichiometric MoS_{2-x} nanoplates and/or Mo₂S₃ phase at the interface[15]. It can be pointed out that there is a possibility of partial Mo doping in Bi₂Te₃ according to a recent theoretical report[16]. Besides, the role of the electric field-assisted sintering in the reactive densification is obvious considering the report of Bi₂Te₃-MoS₂ composite realized by the Hot-Pressing (HP) method, wherein there was no reaction between the two phases [5]. However, further investigations are required to fully understand the mechanism of the reaction. It can be noticed that for the low content of MoS₂ (25 mol%), the Bi₂Te₃ phase remained the main phase according to the intensities of the major peaks (**Figure 2.1**). In contrast, the Bi₂Te₂S dominates the matrix while the native Bi₂Te₃ main

peaks are reduced significantly for the 50 mol% sample. The different phases have been confirmed by the SEM composition analysis using Energy Dispersive Spectroscopy (EDS) (**Figure 2.3(e)** and **Figure 2.4-2.6**) and the results are in line with the PXRD observation.

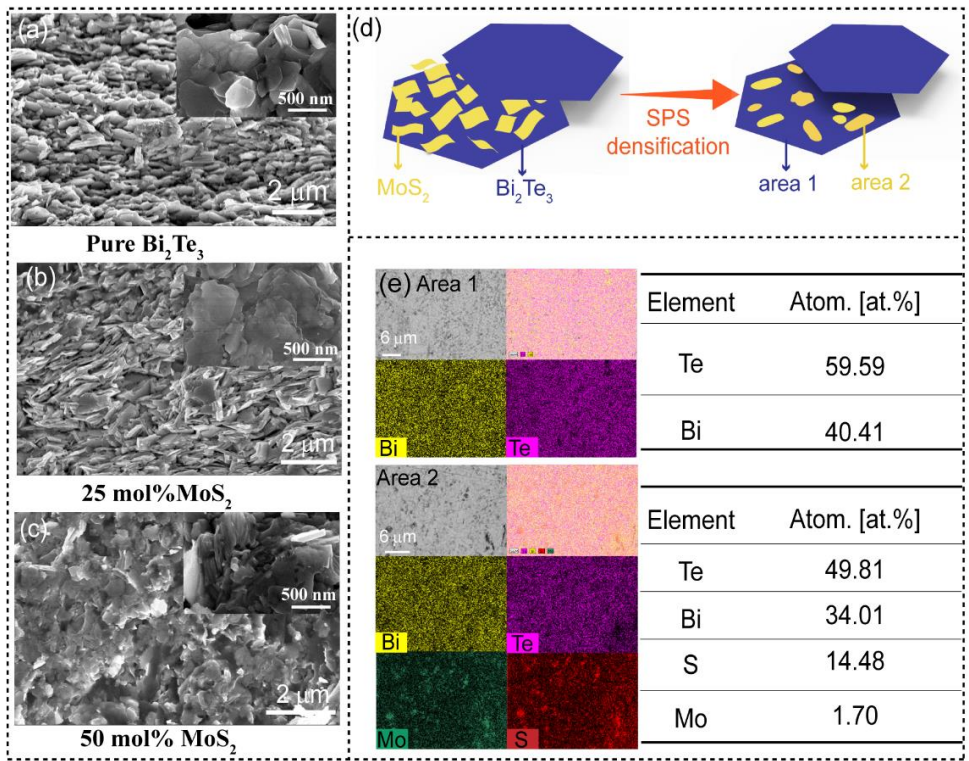


Figure 2.3 Fracture surface SEM images of $\text{Bi}_2\text{Te}_3/\text{X mol\% MoS}_2$ after Spark Plasma Sintering with (a) $\text{X}=0$, (b) $\text{X}=25$, (c) $\text{X}=50$; the insets correspond to the higher magnification images of the fracture surfaces; (d) Schematic depiction of $\text{Bi}_2\text{Te}_3/\text{MoS}_2$ heterostructure before and after SPS; (e) representative elemental mapping of two distinct areas of the $\text{X} = 25$ sample with their corresponding atomic compositions

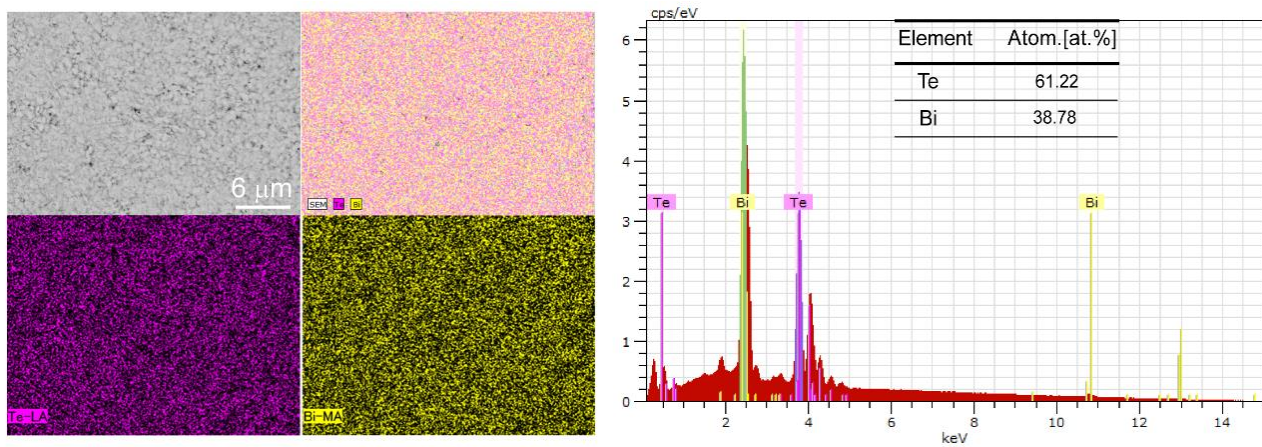


Figure 2.4 The elemental mapping, EDS spectrum and composition of pure Bi_2Te_3 ($\text{x} = 0$) sample

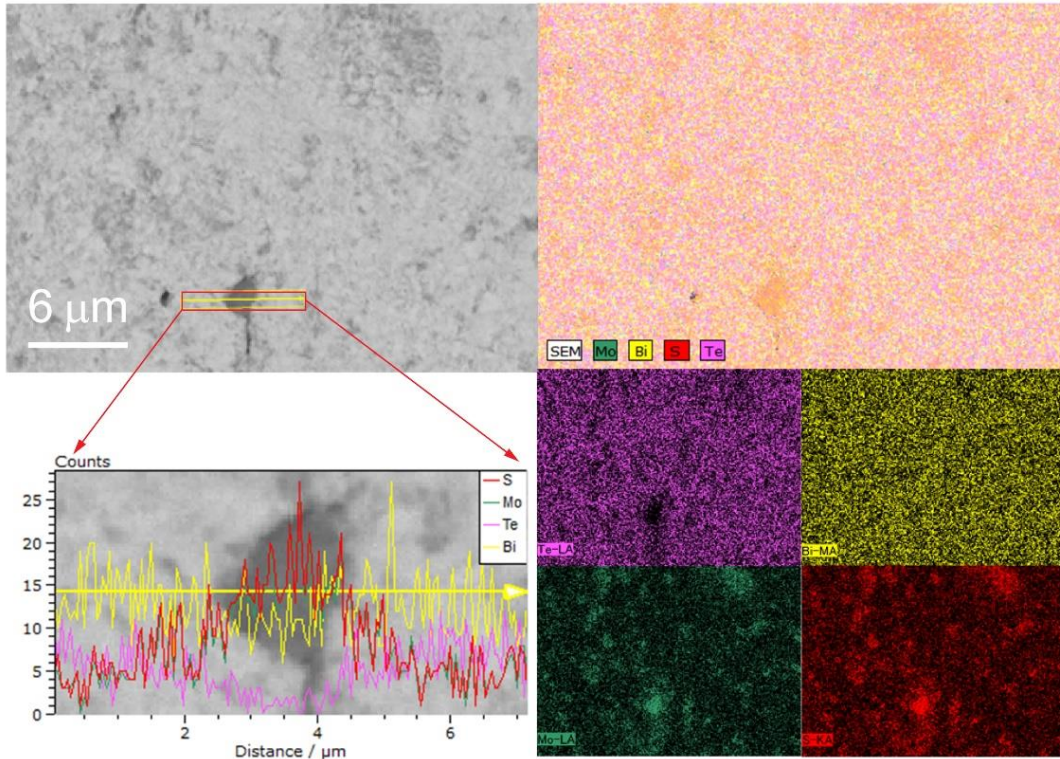


Figure 2.5 Line analysis of the chunk and the elemental mapping of $\text{Bi}_2\text{Te}_3/25 \text{ mol}\% \text{ MoS}_2$ sample

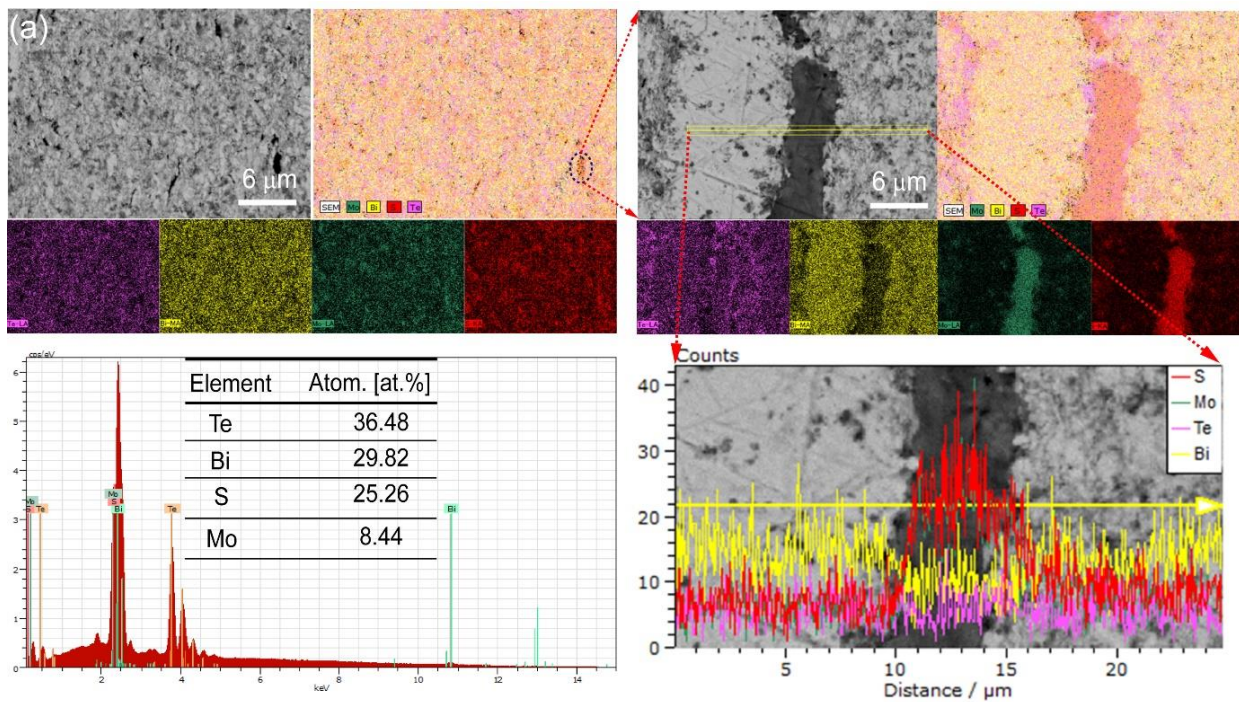


Figure 2.6 (a) The elemental mapping, EDS spectrum and composition of $\text{Bi}_2\text{Te}_3/50 \text{ mol}\% \text{ MoS}_2$ sample as well as the line analysis of black chunk in $\text{Bi}_2\text{Te}_3/50 \text{ mol}\% \text{ MoS}_2$ sample

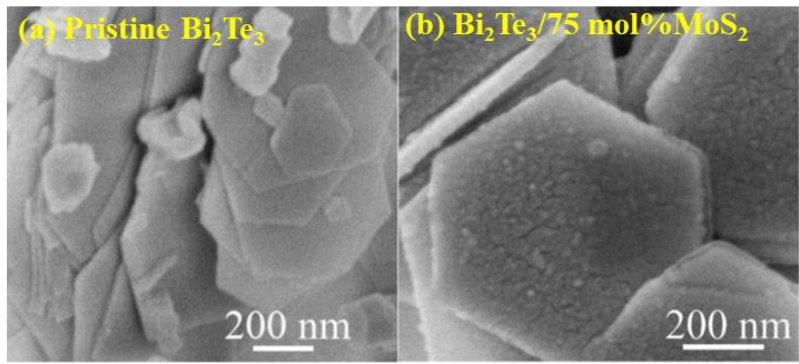


Figure 2.7 SEM images before SPS: (a) pure Bi_2Te_3 nanoplates; (b) $\text{Bi}_2\text{Te}_3/75 \text{ mol\% MoS}_2$

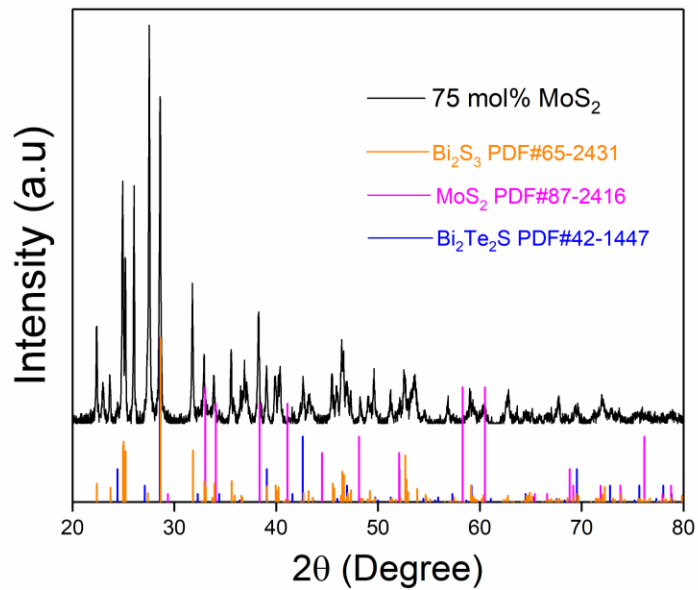


Figure 2.8 PXRD pattern of the $\text{Bi}_2\text{Te}_3/75 \text{ mol\% MoS}_2$ nanocomposite

Figure 2.3(a-c) depicts the SEM images of freshly fractured surfaces of $\text{Bi}_2\text{Te}_3/X \text{ mol\% MoS}_2$ ($X = 0, 25, 50$) samples which show the archetypal plate-shaped particles for the $X = 0$ and 25 samples as expected for these layered nanocomposite materials. The high-magnification image (**Figure 2.3(a), inset**) shows that the pristine Bi_2Te_3 has an obvious typical hexagonal lamellar structure with a smooth surface and a preserved particle size ranging around ~ 500 nm. The shape of the native nanoplates of Bi_2Te_3 in the composite with 25 mol% MoS_2 becomes ill-defined (**Figure 2.3(b), inset**) and the plates do not present the characteristic rough surface indicative of the MoS_2 presence on the surface of the Bi_2Te_3 platelets as seen in the as-synthesized nano-powders (**Figure 2.7(b)**). This is in agreement with the merging/reaction of the MoS_2 and platelets of Bi_2Te_3 to form the $\text{Bi}_2\text{Te}_2\text{S}$ interface as observed through the PXRD analysis (**Figure 2.1**). Notably, the microstructure of the composite with 50 mol% MoS_2 is far different from that of

the 25 mol%. The shape of the crystals became blurry due to the extensive merging of nanoplates promoted by the high content of MoS₂.

The Bi₂Te₃/75 mol% MoS₂ nanocomposite was investigated but the PXRD pattern (**Figure 2.8**) revealed a plethora of secondary phases that are difficult to identify with the conventional PXRD resolution revealing the limit in the MoS₂/Bi₂Te₃ ratio, which can be mixed to be able to control a constructive nanocomposite formation. To further understand the effect of the nanocomposite formation, their electrical and thermal transport properties were characterized and compared.

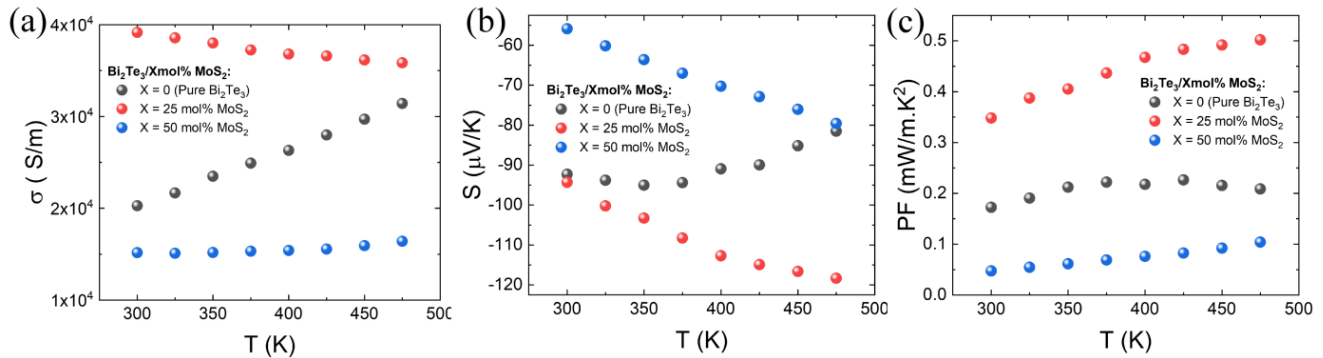


Figure 2.9 Temperature dependence of (a) electrical conductivity, (b) Seebeck coefficient and (c) power factor of the Bi₂Te₃/X mol% MoS₂ (X = 0, 25, 50) nanocomposites.

As displayed in **Figure 2.9**, the sample of Bi₂Te₃ produced using hydrothermal method followed by SPS has a relatively low electrical conductivity caused by the reduction of crystal size, which induced much more scattering interfaces[17]. This will affect significantly the carrier mobility as it has been confirmed through the Hall effect measurement (**Table 2.2**) wherein the carrier mobility of the X = 0 sample is estimated with a low value of $\mu_e = 10.90 \text{ cm}^2 \text{ V}^{-1} \text{ s}^{-1}$. Additionally, it is observed that the Bi₂Te₃/0 mol%MoS₂ is characterized by a non-degenerate *n*-type semiconducting behavior (**Figure 2.9(a)**) that increases with T, positive ($d\sigma/dT$), likely due to a slight Te-rich composition and a moderate carrier concentration in the $\approx 10^{19} \text{ cm}^{-3}$ range (**Table 2.2**) [18]. Compared to the Bi₂Te₃/0 mol%MoS₂ sample, the nanocomposite formation in the Bi₂Te₃/25 mol%MoS₂ sample induces a constructive effect leading to a substantial enhancement of the electrical conductivity, especially in the room temperature range. Our interpretation is that the formation of Bi₂Te₂S between the nanoplates leads to a superior electrical contact by comparison with the Bi₂Te₃ sample wherein the nanoplates are not fully connected (**Figure 2.3(a)-inset and (b)-inset**). Consequently, the carrier mobility is improved, mainly in the out-of-plane axis, and therefore promoting an overall higher electrical conductivity. It is sustained experimentally by the Hall effect measurement, which highlighted a largely improved mobility in the X = 25 sample with a 5 times improved carrier mobility up to $\mu_e = 51.50 \text{ cm}^2 \text{ V}^{-1} \text{ s}^{-1}$ (**Table 2.2**). However, the σ of the nanocomposite sample with 50 mol% MoS₂ is drastically reduced in consistence with the dominant presence of the tetradymite phase (**Figure 2.1**) which reduced the overall carrier

concentration of the nanocomposite. Indeed, the tetradymite phase is known to have a wider bandgap ($E_g \approx 0.3$ eV) and a lower electrical conductivity than Bi_2Te_3 [19,20]. In addition, the influence of the fractured microstructure (**Figure 2.3(c)**) cannot be ruled out, which could be the major contribution of the large reduction of the σ in the $\text{Bi}_2\text{Te}_3/75$ mol% MoS_2 composite by reducing the carrier mobility's.

The Seebeck coefficient (S) behavior has been investigated as an effective indicator of prevalent carrier type as well as the effect of nanocomposite formation on the electrical transport properties. As shown in **Figure 2.9(b)**, all the samples show a negative S indicating that the predominant carriers are the electrons (n -type). The Seebeck coefficient in the $\text{Bi}_2\text{Te}_3/25$ mol% MoS_2 sample is comparable to the pristine sample in the near room temperature range, agreeing with the fact that Bi_2Te_3 is the main phase in $\text{Bi}_2\text{Te}_3/25$ mol% MoS_2 composite. The S values do not saturate over the whole temperature range likely due to the proficient influence of the tetradymite minor phase. The S_{max} ($-118.3 \mu\text{V K}^{-1}$ at 475 K) is about 1.47 times larger than the pristine Bi_2Te_3 ($-81 \mu\text{V K}^{-1}$ at 475 K). This larger $|S|$ is in consistence with the reduced carrier concentration compared to the pristine Bi_2Te_3 sample (**Table 2.2**). Further increase in mol% of MoS_2 dilapidates the value of $|S|$ to around 40% lower in the $\text{Bi}_2\text{Te}_3/50$ mol% MoS_2 sample. Contrary to the electrical transport tendency moving to a ‘semiconductor-like’ behavior with increasing MoS_2 molar ratio, the decreasing of $|S|$ suggests a more ‘metal-like’ behavior not representative of the tetradymite main phase, which will be represented by a higher $|S|$ ($\approx -190 \mu\text{V K}^{-1}$ at 300 K) [20]. However, this Seebeck value appears consistent with the report of the $\text{MoS}_2/\text{Mo}_2\text{S}_3$ nanocomposite[21], which gives us an insight into the non-negligible role of the S-deficient MoS_2 phases observed in the EDS mapping analysis (**Figure 2.5 and 2.6**). However, further investigations with higher accuracy than PXRD and EDS are required to fully confirm the presence of this latter phase and its contribution to the nanocomposites transport properties. Based the things considered above, the 25 mol% MoS_2 content is the optimum value to massively improve the electrical conductivity as well as preserve a large Seebeck coefficient in this typical bulk synthesis approach. Ultimately, the highest power factor ($S^2\sigma$) at room temperature was obtained for the 25 mol% MoS_2 sample with $\text{PF} = 0.35 \mu\text{W m}^{-1}\text{K}^{-2}$ at 300 K that increases to $0.5 \mu\text{W m}^{-1}\text{K}^{-2}$ at 475K, as shown in **Figure 2.9(c)**.

Table 2.2. Carrier concentrations and mobility's of the $\text{Bi}_2\text{Te}_3/\text{X}$ mol MoS_2 nanocomposite samples

Bi ₂ Te ₃ /Xmol MoS ₂ nanocomposite – Hall Effect at 300 K			
	X = 0	X = 25	X = 50
n (cm ⁻³)	8.94x10 ¹⁹	4.75x10 ¹⁹	3.20x10 ¹⁹
μ_e (cm ² .V ⁻¹ .S ⁻¹)	10.90	51.50	29.58

The thermal properties of the nanocomposites were characterized (Fig. 4a and b) to probe the influence of the nanocomposite formation on the thermal transport behavior. The thermal conductivity κ is expressed by $\kappa = \kappa_e + \kappa_l + \kappa_b$. The κ_e can be estimated from the Wiedemann–Franz law:

$$\kappa_e = L \times T \times \sigma, \quad (2.1)$$

where L is the Lorentz number, calculated by the equation:

$$L = 1.5 + \exp[-|S|/116] \quad (2.2)$$

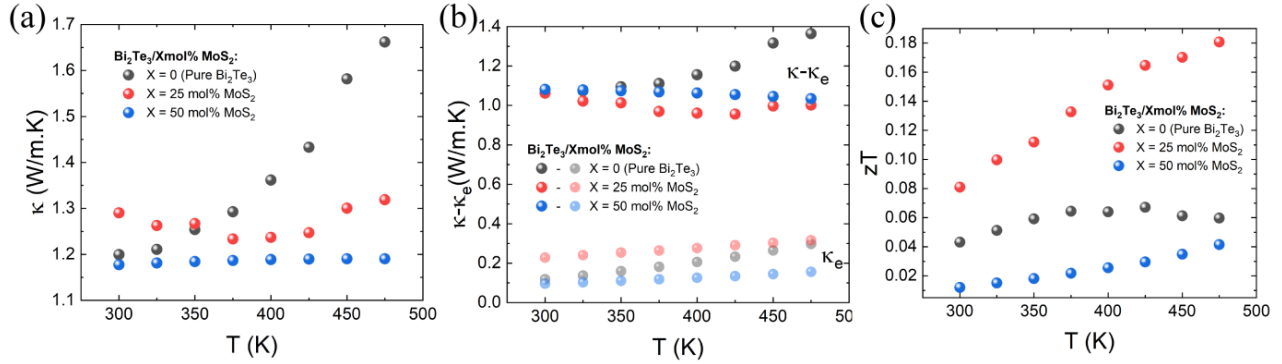


Figure 2.10 Temperature dependence of (a) total thermal conductivity κ ; (b) $\kappa-\kappa_e$; (c) ZT of $\text{Bi}_2\text{Te}_3/\text{X mol\% MoS}_2$

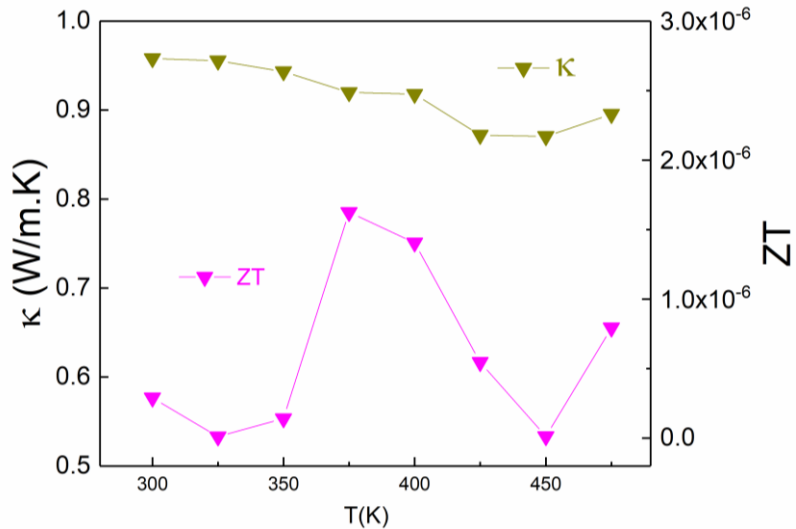


Figure 2.11 Temperature dependence of thermal conductivity κ and figure of merit ZT of the $\text{Bi}_2\text{Te}_3/75\% \text{ mol\% MoS}_2$ nanocomposite

The temperature dependence of κ and $\kappa-\kappa_e$ are shown in **Figure 2.10(a)** and **(b)**. The average thermal conductivities were determined as ~ 1.37 , 1.27 , and $1.19 \text{ W m}^{-1} \text{ K}^{-1}$ for 0 mol%, 25 mol%, and 50 mol% MoS_2 composites, respectively. The bipolar thermal conductivity at high temperatures (sharp upturn on both κ and $\kappa-\kappa_e$) is marked in pristine Bi_2Te_3 and becomes negligible with the formation of the nanocomposite[22]. Interestingly, the decrease of the bipolar contribution in the $\text{Bi}_2\text{Te}_3/\text{MoS}_2$ nanocomposite appears to be a consequence of interface

creation between the Bi_2Te_3 matrix and the tetradymite $\text{Bi}_2\text{Te}_2\text{S}$ formation. The latter can provide an energy barrier, due to the bandgap mismatch, which will preferentially scatter the minor carriers, and consequently suppress the κ_b [23]. Except in the pristine Bi_2Te_3 , it can be seen that the κ_l predominates in the heat transport process and have negative temperature dependence, as revealed in **Figure 2.10(b)**. Moreover, the composite interface seems to play the role of a phonon scattering center, which slightly decreases the κ . Indeed, the $\text{Bi}_2\text{Te}_2\text{S}$ is reported with an intrinsic low thermal transport, thanks to the mixed anion occupancy, which plays a non-negligible role in the enhanced phonon scattering and therefore suppresses the κ_l . This is commonly related to a structural distortion induced by the bonding heterogeneity induced by the mixed anion occupancy in this compound[[24,25]. Therefore, the addition of MoS_2 , and consequently the nanocomposite formation, not only effectively decrease the thermal conductivity but also suppress the bipolar conduction κ_b .

The temperature-dependent ZT values of the nanocomposite samples are plotted in **Figure 2. 10(c)**. It revealed that the $\text{Bi}_2\text{Te}_2\text{S}$ interface formation ($X = 25$) has a beneficial effect to enhance the global ZT of the $\text{Bi}_2\text{Te}_3/\text{MoS}_2$ nanocomposite, mainly due to the significant improvement of the electrical conductivity. However, the constructive effect is limited to a narrow MoS_2 loading. The promotion of the tetradymite as the main phase, and the S-deficient MoS_2 byproduct, rise conflicting transport mechanisms which reduce significantly the ZT values below those of the pristine Bi_2Te_3 for composites with $X = 50$ and 75 (**Figure 2. 10 (c)** and **Figure 2.11**).

2.4 Summary

Novel n-type $\text{Bi}_2\text{Te}_3/X$ mol% MoS_2 nanocomposites were prepared by hydrothermal reaction combined with reactive electric field-assisted sintering. This unconventional approach leads to the formation of additional phases in the nanocomposite samples due to the reaction between Bi_2Te_3 and MoS_2 . The optimum TE properties of the nanocomposites were obtained for the low MoS_2 content of 25 mol% due to the interplanar contact improvement, produced by the tetradymite ($\text{Bi}_2\text{Te}_2\text{S}$) phase formation, which leads to a substantial electrical conductivity improvement without affecting the Seebeck coefficient. As a result, the $\text{Bi}_2\text{Te}_3/25$ mol% MoS_2 gives an enhanced ZT of 0.18 at 475 K, which is 3 times higher than the reference nanostructured Bi_2Te_3 . This atypical approach gives an insight for further enhancement in the TE performance of nanoscale material by using constructive composite interface engineering.

Reference

- [1] M. Hines, J. Lenhardt, M. Lu, L. Jiang, Z. Xiao, J. Vac. Sci. Technol. A 30 (2012) 041509.
- [2] M. Saleemi, M.S. Toprak, S. Li, M. Johnsson, M. Muhammed, J. Mater. Chem. 22 (2012) 725-730.
- [3] H.J. Goldsmid, Materials 7 (2014) 2577-2592.
- [4] B. Poudel, Q. Hao, Y. Ma, Y. Lan, A. Minnich, B. Yu, X. Yan, D. Wang, A. Muto, D. Vashaee, X. Chen, J. Liu, M.S. Dresselhaus, G. Chen, Z. Ren, Science 320 (2008) 634-638.
- [5] G. Tang, K. Cai, J. Cui, J. Yin, S. Shen, Ceram. Int. 42 (2016) 17972-17977.

- [6] M.K. Keshavarz, D. Vasilevskiy, R.A. Masut, S. Turenne, *Mater. Charact.* 95 (2014) 44-49.
- [7] Q. Tang, Z. Zhou, *Prog. Mater Sci.* 58 (2013) 1244-1315.
- [8] H. Babaei, J.M. Khodadadi, S. Sinha, *Appl. Phys. Lett.* 105 (2014) 193901.
- [9] D. Wickramaratne, F. Zahid, R.K. Lake, *J. Chem. Phys.* 140 (2014) 124710.
- [10] H. Huang, Y. Cui, Q. Li, C. Dun, W. Zhou, W. Huang, L. Chen, C.A. Hewitt, D.L. Carroll, *Nano Energy* 26 (2016) 172-179.
- [11] H. Guo, T. Yang, T. Peng, Z. Zhang, arXiv:1212.3394.
- [12] H. Ju, M. Kim, J. Kim, *Chem. Eng. J.* 275 (2015) 102-112.
- [13] H. Ju, J. Kim, *Dalton transactions* 44 (2015) 11755-11762.
- [14] C. Nethravathi, A. Dattatreya Manganahalli, M. Rajamathi, *ACS Appl. Nano Mater.* 2 (2019) 2005-2012.
- [15] M.K. Keshavarz, D. Vasilevskiy, R.A. Masut, S. Turenne, *J. Electron. Mater.* 43 (2014) 2239-2246.
- [16] P. Gangwar, S. Kumar, N. Khare, *Mater. Res. Express.* 6 (2019) 105062.
- [17] K. In Soo, S. Vinod K., J. Deep, W. Joshua D., P. Spencer, C. Kan-Sheng, S. Fengyuan, R.-Z. Francisco, P. Arturo, J.-Y. Miguel, D. Vinayak P., M. Tobin J., H. Mark C., L. Lincoln J., *ACS nano* 8 (2014) 10551-10558.
- [18] J.J. Shen, L.P. Hu, T.J. Zhu, X.B. Zhao, *Appl. Phys. Lett.* 99 (2011) 124102.
- [19] L.D. Zhao, B.P. Zhang, J.F. Li, H.L. Zhang, W.S. Liu, *Solid State Sci.* 10 (2008) 651-658.
- [20] D. Bao, J. Chen, Y. Yu, W. Liu, L. Huang, G. Han, J. Tang, D. Zhou, L. Yang, Z.-G. Chen, *Chem. Eng. J.* 388 (2020) 124295.
- [21] G. Solomon, E. Song, C. Gayner, J.A. Martinez, Y. Amouyal, *ACS Appl. Nano Mater.* 4 (2021) 4419-4431.
- [22] I.T. Witting, T.C. Chasapis, F. Ricci, M. Peters, N.A. Heinz, G. Hautier, G.J. Snyder, *Adv. Electron. Mater.* 5 (2019) 1800904.
- [23] D.C. Grauer, Y.S. Hor, A.J. Williams, R.J. Cava, *Mater. Res. Bull.* 44 (2009) 1926-1929.
- [24] S.-J. Joo, B. Ryu, J.-H. Son, J.E. Lee, B.-K. Min, B.-S. Kim, *J. Alloys Compd.* 783 (2019) 448-454.
- [25] R.L. Fagerquist, R.D. Kirby, *Phys. Rev., B Condens. Matter* 38 (1988) 3973-3985.

Chapter 3 Fabrication and TE Properties of n - Type Chalcopyrite/PEDOT:PSS/Graphene Hybrid Film

3.1 Introduction

With the transition of many electronic devices from traditionally rigid to flexible as well as wearable and implantable, the demand for corresponding power supply especially those with autonomous and long-life is growing[1,2]. Thermoelectric (TE) materials that can stably and directly convert ubiquitous heat or industrial waste heat into electric energy have become a hot topic in recent decades[3-6], and especially now for their applicable potential in flexible TE (FTE) devices that can present conformal interactions with heat sources to maximize heat harvesting[7-9]. The energy conversion efficiency of TE materials is determined by a dimensionless figure of merit ZT ($ZT = S^2\sigma T\kappa^{-1}$), where S is the Seebeck coefficient, σ is the electrical conductivity, T is the working temperature, κ is the thermal conductivity, respectively. The combined parameter of $S^2\sigma$, called power factor (PF), is an indicator of the maximum output power[10]. Until now, the state-of-the-art TE materials with high ZT are mostly inorganic bulk materials[11,12].

Inorganic materials are typically rigid, and the focus of the research on FTE materials has been on conducting polymers (CPs) and CP-based composites[13-18]. Although the PF and ZT of CPs and CP-based composite materials are lower compared to inorganic TE materials, their flexibility and in principle low cost device synthesis processes are the attraction. CPs typically have low thermal conductivity, so the challenge has been to improve the PF [14,16,19]. CP-related are mainly p -type so there has much effort devoted to developing n -type FTE materials[20,21].

One strategy is incorporating inorganic TE materials like Ag_2Se which have some flexibility themselves on various flexible polymer substrates including nylon[22], polyimide[23,24], copy paper[25], and silk[26], etc. Nevertheless, it is observed that the TE properties have an apparently decrease as a result of microcracks caused by the increase of bending times in the film. Incorporating inorganic TE components into conductive polymer matrixes has been another effective strategy, trying to take advantage of the inherently low κ and good flexibility of conductive polymers and the superior charge transport properties of inorganic components[5,8]. So far, PEDOT:PSS has been widely studied as the polymer matrix in FTE composites due to its promising σ of 4380 S/cm at RT, stability in the air, robust mechanical properties and commercialization.[27] Many groups have reported PEDOT:PSS-related FTE films with high-performance and excellent flexibility[28-33]. For example, Goo *et al.*[28] prepared flexible proton-irradiated Bi_2Te_3 /PEDOT: PSS composite films by drop casting method and obtained a maximum PF of $325.3 \mu W m^{-1}K^{-2}$ at RT, which is among the top values of Bi_2Te_3 /PEDOT:PSS composites. More recently, Meng *et al.*[33] prepared a PEDOT:PSS/ Ag_2Te composite film supported by polyethersulfone (PES) membrane with a PF of $143.3 \mu W m^{-1}K^{-2}$ at RT, presenting a good flexibility. While such new classes of relatively high-performance FTE films have emerged, most of them have as main constituents the scarce Te or toxic Se element, and/or expensive Ag element, which are not

conducive to the requirements of low cost, environment-friendliness and low toxicity for industrial application. In this work, instead of aiming for just high performance, we have tried to develop an FTE composite based on abundant, inexpensive and eco-friendly inorganic fillers.

One compelling TE inorganic material is non-toxic chalcopyrite, CuFeS_2 [34-37], which is composed of very cheap and abundant elements in the earth crust, and is a stable material free of any noticeable ionic conduction. Chalcopyrite has been widely studied as a potential *n*-type TE material, with its diamond-like structure contributing to intrinsically low lattice thermal conductivity[38,39], tetrahedrally bonding exhibiting large mobility[40], and magnetism found to contribute to a large power factor at room temperature[34,35,41,42].

Herein, based on the polytetrafluoroethylene (PTFE) membrane, *n*-type flexible thermoelectric composite films consisting of $\text{Cu}_{1-x}\text{Zn}_x\text{FeS}_2$ ($x = 0.01, 0.02, 0.03$), PEDOT:PSS were prepared by drop-casting method combined with cold-pressing. The PEDOT:PSS forms an electrical network and provide flexibility to the composite films while the neighbor $\text{Cu}_{1-x}\text{Zn}_x\text{FeS}_2$ particles are bridged by the PEDOT:PSS to generate *n*-type conductivity of the films. Later we have strategically introduced graphene to optimize the interfacial carrier transports in $\text{Cu}_{1-x}\text{Zn}_x\text{FeS}_2$ /PEDOT:PSS composite. It is found that σ , S and PF of composite films exhibit a spike at a certain chalcopyrite mass fraction. Furthermore, the electrical conductivity and the mechanical flexibility of the composite films is improved with the assistance of graphene. The TE properties of the hybrid films are discussed and a prototype TE device based on the abundant mineral-based hybrid material is further demonstrated.

3.2 Experimental section

3.2.1 Materials

Analytical grade elemental powders of Cu (99.7%), Zn (99.9%), and FeS_2 (99.8%) were purchased from Sigma-Aldrich. PEDOT:PSS solution (Clevious PH 1000, the concentration of PEDOT:PSS is 1.1 wt. %) was obtained from As One. Ethanol ($\text{C}_2\text{H}_5\text{OH}$, 98%) was purchased from Wako chemicals. Dimethyl sulfoxide (DMSO), graphene nanoplatelets (6-8 nm thick \times 15 microns wide), polyethylene terephthalate (PET, 0.013 mm in thickness), glass slides and PTFE membrane (0.025 μm pore size, 25 mm in diameter) were purchased from Sigma Aldrich. All the chemicals were of analytical grade.

3.2.2 Preparation of chalcopyrite powder

Zn doped chalcopyrite were synthesized by the solid-state reaction method. High purity powders of Cu (99.7%), Zn (99.9%), FeS_2 (99.8%) were weighed and mixed in the stoichiometric proportions of $\text{Cu}_{1-x}\text{Zn}_x\text{FeS}_2$ ($x = 0.01, 0.02, 0.03$), specified in each section. The mixture powders were loaded into a quartz tube (diameter of 10 mm) which was sealed until the vacuum pressure was less than 2×10^{-3} mbar. These ampoules were put vertically into a programmable resistance box furnace annealed at 973 K for 72 h. The obtained ingots were ground into rough powder in a glovebox under Ar atmosphere and sealed into the vacuum tube and annealed at 973 K for 72 h again. The final ingots were ball

milled for 2 h by the 8000D Mixer/Mill and the milled powders were sieved to filter out large particles ($> 75 \mu\text{m}$) in a glovebox.

3.2.3 Fabrication of the binary chalcopyrite/PEDOT:PSS and ternary chalcopyrite/PEDOT:PSS/graphene films

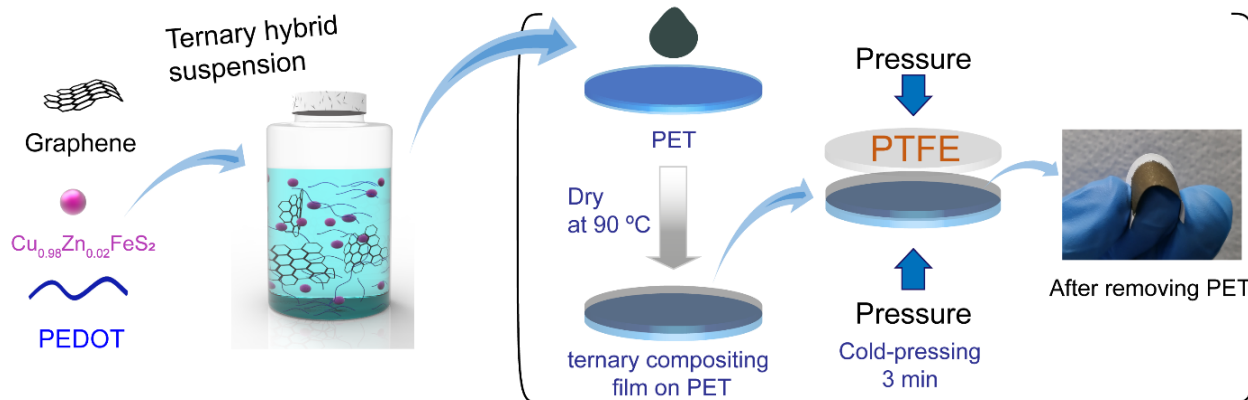


Figure 3.1 Fabrication of the $\text{Cu}_{0.98}\text{Zn}_{0.02}\text{FeS}_2/\text{PEDOT:PSS}/\text{graphene}$ film supported by PTFE membrane and optical photo is the resulted flexible film

The fabrication process is similar to the previous report[25], which was schematically depicted in **Figure 3.1**. For the binary films, in a typical fabrication process, a specific amount (20 mg) of the as-synthesized chalcopyrite powder was well dispersed into a mixture solution constituted by 200 μL PEDOT:PSS, 200 μL ethanol and 100 μL distilled water, which were subjected to a vortex mixer for 5 min, followed by 0.5 h ultrasonication. Aqueous PEDOT:PSS solution was firstly treated with 10 vol.% polar solvent DMSO to improve the electrical conductivity.[43] PET substrates were precleaned by O_2 plasma for increasing the surface hydrophilicity. Then the mixture was drop-cast on the PET substrate which is fixed by a vacuum filter holder. The drop-casting sample was kept in an oven at 90 $^\circ\text{C}$ for 1 h to slowly remove the solvent. Afterwards, the PET based film was sandwiched between 2 pieces of PTFE membrane and pressed at 20 MPa for 3 minutes. After cold-pressing, the composite film was obtained by removing the PET. The same fabrication process was repeated for the films with 30mg, 40mg and 50 mg $\text{Cu}_{1-x}\text{Zn}_x\text{FeS}_2$ ($x = 0.01, 0.02, 0.03$) powder.

For the ternary films, prior to the fabrication process above, chalcopyrite powder and graphene nanosheets were first ball-milled for 2 h to get graphene homogenously dispersed in mixture. Four mass ratios of 20:1, 30:1, 40:1, 50:1 between chalcopyrite and graphene were prepared for the further compositing. Then, the rest procedure to prepare ternary films is same as aforementioned in the binary film fabrication.

3.3 Measurement and characterization

The microstructure and elemental distribution were observed using a field emission scanning electron microscope (FE-SEM, Hitachi S-4800) equipped with an energy dispersive spectrometer (EDS, Horiba EMAX Evolution X-Max 80). The crystallographic structure of the as-prepared composite materials was determined using Cu K α radiation by RINT TTR-3 diffractometer (Rigaku Co., Akishima, Tokyo, Japan). The electrical conductivity and Seebeck coefficient values were obtained simultaneously using a commercial instrument (ZEM-3, Advance Riko). The measurement was carried out in a standard four-probe configuration under a helium atmosphere at RT. Raman spectrums were acquired on a HORIBA-Jobin-Yvon Micro Raman Spectrometer T64000. UV-vis absorption spectra were converted from the diffuse reflectance spectra collected on a UV-vis-NIR Spectrometer V-770 (JASCO). Hall mobility and carrier concentration was measured on ResiTest 8300 Series (Toyo Technica).

3.4 Results and discussion

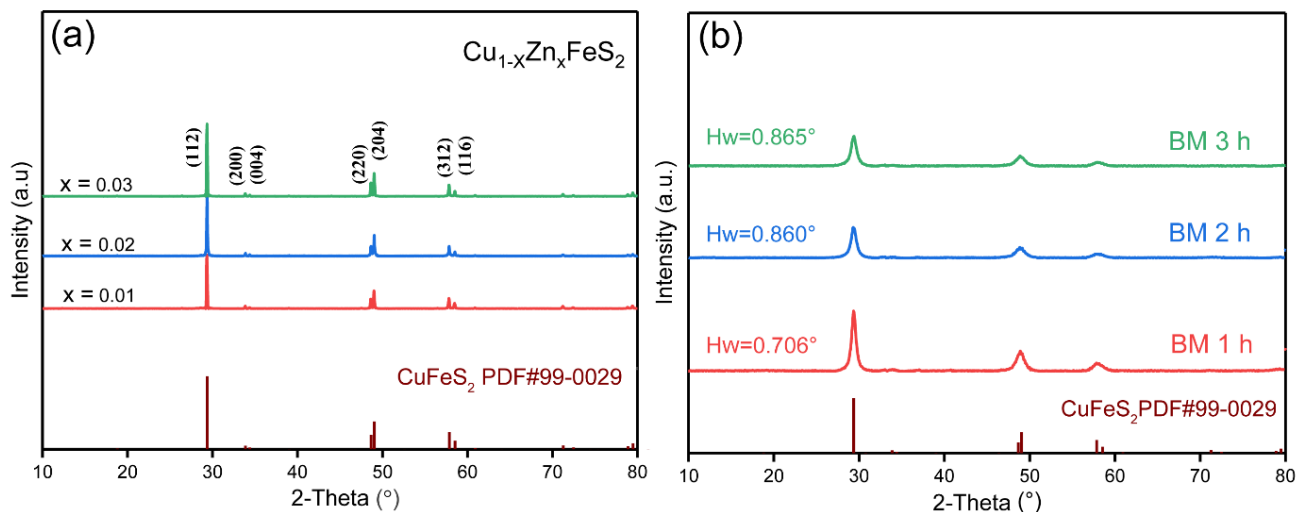


Figure 3.2 XRD patterns of (a) the sintering powder at stoichiometric composition ($\text{Cu}_{1-x}\text{Zn}_x\text{FeS}_2$, $x = 0.01, 0.02, 0.03$); (b) $\text{Cu}_{0.98}\text{Zn}_{0.02}\text{FeS}_2$ powder with different ball milling time.

The synthesized $\text{Cu}_{1-x}\text{Zn}_x\text{FeS}_2$ ($x = 0.01, 0.02, 0.03$) powder were characterized by XRD as seen in **Figure 3.2**. In **Figure 3.2**, all of the patterns display characteristic diffraction peaks of the CuFeS_2 phase (JCPDS 99-0029), which indicates that the prepared nominal $\text{Cu}_{1-x}\text{Zn}_x\text{FeS}_2$ was successfully fabricated by solid state method. There is no peak shift or ZnS peak observed, suggesting that Zn totally substituted Cu under a low partial Zn/Cu substitution level ($x < 0.03$) [44]. **Figure 3.2(b)** presents the XRD of a typical example of $\text{Cu}_{0.98}\text{Zn}_{0.02}\text{FeS}_2$ powder under different ball milling (BM) time, the full widths at half-maximums (FWHMs) were calculated based on the (112) reflections. The FWHMs of the samples ball-milled for 1 h, 2 h and 3 h are 0.706° , 0.860° , and 0.861° , respectively. The crystal domain sizes, τ , of the samples can be roughly estimated using the Scherrer equation, $\tau = K\lambda/\beta\cos\theta$, where $\lambda = 1.5406$

Δ , β corresponds to FWHMs in radians, and $K = 0.9$ was assumed. We thus obtain $\tau = 11.6$ nm, 9.5 nm, and 9.5 nm for the BM1 h, BM 2 h and BM 3 h samples, respectively. Since FWHMs includes a contribution from the diffractometer, the actual crystal domain sizes should be larger than these values. Nevertheless, it is evident that 2 h ball milling is sufficient to reduce particle sizes and the powder with 2 h ball-milled time was chosen as the inorganic fillers.

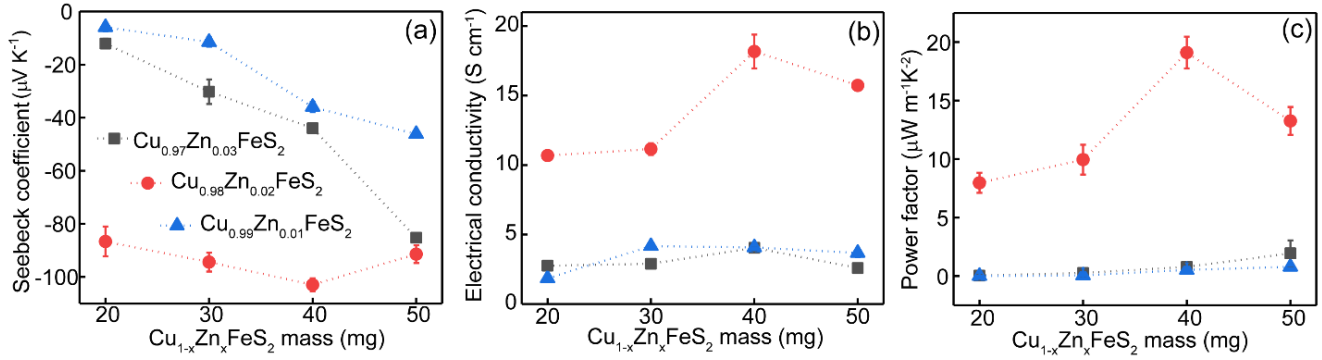


Figure 3.3 (a) Seebeck coefficient (b) Electrical conductivity and (c) Power factor of $\text{Cu}_{1-x}\text{Zn}_x\text{FeS}_2/\text{PEDOT}:\text{PSS}$ binary films as the function of $\text{Cu}_{1-x}\text{Zn}_x\text{FeS}_2$ mass fraction ($x = 0.01, 0.02, 0.03$).

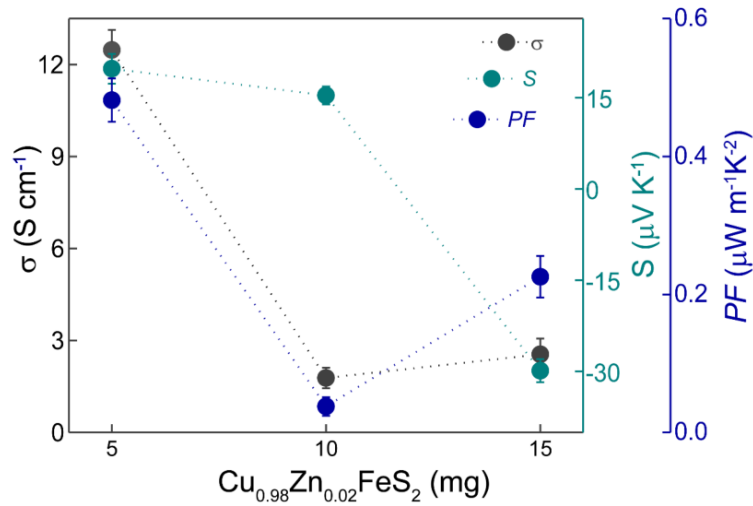


Figure 3.4 TE properties of $\text{Cu}_{0.98}\text{Zn}_{0.02}\text{FeS}_2/\text{PEDOT}:\text{PSS}$ hybrid film as a function of $\text{Cu}_{0.98}\text{Zn}_{0.02}\text{FeS}_2$ mass.

The S , σ , and PF of $\text{Cu}_{1-x}\text{Zn}_x\text{FeS}_2/\text{PEDOT}:\text{PSS}$ ($x = 0.01, 0.02, 0.03$) were compared in **Figure 3.3(a)-(c)**. The negative S indicates that the composite films are n-type. Evidently, the film with $x = 0.02$ exhibits the highest TE properties at the different mass fractions. Hereafter, $\text{Cu}_{0.98}\text{Zn}_{0.02}\text{FeS}_2$ was selected as inorganic filler for all the composite films. The TE properties of the binary films with 5-15 mg $\text{Cu}_{1-x}\text{Zn}_x\text{FeS}_2$ fillers were shown in **Figure 3.4**. As the small amount of filler will introduce the p-type conducting feature into the compositing films, the mass range

of 20-50 mg was chosen for optimizing the best content of inorganic filler for the binary film. According to the semiclassical Mott relation[45], the effective S of the composite film should be compromised when compositing p-type polymers and n-type inorganic materials. However, the $\text{Cu}_{0.98}\text{Zn}_{0.02}\text{FeS}_2/\text{PEDOT:PSS}$ film in this work still behaves competitive S ($-102.5 \mu\text{V/K}$) to the reported one[33,46-53].

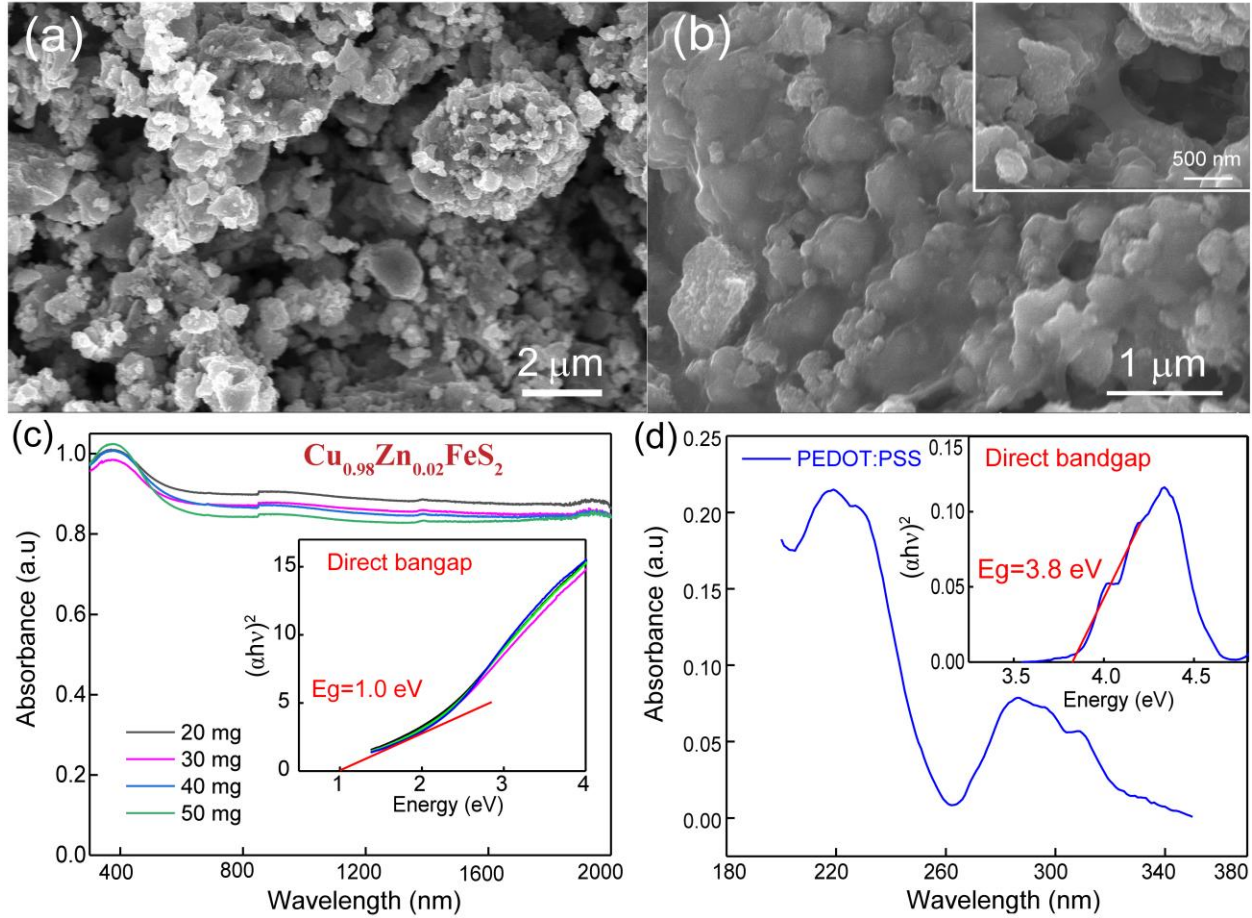


Figure 3.5 SEM image of (a) ball-milled $\text{Cu}_{0.98}\text{Zn}_{0.02}\text{FeS}_2$ powder and (b) binary film with 30 mg $\text{Cu}_{0.98}\text{Zn}_{0.02}\text{FeS}_2$ (inset is the magnified image of binary film); UV-Vis absorption spectra of (c) $\text{Cu}_{0.98}\text{Zn}_{0.02}\text{FeS}_2/\text{PEDOT:PSS}$ (d) PEDOT:PSS (inset: the variation of $(\alpha h\nu)^2$ as a function of photon energy..

Figure 3.5(a) and **(b)** presents the microstructure of $\text{Cu}_{0.98}\text{Zn}_{0.02}\text{FeS}_2$ powder and the composite binary film at 30 mg fraction, respectively. Compared to powder, even though the gap between $\text{Cu}_{0.98}\text{Zn}_{0.02}\text{FeS}_2$ particles were stitched by PEDOT:PSS conductive paths, which facilitating the hopping movement of charge carriers between particles, the pores and bulges observed in **Figure 3.5(b)** negatively affect the effective conductivity of the composite film. On the other hand, according to the UV-vis absorption spectra in **Figure 3.5 (c)** and **(d)**, the bandgap of the $\text{Cu}_{0.98}\text{Zn}_{0.02}\text{FeS}_2$ and PEDOT:PSS is determined to 1.0 eV and 3.8 eV, respectively. Referring to the literature, the work function of $\text{Cu}_{0.98}\text{Zn}_{0.02}\text{FeS}_2$ and PEDOT:PSS is 5.15 eV and 5.2 eV.[54-56] Accordingly, the conduction band (CB) position of

the p-type PEDOT:PSS is estimated to locate at near 1.4 eV regards to vacuum level while the CB of the as-synthesized n-type $\text{Cu}_{0.98}\text{Zn}_{0.02}\text{FeS}_2$ is around 5.1 eV. As a result, the band diagrams of the PEDOT:PSS and $\text{Cu}_{0.98}\text{Zn}_{0.02}\text{FeS}_2$ are depicted in **Figure 3.6(a)**. The energy alignment (P-N junction) in **Figure 3.6(b)** explains the poor electrical conductivity due to the electron-hole pair recombination at the P-N junction, which compromises the carrier concentration and thus suppressing σ . Ultimately, a poor PF of $19.1 \mu\text{W m}^{-1}\text{K}^{-2}$ was obtained from $\text{Cu}_{0.98}\text{Zn}_{0.02}\text{FeS}_2(40 \text{ mg})/\text{PEDOT:PSS}$.

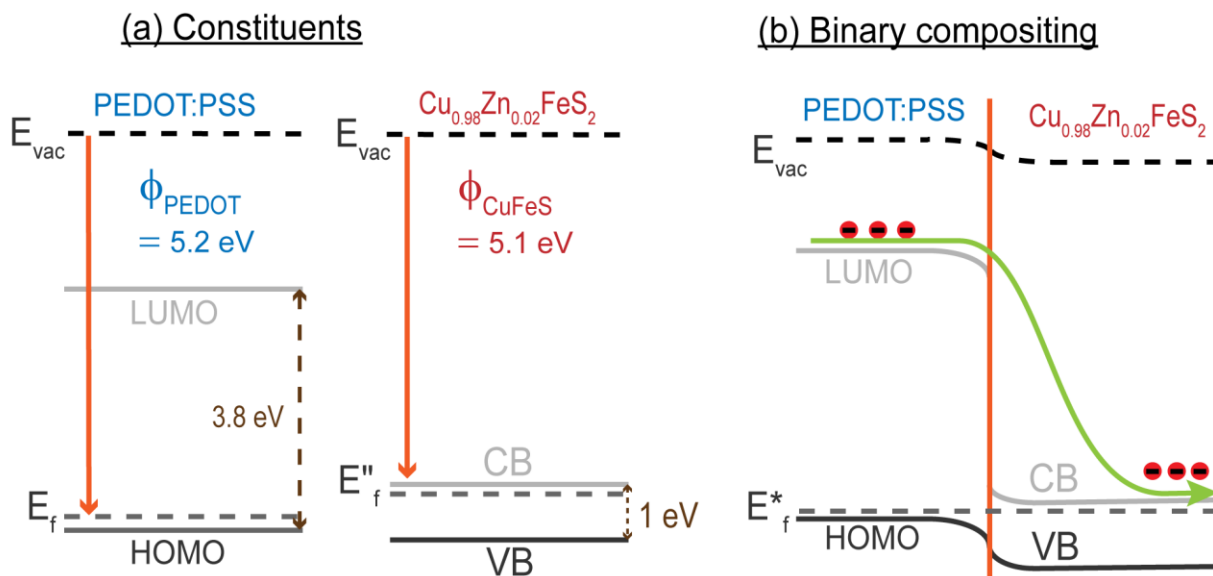


Figure 3.6 (a) Band diagram of the constituents; (b) Band alignment between PEDOT:PSS and $\text{Cu}_{0.98}\text{Zn}_{0.02}\text{FeS}_2$.

Taking into account that the conductivity of inorganic materials will decrease when being reduced in dimensionality and the relatively high interfacial contact resistance when incorporating them into the conductive polymer, many researchers have tried to address it by adding carbon allotropes[8,10,57-63]. The significant enhancement of the PF was observed due to the enhanced conductivity caused by the optimized carrier concentration and/or reduced void volume fraction between inorganic fillers. Among these carbon allotropes, graphene, a one-atom thick sp^2 -bonded planar carbon sheet, has frequently been considered as a promising filler to construct better conducting channels due to its higher theoretical surface area, high electrical conductivity, stable thermal properties, and excellent mechanical and chemical properties. Moreover, it has been reported that the π - π interaction between PEDOT:PSS and graphene ordered the PEDOT:PSS molecular chain arrangement and conversely made graphene dispersing more homogenously in the matrix, leading to an increase in carrier mobility and electrical conductivity[64-66]. Herein, graphene nanosheets were introduced to the binary film.

The XRD patterns of $\text{Cu}_{0.98}\text{Zn}_{0.02}\text{FeS}_2/\text{PEDOT:PSS}/\text{graphene}$ (20-50 mg/200 $\mu\text{L}/1 \text{ mg}$) hybrid films were firstly measured and shown in **Figure 3.7(a)**. Only $\text{Cu}_{0.98}\text{Zn}_{0.02}\text{FeS}_2$ diffraction peaks were discernible, implying the stability of the $\text{Cu}_{0.98}\text{Zn}_{0.02}\text{FeS}_2$ during the solution treatment. The peaks for graphitic structure was not observed due to the

small amount of graphene; there is also no characteristic peak of PEDOT:PSS because of its amorphous crystal structure. To evidence the existence of graphene and its interaction with the matrix, the Raman spectra of binary and ternary films were performed, as shown in **Figure 3.7(b)**. The characteristic peaks of chalcopyrite at around 218.1 cm^{-1} , 285.7 cm^{-1} (A_1 modes), 398.1 cm^{-1} (B_2 modes) and 460.6 cm^{-1} (E modes) were observed in both composite films. In ternary film, excepting the peaks of chalcopyrite, the characteristic D ($\sim 1350\text{ cm}^{-1}$) and G bands ($\sim 1585\text{ cm}^{-1}$) of graphene are observed, which are related to the vibrations of sp^3 -type disordered, activated carbon atoms and the sp^2 -like carbon atoms, respectively.[67] A discernible decreased intensity of Raman peaks at 218.1 cm^{-1} , caused by the surface optical vibration, was observed in the ternary film, indicating the relaxation of the surface strain after the interaction between $\text{Cu}_{0.98}\text{Zn}_{0.02}\text{FeS}_2$ and graphene.[61,62,68] **Figure 3.7(c)** and **(d)** give the SEM-EDX analysis and the corresponding energy dispersive X-ray spectroscopy of the ternary film. The mapping result confirmed that Cu, Zn, Fe, S and C elements are uniformly distributed in the composite film. The EDX of $\text{Cu}_{0.98}\text{Zn}_{0.02}\text{FeS}_2$ and $\text{Cu}_{0.98}\text{Zn}_{0.02}\text{FeS}_2/\text{graphene}$ powder is shown in **Figure 3.8**. The semi-quantification from EDX spectrum indicates that the composition of the ternary film is Cu, Zn, Fe, S and C. The average atomic ratio of Cu: Zn: Fe: S is approximately 23: 1: 27: 49, which is close to the nominal composition of $\text{Cu}_{0.98}\text{Zn}_{0.02}\text{FeS}_2$. The thickness variation of ternary films (20, 30, 40, 50 mg) can be seen in **Figure 3.9**.

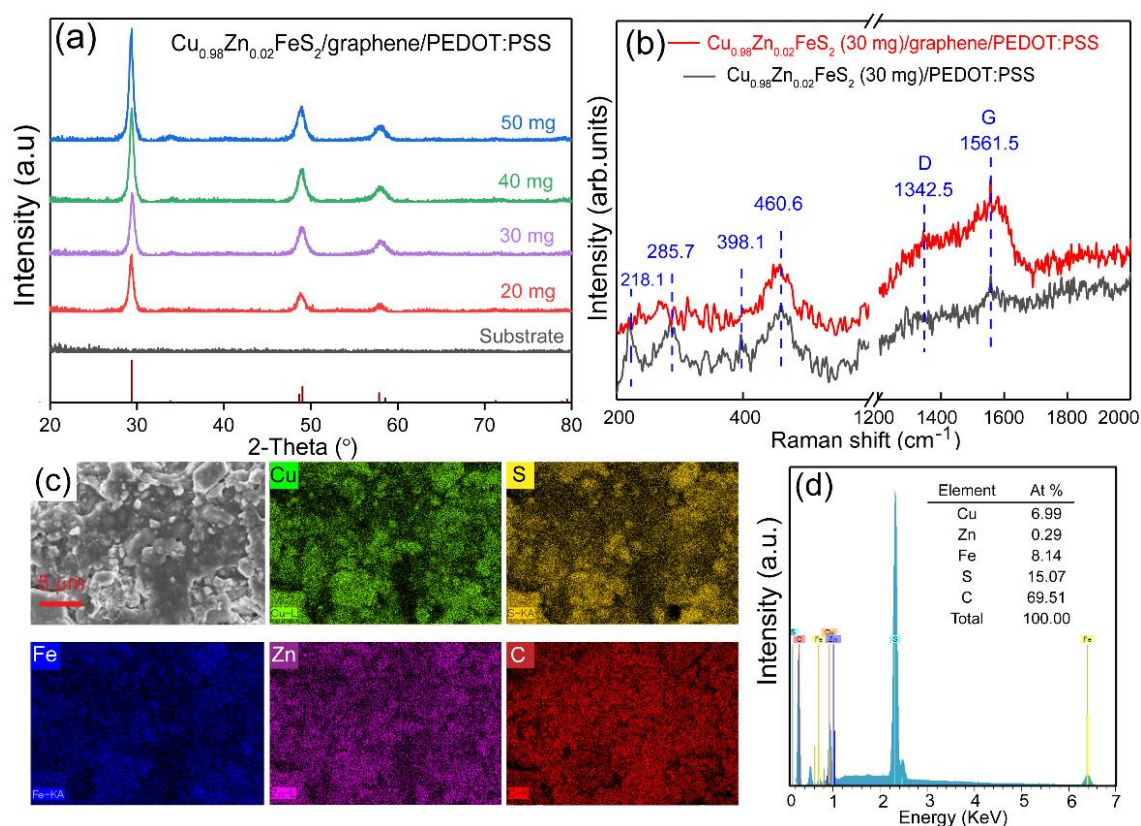


Figure 3.7 Characterization of the ternary films: (a) XRD patterns with different $\text{Cu}_{0.98}\text{Zn}_{0.02}\text{FeS}_2$ mass; (b) Raman spectra of the ternary and binary film at 30 mg fraction; (c) EDX mapping (the scale bar of all the mappings is $5\ \mu\text{m}$) and (d) spectra and composition of the ternary film at 30 mg fraction

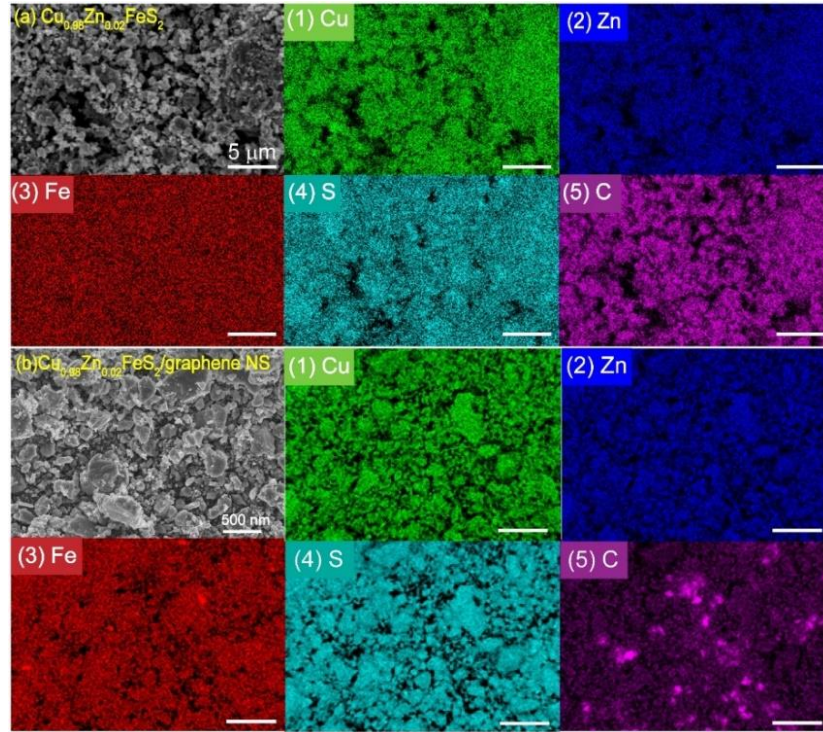


Figure 3.8 SEM observation of ball milling $\text{Cu}_{0.98}\text{Zn}_{0.02}\text{FeS}_2$ and $\text{Cu}_{0.98}\text{Zn}_{0.02}\text{FeS}_2/\text{graphene NS}$, and the corresponding EDX mapping of Cu, Zn, Fe, S, C elements. The difference in C element mappings indicates the distribution of graphene. The scale bar of all the mappings is 5 μm .

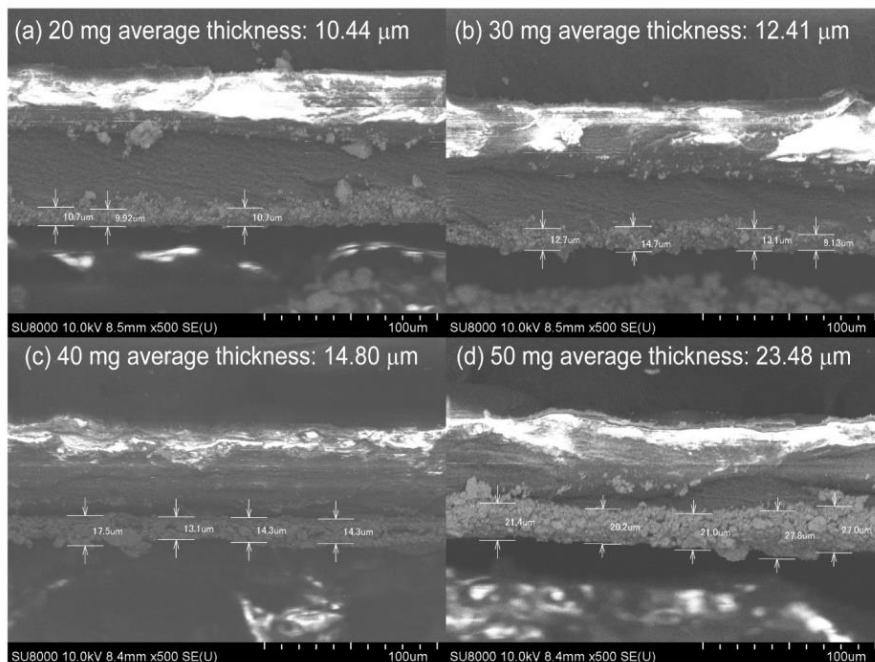


Figure 3.9. SEM cross-section images of $\text{Cu}_{0.98}\text{Zn}_{0.02}\text{FeS}_2$ /graphene/PEDOT:PSS on the PTFE membrane.

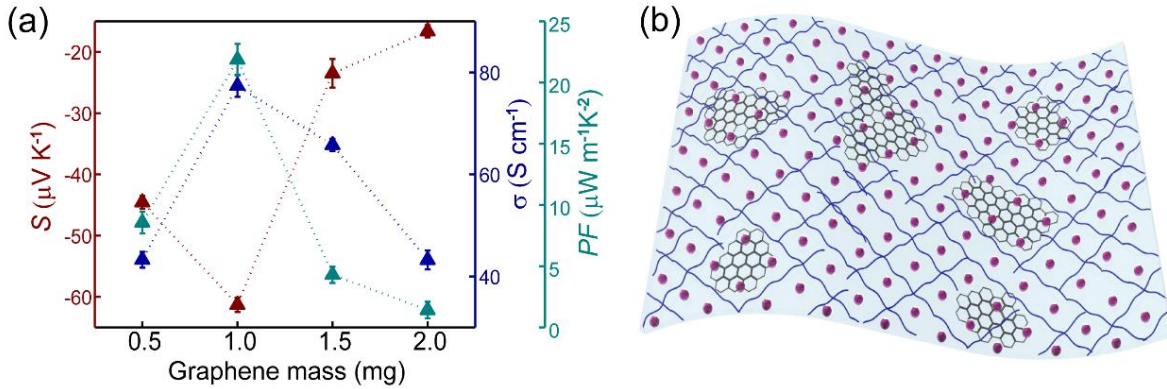


Figure 3.10 (a) Seebeck coefficient, electrical conductivity and Power factor of the $\text{Cu}_{0.98}\text{Zn}_{0.02}\text{FeS}_2$ /PEDOT:PSS/graphene film as a function of graphene mass; (b) Schematic illustration of the $\text{Cu}_{0.98}\text{Zn}_{0.02}\text{FeS}_2$ /PEDOT:PSS/graphene film

As the PEDOT:PSS amount is correlated with the chalcopyrite amount as indicated in the binary films, to optimize the TE properties of ternary films, we mainly optimized the graphene mass and chalcopyrite powder. By compositing the 30 mg $\text{Cu}_{0.98}\text{Zn}_{0.02}\text{FeS}_2$ with PEDOS:PSS and different amount of graphene, the optimal amount of graphene was assessed by TE properties of $\text{Cu}_{0.98}\text{Zn}_{0.02}\text{FeS}_2$ /PEDOT:PSS/graphene (30 mg/200 μL /0.5-2.0 mg) film at RT. As shown in **Figure 3.10(a)**, 1 mg graphene is evaluated as the optimal mass because the maximum σ , S and PF were obtained at this fraction. The electrical conductivity of ternary film at 1 mg (77.3 S cm^{-1}) was ~ 4.3 times higher than the maximum of binary film (18.2 S cm^{-1}), which is ascribed to the intrinsically high conductivity of graphene. In the aspect of S , the negative S values indicate that the introduction of graphene does not alter the type of composite film. Although the S ($-61.3 \mu\text{V K}^{-1}$) obtained with 1 mg graphene is slightly compromised compared to the maximum S in binary film, the higher PF ($23.7 \mu\text{W m}^{-1}\text{K}^{-2}$) was obtained in ternary film with 1 mg graphene.

As graphene mass increased from 0.5 to 1 mg, S and σ behave the similar increasing trend because of the potential barriers existing at the interfaces between $\text{Cu}_{0.98}\text{Zn}_{0.02}\text{FeS}_2$ and graphene. Further increasing the mass fraction of graphene, a rapid decrease trend is observed in electrical conductivity and Seebeck coefficient because the excessive graphene causes agglomeration in the matrix. When graphene nanosheets agglomerated within the matrix, the carrier mobility was destructed by the thicker graphene.[69,70] Meanwhile, the more wrinkles on the surface of graphene nanosheets as the result of agglomeration caused by strong van der Waals forces between graphene layers. Therefore, the π - π conjugation interactions between graphene and polymer could be severely weakened, worsening the electrical transport and reducing Seebeck coefficients at the same time.[71,72] As schematically illustrated in **Figure 3.10(b)**, only appropriate graphene mass is beneficial for building the conductive network in porous film to moderate the pore-related effect and enhance the FTE properties in turn.

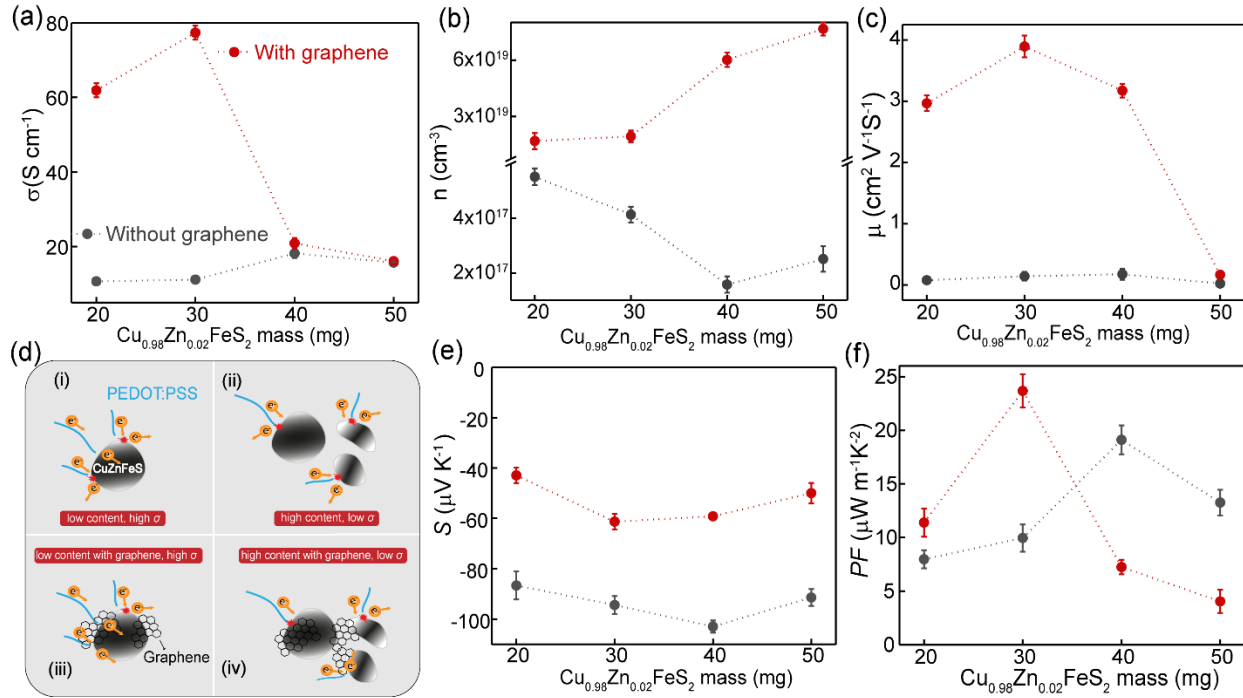


Figure 3.11 TE properties of binary and ternary film as a function of $\text{Cu}_{0.98}\text{Zn}_{0.02}\text{FeS}_2$ mass: (a) Electrical conductivity; (b) Carrier concentration; (c) Carrier mobility; (d) Schematic illustration of the carrier transport mechanism with low content (i, iii) and high content (ii, iv) of $\text{Cu}_{0.98}\text{Zn}_{0.02}\text{FeS}_2$; (e) Seebeck coefficient; (f) Power factor

Subsequently, we optimized the TE properties of ternary films through varying the $\text{Cu}_{0.98}\text{Zn}_{0.02}\text{FeS}_2$ mass. **Figure 3.11(a)** shows electrical conductivity of binary and ternary film as a function of $\text{Cu}_{0.98}\text{Zn}_{0.02}\text{FeS}_2$ mass at 20 mg, 30 mg, 40 mg and 50 mg. When compared to binary film, the addition of highly conductive graphene substantially increased the effective σ of the ternary films especially at 30 mg fraction; as aforementioned, the maximum conductivity of $\sim 77.4 \text{ S cm}^{-1}$ is over 4 times higher than that of the $\text{Cu}_{0.98}\text{Zn}_{0.02}\text{FeS}_2/\text{PEDOT:PSS}$ film (18.2 S cm^{-1}). To understand this phenomenon, the Hall-effect measurement was performed. It should be noted that samples for carrier concentration and mobility were prepared with glass substrates because the flexible films could be easily damaged by the probes of the particular Hall measurement. Accordingly, the rough data of carrier concentration (n) and carrier mobility (μ) of binary and ternary film are respectively shown in **Figure 3.11(b)** and (c). The n and μ of the ternary films are significantly enhanced compared to those of the binary films over the mass fraction range originated from the “metallic” characterise of graphene and the more net paths constructed by it, excepting the μ at 50 mg ascribed to high contact resistance. Further increasing the $\text{Cu}_{0.98}\text{Zn}_{0.02}\text{FeS}_2$ mass, the deteriorated σ was obtained from the as-prepared films due to the relatively high interfacial contact resistance, which leads to the depressed carrier mobility and low σ (as listed in the **Table 3.1**).^[28,73] The carrier transport mechanism is schematically drawn in **Figure 3.11(d)**. For low $\text{Cu}_{0.98}\text{Zn}_{0.02}\text{FeS}_2$ content (**i, iii**, filler mass ≤ 30 mg), there are high path density and relative low porosity, which is converse in high $\text{Cu}_{0.98}\text{Zn}_{0.02}\text{FeS}_2$ content (**ii, iv**, filler mass > 30 mg). Supported by the

PEDOT:PSS paths, the introduced graphene forms supplementary conductive paths at the corresponding mass content (**i** to **iii** and **ii** to **iv**) and thus endowing higher carrier mobility. However, the fully dense paths were broken at high content of $\text{Cu}_{0.98}\text{Zn}_{0.02}\text{FeS}_2$ (**ii** and **iv**), which is responsible for the relatively decreasing trend in conductivity.

Table 3.1 Comparison of the carrier mobility of binary and ternary films when varying $\text{Cu}_{0.98}\text{Zn}_{0.02}\text{FeS}_2$ mass

$\mu/\text{cm}^2 \text{V}^{-1} \text{s}^{-1}$ / Mass fraction film	20 mg	30 mg	40 mg	50 mg
binary	0.07541	0.14086	0.17431	0.02105
ternary	2.96616	3.89533	3.17382	0.16532

Figure 3.11(e) shows the S variation of binary and ternary films as a function of $\text{Cu}_{0.98}\text{Zn}_{0.02}\text{FeS}_2$ mass. The Seebeck coefficients of ternary films decreased a lot compared to binary films because of the enhanced conductivities. However, the degree of the Seebeck coefficient decrease was relatively low compared with the increased magnitude of carrier concentration, which is caused by the energy filtering effect. According to the diagram of the ternary hybrid in **Figure 3.12(b)**, when the graphene was implanted as nanofiller between the $\text{Cu}_{0.98}\text{Zn}_{0.02}\text{FeS}_2$ and PEDOT:PSS, the upward band bending of $\text{Cu}_{0.98}\text{Zn}_{0.02}\text{FeS}_2$ created the energy barriers at the interface between $\text{Cu}_{0.98}\text{Zn}_{0.02}\text{FeS}_2$ and graphene. The band offset was reflected by the flat band potential, which is calculated by the equation

$$\frac{1}{C^2} = \frac{2}{\epsilon_0 \epsilon_r N_D A^2} \left(E - E_{fb} - \frac{k_b T}{e} \right) \quad (3.1)$$

the electrochemical experiments were performed at RT in the three-electrode system with Pt as a counter electrode and 0.5 M Na_2SO_4 (pH = 7) as electrolyte on CHI 660A electrochemical workstation. The *Mott-Schottky* curves were obtained under 2000 Hz with Ag/AgCl as a reference. The intersection point is the $E_{fb} + \kappa_b T/e$ (V vs. Ag/AgCl), where E_{fb} is the flat band potential, which is approximately equaled to conduction band potential (E_{CB}), κ_b is the *Boltzmann constant*, the value is 1.380649×10^{-23} J/K, T is the absolute temperature with a value of 298 K, e is the electronic charge with a value of $1.6021892 \times 10^{-19}$ C, C is the space charge capacitance, ϵ_0 is the vacuum dielectric constant with a value of 8.854×10^{-12} F/m, ϵ_r is the relative dielectric constant of the passivation film at room temperature, N_D is the donor concentration. Taking into account the graphene performs as metal with infinite electrons, the flat band potential of the compositing film is close to the Fermi level (E_f) of graphene, which results in a positive ΔE after band alignment with $\text{Cu}_{0.98}\text{Zn}_{0.02}\text{FeS}_2$, as listed in **Table 3.2**, The vacuum level is calculated by the follow equation,

$$E(\text{eV}) = 4.44 + E(\text{Ag/AgCl}) + 0.197 \quad (3.2)$$

therefore, the energy barrier (ΔE) was caused by the fermi level matching between graphene and chalcopyrite. $E(\text{Ag/AgCl})$ is the electrode potential obtained by the electrochemical experiments in equation 3.1. The E_{fb} of the

ternary film with 30 mg $\text{Cu}_{0.98}\text{Zn}_{0.02}\text{FeS}_2$ is larger than that with 20 mg, indicating a larger ΔE . The larger ΔE the more carriers with low-energy are filtered thus driving the average of carrier energy to a higher degree, leading to a higher Seebeck coefficient. As a result, combination of the maximum electrical conductivity and Seebeck coefficient yields a power factor as high as $23.7 \mu\text{W m}^{-1}\text{K}^{-2}$ for $\text{Cu}_{0.98}\text{Zn}_{0.02}\text{FeS}_2$ (30 mg)/PEDOT:PSS/graphene at RT, as shown in **Figure 3.11(f)**.

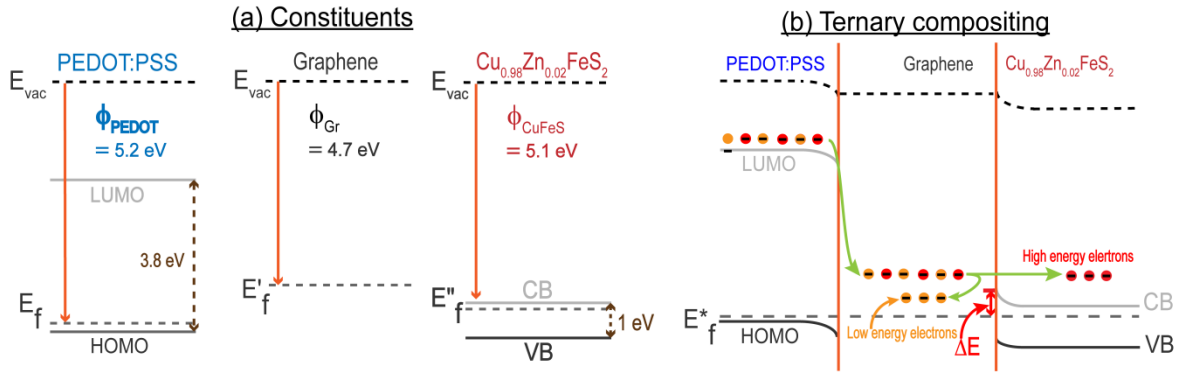


Figure 3.12 Band diagram of the constituents of the compositing film (a); Energy-filtering effects at junctions of PEDOT:PSS/ $\text{Cu}_{0.98}\text{Zn}_{0.02}\text{FeS}_2$, graphene / $\text{Cu}_{0.98}\text{Zn}_{0.02}\text{FeS}_2$ (b).

Table 3.2 The flat band potential of the binary film and vacuum level and energy barriers (ΔE)

	20 mg	30 mg	40 mg	50 mg
E_{fb} (V)	-0.417	-0.437	-0.490	-0.479
E (eV)	4.220	4.200	4.147	4.158
ΔE	0.480	0.500	0.553	0.542

In order to examine the reliability of the $\text{Cu}_{0.98}\text{Zn}_{0.02}\text{FeS}_2$ /PEDOT:PSS/graphene film (30 mg fraction), a bending test was applied around a glass rod with a diameter of 7.13 mm, and the relative rate of σ/σ_0 and S/S_0 (σ_0 and S_0 is the conductivity and Seebeck coefficient before bending) were measured, which is shown in **Figure 3.13(a)** and **(b)**. After 2000 cycles of bending measurement, the electrical conductivity decreased by no more than 25% while the Seebeck coefficient does not have a significant change. Besides, no distinct defects and cracks are observed in ternary film after bending 2000 cycles. These results show the excellent mechanical flexibility of the ternary film compared to the binary film whose descend sharply in the first 200 cycles bending measurement, as shown in **Figure 3.14**. The network matrix from the synergic construction of PEDOT:PSS and graphene nanosheets, can effectively bridge the $\text{Cu}_{0.98}\text{Zn}_{0.02}\text{FeS}_2$ particles meanwhile significantly absorb the outer mechanical stress.

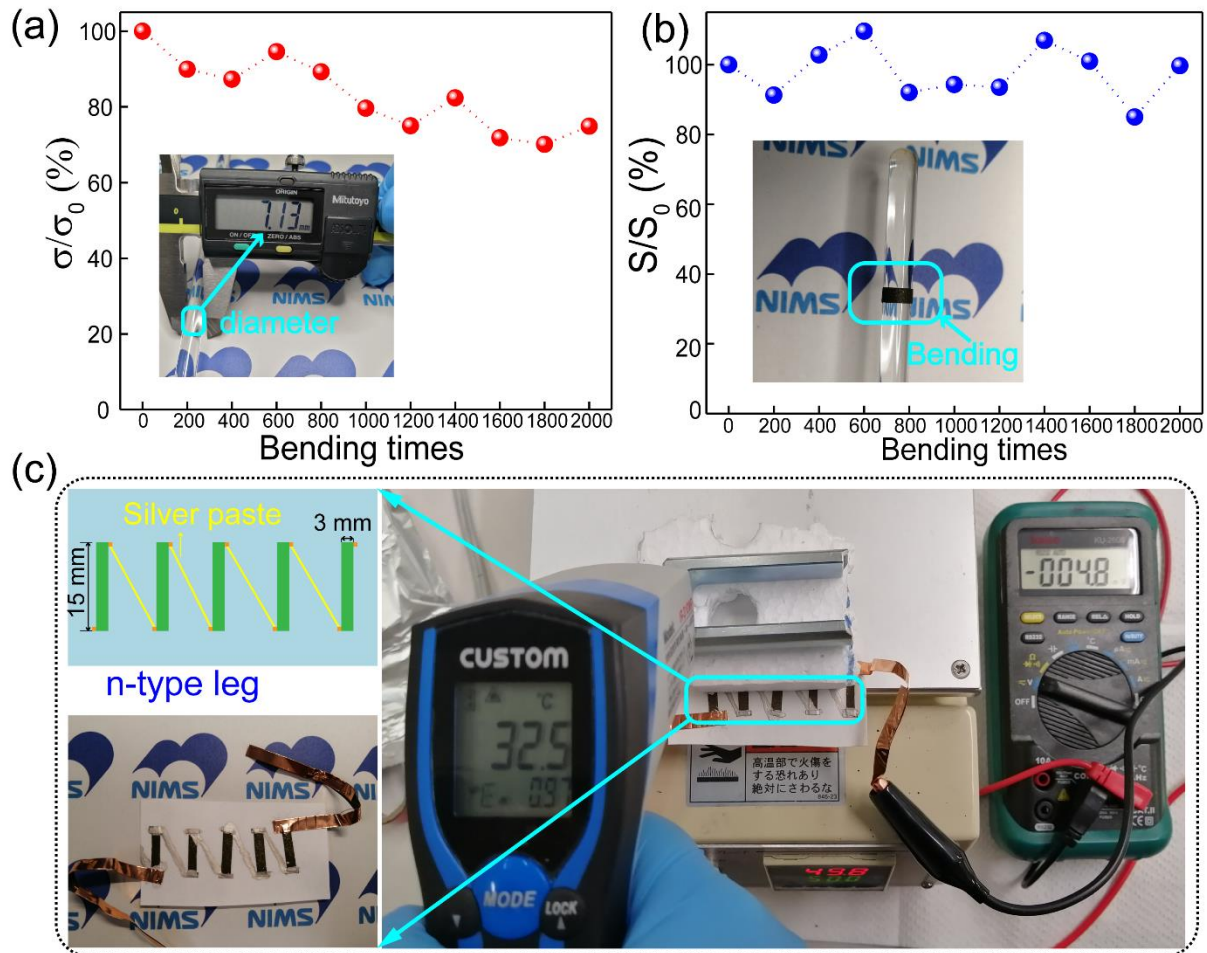


Figure 3.13 The relative rate of (a) electrical conductivity and (b) Seebeck coefficient. The inset in (a) is the photo of a glass rod and in (b) is bending $\text{Cu}_{0.98}\text{Zn}_{0.02}\text{FeS}_2/\text{PEDOT:PSS}/\text{graphene}$ film around the rod; (c) Schematic diagram of a home-made FTE device (left-up), image of the as-fabricated FTE device (left-bottom), and its thermovoltage generation with heating plate (right) as thermal source.

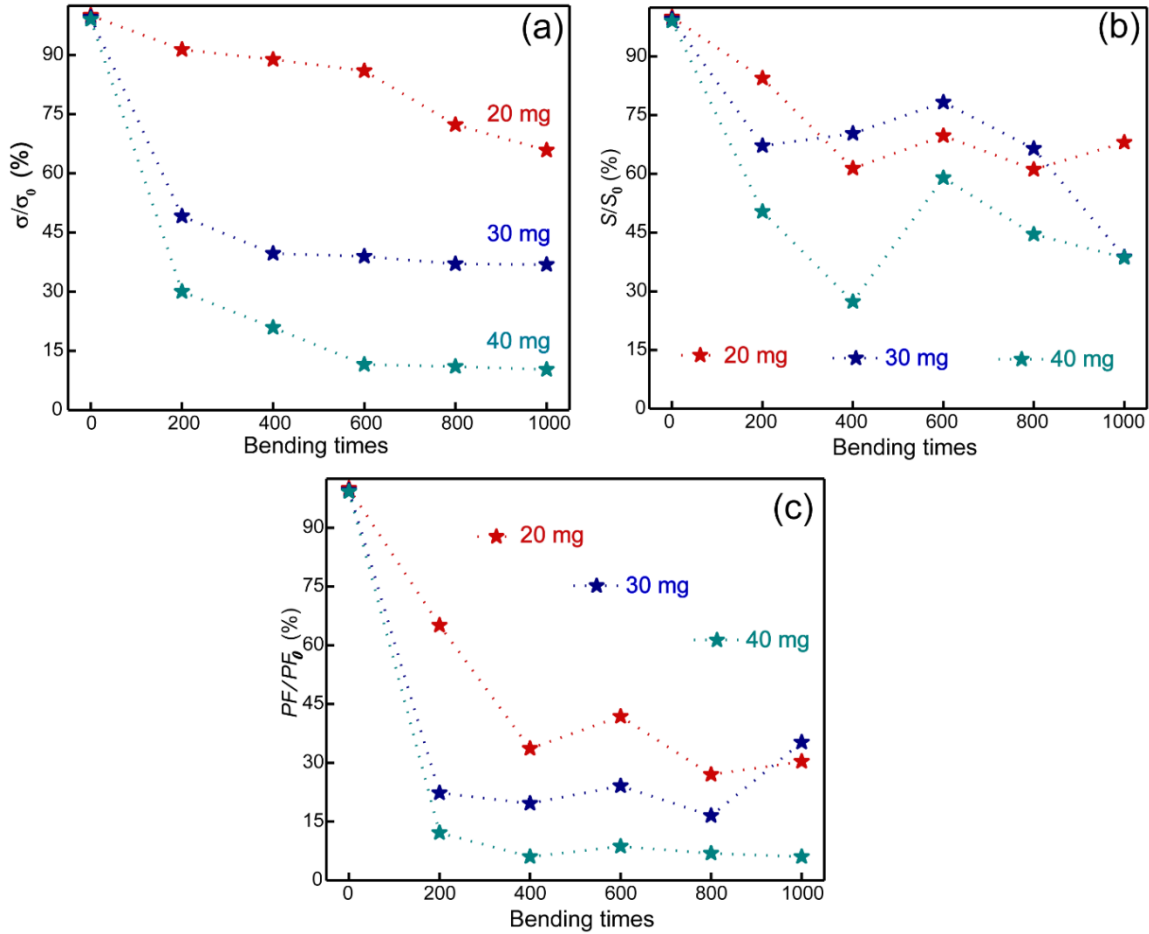


Figure 3.14 The variation of relative rate of (a) σ , (b) S and (c) PF of the $\text{Cu}_{0.98}\text{Zn}_{0.02}\text{FeS}_2$ (20-40 mg)/PEDOT:PSS film.

To make the $\text{Cu}_{0.98}\text{Zn}_{0.02}\text{FeS}_2$ /PEDOT:PSS/graphene film into real applications, a prototype power generator was fabricated based on 5 legs of tailored $\text{Cu}_{0.98}\text{Zn}_{0.02}\text{FeS}_2$ /PEDOT:PSS/graphene film. The length and width of each leg are 15 mm and 3 mm, respectively. Each leg was connected by silver paste and the prototype was supported by a piece of paper. The electrodes of the prototype device were connected by copper foils. To obtain the accurate temperature applied on the device, a temperature meter was used to measure the constant temperature field provided by a temperature controlling apparatus at hot side. The open-circuit voltage (OCV) of the device was measured depending on the temperature differences between heating plate (32.5 °C) and air (26 °C), as shown in **Figure 3. 14(c)** (right). An OCV value of 4.8 mV was read at a ΔT of 6.5 °C, which is compared with the previously reported TE devices, as listed in the **Table 3.3**. The result demonstrates that a flexible TE generator prototype made of $\text{Cu}_{0.98}\text{Zn}_{0.02}\text{FeS}_2$ /PEDOT:PSS/graphene flexible films work well for harvesting the low-grade heat. Although the output voltage of the generator is lower than that of Ag_2Se -based devices, there are room to further enhance the performance after optimizing the material combinations and the device configuration.

Table 3.3 Thermoelectric voltage generation of flexible thermoelectric devices

Year, authors	methods, substrates	Materials		Number	ΔT (K)	OCV (mV)	Leg Size
		<i>n</i>	<i>p</i>				
2020, Mallick et al. [74]	screen-printed, polystyrene	Ag ₂ Se	PEDOT: PSS	13 units	30	71.1	
2020, Lu et al. [58]	vacuum filtration, nylon	Ag ₂ Se/Ag/CuAgSe	Ag paste	6 pieces	18	5.2	5×25 mm ²
2018, Chen et al. [75]	drop-casting, free	Co NWs/PVDF	PEDOT: PSS	10 units	10	6.9	12×3 mm ²
2017, Tian et al. [76]	deposited method, PET	TiS ₂ /organic hybrid superlattice films	PEDOT: PSS	5 pairs	70	33	5×20 mm ²
2016, Oh et al.[77]	vacuum filtration, PTFE	WS ₂	NbSe ₂	16 units	3	2.4	10×5 mm ²
2016, Lu et al. [26]	Repeatedly depositing, silk fabric	Bi ₂ Te ₃	Sb ₂ Te ₃	12	35	10	40×8 0 mm ²
2016, Wan et al. [78]	Solution synthesis, free	TiS ₂ HA _{0.01} NMF _{0.003}		Single- leg	20	1.3	5×5 mm ²
2012, Hewitt et al. [79]	Solution method, fabrics	CNT/PVDF	CNT/PV DF	72 layers	50	26	25-40 μm
This work	Drop-casting, PTFE	Cu _{0.98} Zn _{0.02} FeS ₂ /PE DOT:PSS/graphene	Ag paste	5 pieces	6.5	4.8	3×15 mm ²

3.5 Summary

In summary, we have rationally designed a ternary *n*-type flexible thermoelectric film composed of abundant mineral-based chalcopyrite Cu_{0.98}Zn_{0.02}FeS₂, PEDOT:PSS and graphene nanosheets. The processes to obtain optimized TE properties in such a system was developed. The optimum TE film demonstrates an enhanced electrical conductivity of $\sim 77.4 \text{ S cm}^{-1}$ and a maximum power factor of $\sim 23.7 \mu\text{W m}^{-1}\text{K}^{-2}$. Furthermore, the electrical

conductivity and the Seebeck coefficient of the composite film retained more than 80% of its properties after 2000 bending cycles, proving that the composite film is a promising candidate in the family of *n*-type FTE films. We believe our present work opens up a possibility of nontoxic and low-cost flexible heat-harvesting generators, and the demonstrated successful fabrication will contribute to further rational design in three-component hybrids and boost the research related to such systems.

Reference

- [1] T. Mori, S. Priya, MRS Bull. 43 (2018) 176-180.
- [2] C. Dagdeviren, Z. Li, Z. Wang, Annu.Rev.Biomed.Eng 19 (2017) 85-108.
- [3] J. He, T.M. Tritt, Science 357 (2017) 1369.
- [4] S. Hong, Y. Gu, J.K. Seo, J. Wang, P. Liu, Y.S. Meng, S. Xu, R. Chen, Sci. Adv. 5 (2019) eaaw0536.
- [5] T. Mori, T. Hara, Scr. Mater. 111 (2016) 44-48.
- [6] Z. Liu, N. Sato, W. Gao, K. Yubuta, N. Kawamoto, M. Mitome, K. Kurashima, Y. Owada, K. Nagase, C.-H. Lee, J. Yi, K. Tsuchiya, T. Mori, Joule 5 (2021) 1196-1208.
- [7] I. Petsagkourakisa, K. Tybrandta, X. Crispin, I. Ohkubo, N. Satoh, T. Mori, Sci. Technol. Adv. Mater. 19 (2018) 836-862.
- [8] N. Nandihalli, C.-J. Liu, T. Mori, Nano Energy 78 (2020) 105186.
- [9] M. Bharti, A. Singh, A.K. Debnath, A.K. Chauhan, K.P. Muthe, S.K. Gupta, K. Marumoto, T. Mori, D.K. Aswal, Mater. Today Phys. 16 (2021) 100307.
- [10] Y. Chen, M. He, B. Liu, G.C. Bazan, J. Zhou, Z. Liang, Adv. Mater. 29 (2017) 1604752.
- [11] L.D. Zhao, S.H. Lo, Y. Zhang, H. Sun, G. Tan, C. Uher, C. Wolverton, V.P. Dravid, M.G. Kanatzidis, Nature 508 (2014) 373-377.
- [12] J.R. Sootsman, C. Duck Young, K. Mercouri G., Angew. Chem. Int. Ed. 48 (2009) 8616-8639.
- [13] T. Park, C. Park, B. Kim, H. Shin, E. Kim, Energy Environ. Sci. 6 (2013) 788.
- [14] C.T. Hong, W. Lee, Y.H. Kang, Y. Yoo, J. Ryu, S.Y. Cho, K.-S. Jang, J. Mater. Chem. A 3 (2015) 12314-12319.
- [15] Q. Yao, L. Chen, W. Zhang, S. Liufu, X.C. Chen, ACS nano 4 (2010) 2445-2451.
- [16] D. Kim, Y. Kim, K. Choi, J.C. Grunlan, C. Yu, ACS nano 4 (2010) 513-523.
- [17] D. Park, M. Kim, J. Kim, Polymers 13 (2021) 210.
- [18] F.P. Du, N.N. Cao, Y.F. Zhang, P. Fu, Y.G. Wu, Z.D. Lin, R. Shi, A. Amini, C. Cheng, Sci Rep 8 (2018) 6441.
- [19] Q. Yao, L. Chen, W. Zhang, S. Liufu, X. Chen, ACS nano 4 (2010) 2445-2451.
- [20] S. Hata, K. Taguchi, K. Oshima, Y. Du, Y. Shiraishi, N. Toshima, ChemistrySelect 4 (2019) 6800-6804.
- [21] C. Liu, F. Jiang, M. Huang, B. Lu, R. Yue, J. Xu, J. Electron. Mater. 40 (2010) 948-952.
- [22] C. Jiang, Y. Ding, K. Cai, L. Tong, Y. Lu, W. Zhao, P. Wei, ACS Appl. Mater. Interfaces 12 (2020) 9646-9655.
- [23] J. Choi, K. Cho, J. Yun, Y. Park, S. Yang, S. Kim, Adv. Energy Mater. 7 (2017) 1700972.
- [24] X. Chen, L. Feng, P. Yu, C. Liu, J. Lan, Y.H. Lin, X. Yang, ACS Appl. Mater. Interfaces 13 (2021) 5451-5459.
- [25] J. Gao, L. Miao, C. Liu, X. Wang, Y. Peng, X. Wei, J. Zhou, Y. Chen, R. Hashimoto, T. Asaka, K. Koumoto, J. Mater. Chem. A 5 (2017) 24740-24748.

- [26] Z. Lu, H. Zhang, C. Mao, C.M. Li, *Appl. Energy* 164 (2016) 57-63.
- [27] N. Kim, S. Kee, S.H. Lee, B.H. Lee, Y.H. Kahng, Y.R. Jo, B.J. Kim, K. Lee, *Adv. Mater.* 26 (2014) 2268-2272, 2109.
- [28] G. Goo, G. Anoop, S. Unithrattil, W.S. Kim, H.J. Lee, H.B. Kim, M.H. Jung, J. Park, H.C. Ko, J.Y. Jo, *Adv. Electron. Mater.* 5 (2019) 1800786.
- [29] Y. Lu, Y. Qiu, K. Cai, X. Li, M. Gao, C. Jiang, J. He, *Mater. Today Phys.* 14 (2020) 100223.
- [30] Z. Yan, Y. Zhao, D. Liu, Z. Zhang, Y. Zheng, J. Cui, Y. Zhang, C. Xue, *RSC Adv.* 10 (2020) 43840-43846.
- [31] M.N. Gueye, A. Carella, J. Faure-Vincent, R. Demadrille, J.-P. Simonato, *Prog. Mater. Sci.* 108 (2020) 100616.
- [32] W. Lee, S. Lee, H. Kim, Y. Kim, *Chem. Eng. J.* 415 (2021) 128935.
- [33] Q. Meng, H. Song, Y. Du, Y. Ding, K. Cai, *J. Materiomics* 7 (2021) 302-309.
- [34] N. Tsujii, T. Mori, *Appl. Phys. Express* 6 (2013) 043001.
- [35] R. Ang, U.A. Khan, T. Naohito, K. Takai, N. Ryuhei, T. Mori, *Angew. Chem.* 127 (2015) 13101-13105.
- [36] N. Tsujii, T. Mori, Y. Isoda, *J. Electron. Mater.* 43 (2014) 2371-2375.
- [37] Y. Li, T. Zhang, Y. Quin, D. Tristan, G.J. Snyder, X. Shi, L. Chen, *J. Appl. Phys.* 116 (2014) 203705.
- [38] J. Li, Q. Tan, J.-F. Li, *J. Alloys Compd.* 551 (2013) 143-149.
- [39] D. Berthebaud, O.I. Lebedev, A. Maignan, *J. Materiomics* 1 (2015) 68-74.
- [40] D. Liang, R. Ma, S. Jiao, G. Pang, S. Feng, *Nanoscale* 4 (2012) 6265-6268.
- [41] H. Takaki, K. Kobayashi, M. Shimono, N. Kobayashi, K. Hirose, N. Tsujii, T. Mori, *Appl. Phys. Lett.* 110 (2017) 072107
- [42] H. Takaki, K. Kobayashi, M. Shimono, N. Kobayashi, K. Hirose, N. Tsujii, T. Mori, *Mater. Today Phys.* 3 (2017) 85-92.
- [43] E. Yildirim, G. Wu, X. Yong, T.L. Tan, Q. Zhu, J. Xu, J. Ouyang, J.-S. Wang, S.-W. Yang, *J. Mater. Chem. C* 6 (2018) 5122-5131.
- [44] H. Xie, X. Su, G. Zheng, T. Zhu, K. Yin, Y. Yan, C. Uher, M.G. Kanatzidis, X. Tang, *Adv. Energy Mater.* 7 (2017) 1601299.
- [45] N.W. Ashcroft, N.D. Mermin, In: *Solid State Phys.*, Brooks Cole, Cengage Learning, (1976) 1-848.
- [46] Y. Wang, M. Hong, W.-D. Liu, X.-L. Shi, S.-D. Xu, Q. Sun, H. Gao, S. Lu, J. Zou, Z.-G. Chen, *Chem. Eng. J.* 397 (2020) 125360.
- [47] Y. Lu, Y. Ding, Y. Qiu, K. Cai, Q. Yao, H. Song, L. Tong, J. He, L. Chen, *ACS Appl. Mater. Interfaces* 11 (2019) 12819-12829.
- [48] H. Ju, J. Kim, *ACS nano* 10 (2016) 5730-5739.
- [49] Y. Du, K.F. Cai, S. Chen, P. Cizek, T. Lin, *ACS Appl. Mater. Interfaces* 6 (2014) 5735-5743.
- [50] F. Jiang, J. Xiong, W. Zhou, C. Liu, L. Wang, F. Zhao, H. Liu, J. Xu, *J. Mater. Chem. A* 4 (2016) 5265.
- [51] X. Wang, F. Meng, T. Wang, C. Li, H. Tang, Z. Gao, S. Li, F. Jiang, J. Xu, *J. Alloys Compd.* 734 (2018) 121-129.
- [52] H. Song, C. Liu, H. Zhu, F. Kong, B. Lu, J. Xu, J. Wang, F. Zhao, *J. Electron. Mater.* 42 (2013) 1268-1274.
- [53] G.O. Park, J.W. Roh, J. Kim, K.Y. Lee, B. Jang, K.H. Lee, W. Lee, *Thin Solid Films* 566 (2014) 14-18.
- [54] E. Bastola, K.P. Bhandari, I. Subedi, N.J. Podraza, R.J. Ellingson, *MRS Commun* 8 (2018) 970-978.
- [55] D. Hewidy, A.S. Gadallah, G.A. Fattah, *J. Mol. Struct.* 1130 (2017) 327-332.
- [56] D. Zhang, K. Ryu, X. Liu, E. Polikarpov, J. Ly, M.E. Tompson, C. Zhou, *Nano Lett.* 6 (2006) 9.

- [57] L. Wang, Q. Yao, J. Xiao, K. Zeng, S. Qu, W. Shi, Q. Wang, L. Chen, *Chem. Asian J.* 11 (2016) 1804-1810.
- [58] Y. Lu, Y. Qiu, K. Cai, Y. Ding, M. Wang, C. Jiang, Q. Yao, C. Huang, L. Chen, J. He, *Energy Environ. Sci.* 13 (2020) 1240-1249.
- [59] J. Wei, Y. Wang, X. Li, Z. Jia, S. Qiao, Q. Zhang, J. Du, *Int. J. Energy Res.* 44 (2020) 6885-6893.
- [60] T.-H. Chen, P.-H. Chen, C.-H. Chen, *J. Mater. Chem. A* 6 (2018) 982-990.
- [61] S.H. Jung, K.T. Kim, G.S. Lee, J.Y. Sun, D.W. Kim, Y.S. Eom, D.Y. Yang, J. Yu, J.M. Park, D.Y. Hyeon, K.I. Park, *ACS Appl. Mater. Interfaces* 13 (2021) 5125-5132.
- [62] Y.M. Cho, K.T. Kim, G.S. Lee, S.H. Kim, *Appl. Surf. Sci.* 476 (2019) 533-538.
- [63] J.C. Li, D. Li, W. Xu, X.Y. Qin, Y.Y. Li, J. Zhang, *Appl. Phys. Lett.* 109 (2016) 173902.
- [64] H. Sirringhaus, P.J. Brown, R.H. Friend, M.M. Nielsen, K. Bechgaard, B.M.W. Langeveld-Voss, A.J.H. Siperling, R.A.J. Janssen, E.W. Meijer, P. Herwig, D.M. De Leeuw, *Nature* 401 (1999) 685-688.
- [65] C. Park, D. Yoo, S. Im, S. Kim, W. Cho, J. Ryu, J.H. Kim, *RSC Adv.* 7 (2017) 25237-25243.
- [66] Y. Yao, H. Dong, W. Hu, *Adv. Mater.* 28 (2016) 4513-4523.
- [67] L. Huang, J. Lu, D. Ma, C. Ma, B. Zhang, H. Wang, G. Wang, D.H. Gregory, X. Zhou, G. Han, *J. Mater. Chem. A* 8 (2020) 1394-1402.
- [68] W.H. Shin, K. Ahn, M. Jeong, J.S. Yoon, J.M. Song, S. Lee, W.S. Seo, Y.S. Lim, *J. Alloys Compd.* 718 (2017) 342-348.
- [69] P.R. Jagadish, M. Khalid, L.P. Li, N. Amin, R. Walvekar, A. Chan, *AIP Conf. Proc.* 2137 (2019) 040003.
- [70] T.A. Amollo, G.T. Mola, M.S.K. Kirui, V.O. Nyamori, *Crit. Rev. Solid State Mater. Sci.* 43 (2017) 133-157.
- [71] L. Wang, Q. Yao, H. Bi, F. Huang, Q. Wang, L. Chen, *J. Mater. Chem. A* 2 (2014) 11107.
- [72] X. Li, J. Yin, J. Zhou, Q. Wang, W. Guo, *Appl. Phys. Lett.* 100 (2012) 183108.
- [73] B. Zhang, J. Sun, H.E. Katz, F. Fang, R.L. Opila, *ACS Appl. Mater. Interfaces* 2 (2010) 3170-3178.
- [74] M.M. Mallick, A.G. Rosch, L. Franke, S. Ahmed, A. Gall, H. Gesswein, J. Aghassi, U. Lemmer, *ACS Appl Mater Interfaces* 12 (2020) 19655-19663.
- [75] Y. Chen, M. He, J. Tang, G.C. Bazan, Z. Liang, *Adv. Electron. Mater.* 4 (2018) 1800200.
- [76] R. Tian, C. Wan, Y. Wang, Q. Wei, T. Ishida, A. Yamamoto, A. Tsuruta, W. Shin, S. Li, K. Koumoto, *J. Mater. Chem. A* 5 (2017) 564-570.
- [77] J.Y. Oh, J.H. Lee, S.W. Han, S.S. Chae, E.J. Bae, Y.H. Kang, W.J. Choi, S.Y. Cho, J.-O. Lee, H.K. Baik, T.I. Lee, *Energy Environ. Sci.* 9 (2016) 1696-1705.
- [78] C. Wan, R. Tian, A.B. Azizi, Y. Huang, Q. Wei, R. Sasai, S. Wasusate, T. Ishida, K. Koumoto, *Nano Energy* 30 (2016) 840-845.
- [79] C.A. Hewitt, A.B. Kaiser, S. Roth, M. Craps, R. Czerw, D.L. Carroll, *Nano Lett.* 12 (2012) 1307-1310.

Chapter 4 Fabrication and TE Properties of *p* - Type

Mg_{0.99}Cu_{0.01}Ag_{0.99}Sb_{0.97}/graphene/PEDOT:PSS Hybrid Film

4.1 Introduction

With the advancement in flexible electronic technology, a lot of attention has been paid towards thermal management, which can effectively utilize the low grade waste heat for electrical power generation[1]. Thermoelectric (TE) materials, which are one of the prominent energy harvesting technologies, can directly convert the unutilized heat into electrical energy[2-6]. Recently, the potential application of TE materials in flexible device technology has been increasing for harvesting the waste heat[7-10]. The conversion efficiency of TE device is defined by the material's thermoelectric figure of merit, expressed as $ZT = S^2\sigma T/\kappa_{\text{total}}$, where S , σ , κ_{total} , and T stand for the Seebeck coefficient, the electrical conductivity, the total thermal conductivity, and the absolute temperature, respectively. The maximum output power of TE materials is indicated by a parameter called power factor, $PF = S^2\sigma$, which is usually used to assess the performance of the TE films[8]. In recent decades, advancements in controlling the electron and phonon transport by various novel approaches [11-15] resulted in a substantial improvement in ZT for various inorganic TE materials[16-22] with high conversion efficiencies[23-27].

Despite the high thermoelectric performance of inorganic TE materials, the rigidity limits their potential use in wearable thermoelectric technology[28,29]. Therefore, the research has been focused on the development of flexible TE (FTE) materials and devices[7,9,10]. Mostly, the state-of-art TE materials based on Bi₂Te₃ are explored as high performance FTE devices. For example, Wang *et al.* reported an organic/inorganic hybrid design route, to enhance the ZT of Bi_{0.5}Sb_{1.5}Te₃ by incorporating the copper (II) phthalocyanine (CuPc) from 0.7 to 1.1 in the temperature between 300 K and 523 K[30]. Ao *et al.* reported *n*-type Te-embedded Bi₂Te₃ flexible thin film based on flexible polyimide substrate with an ultrahigh room-temperature PF of 14.65 $\mu\text{W cm}^{-1} \text{K}^{-2}$ [31]. Besides, Norimasa *et al.* overcame the flexible substrate shrink problem during the process of film deposition, and reported a flexible Bi₂Te₃ thin film by sputtering deposition and post-thermal annealing method with improved TE properties[32]. Although Bi-Te alloy-related materials show excellent TE properties, Te is rare, toxic, and expensive which restricts their applicability in the wearable or embeddable devices. Therefore, it is highly essential to develop FTE devices, which constitutes Te free and less toxic elements. Recently, through the novel fabrication technologies and rational structure design, *n*-type Ag₂Se-based films with high thermoelectric properties targeting the commercialization are demonstrated[33-35], which evokes the motivation to improve the performance of the existing TE materials by different optimizing technology.

Since 2012, α -MgAgSb has been paid much attention as a promising *p*-type thermoelectric material for power generation below 550 K[36-38]. α -MgAgSb possesses several advantages such as degenerate semiconducting behavior, intrinsically low lattice thermal conductivity, and good mechanical properties. Zhao *et al.* reported the

pioneer research work on α -MgAgSb with enhanced thermoelectric properties by optimizing the processing technology and acceptor doping[37]. A maximum ZT of ~ 1.4 at 450 K was reported for Ni-doped $\text{MgAg}_{0.97}\text{Sb}_{0.99}$ compounds. Thereafter, extensive research has been focused on tuning the hole carrier concentration by several acceptor doping elements on Mg/Ag site to optimize the electrical and thermal properties of α -MgAgSb[39-52]. Moreover, α -MgAgSb showed not only excellent TE properties but also a maximum conversion efficiency, η_{max} of 8.5% for a single TE leg was demonstrated at a temperature difference (ΔT) of 225 K[38]. Recently, thermoelectric modules fabricated based on n -type $\text{Mg}_3(\text{Sb,Bi})_2$ and p -type α -MgAgSb compounds demonstrated high conversion efficiencies, which are rivaling the Bi_2Te_3 -based compounds.[53-55] For example, a high η_{max} of 7.3% was achieved in $\text{Mg}_3\text{Sb}_2/\text{MgAgSb}$ -based 8-pair module at a ΔT of 315 K[53]. A $\text{Mg}_3(\text{Sb,Bi})_2/\text{MgAgSb}$ -based 2-pair module showed an η_{max} of 6.5% at a ΔT of 250 K[54]. A η_{max} of 2.8% at a ΔT of 95 K was obtained for the $\text{Mg}_{3.2}\text{Bi}_{1.5}\text{Sb}_{0.5}/\text{MgAgSb}$ -based 8-pair module[55]. Till now, despite the high thermoelectric materials and module performances of α -MgAgSb compounds, there are no reports on the development of flexible thermoelectric materials and/or devices.



Figure 4.1 Crack film synthesized by directly hybrid $\text{Mg}_{0.99}\text{Cu}_{0.01}\text{Ag}_{0.97}\text{Sb}_{0.99}$ with PEDOT:PSS supported by PET substrate

Herein, we focused on the development of FTE film based on α -MgAgSb to explore them as a potential candidate for room temperature TE applications. An organic-inorganic strategy[9,30,56,57] and an extended approach reported in our previous study is used in the present work[58]. In this study, we used a chemical composition of $\text{Mg}_{0.99}\text{Cu}_{0.01}\text{Ag}_{0.97}\text{Sb}_{0.99}$ which possesses a broad temperature plateau of ZT above unity as the inorganic matrix[53], and hybrid with poly(3,4-ethylenedioxythiophene):poly(4-styrenesulfonate) (PEDOT:PSS). PEDOT:PSS, among the conductive polymers, is the most promising material due to its advantages of water-dispersibility, good conductivity, low-cost, high transparency, and excellent processability[59]. Over the last decades, the development of PEDOT:PSS open the doors for applications in a wide range of communities spanning from antistatic coatings to energy conversion and energy storage devices[60-64]. Nowadays, the potential applications of PEDOT:PSS based materials are still

explored and studied in new domains such as flexible TE materials[59], thin film transparent heaters[65] or bioelectronics[66,67], etc. In this study, PEDOT:PSS is anticipated to form a conductive network in the MCAS matrix to bridge the neighboring particles by forming the conductive paths as well as enhance the flexibility of the TE film because of its beneficial characteristics, especially its p-type TE properties, intrinsic high mechanical flexibility, and excellent thermal stability[68-71]. However, it is found that there is a new challenge of cracking (see **Figure 4.1**) in the $\text{Mg}_{0.99}\text{Cu}_{0.01}\text{Ag}_{0.97}\text{Sb}_{0.99}$ /PEDOT:PSS hybrid system including the high interfacial resistance that has to be addressed to enhance σ , therefore PF ($S^2\sigma$). Accordingly, Zhang *et al.* optimized interfacial carrier transport by removing the potential oxidation layer on the surface of Bi_2Te_3 [72]. Wang *et al.* coated the highly conductive CuTe layer on the $\text{Bi}_{0.5}\text{Sb}_{1.5}\text{Te}_3$, reaching a promising σ of $\sim 2300 \text{ S cm}^{-1}$ [73]. Also, in our previous work[58], the graphene was added into the hybrid system of $\text{Cu}_{0.98}\text{Zn}_{0.02}\text{FeS}_2$ /PEDOT:PSS leading to a simultaneous enhancement of electrical conductivity and flexibility of resultant films. Specifically, graphene, with a single atomic layer of covalently bonded carbon atoms in a honeycomb lattice[74], exhibits high mechanical strength[75] and electrical transport[76], which is a zero-bandgap semi-metal meaning that the charge carriers move with an exceptionally high mobility[77]. Therefore, graphene is a promising candidate to bridge the interface between organic and inorganic materials for optimizing the carrier transport in the hybrid system.

Accordingly, we developed a facile method to resolve the cracking issue when hybrid MgAgSb-based compound with PEDOT:PSS. For enhancing the σ thus PF , graphene was strategically hybridized to optimize the carrier transport as well as improve the flexibility of the hybrid films. Moreover, to optimize the flexibility, the σ , S , and PF of hybrid films were systematically studied as a function of mass fraction of inorganic material.

4.2 Experimental method

4.2.1 Materials

High purity elements of Mg turnings (99.95%, Sigma Aldrich), Cu beads (99.9995%, Sigma Aldrich), Ag shots ($\geq 99.99\%$, Sigma Aldrich) and Sb chunks (99.9999%, 5N plus) were used for the preparation of $\text{Mg}_{0.99}\text{Cu}_{0.01}\text{Ag}_{0.97}\text{Sb}_{0.99}$. PEDOT:PSS solution (Heraeus Clevios TM PEDOT:PSS PH1000, 1.0–1.3 wt % in water) was obtained from As One. Ethanol ($\text{C}_2\text{H}_5\text{OH}$, 98%) was purchased from Wako chemicals. Graphene nanoplatelets (6–8 nm thick $\times 15 \mu\text{m}$ wide), polyethylene terephthalate (PET, 0.013 mm in thickness), and polytetrafluoroethylene (PTFE) membrane (0.025 μm pore size, 25 mm in diameter) were purchased from Sigma Aldrich.

4.2.2 Synthesis of $\text{Mg}_{0.99}\text{Cu}_{0.01}\text{Ag}_{0.97}\text{Sb}_{0.99}$ (MCAS) powder

The synthesis process of $\text{Mg}_{0.99}\text{Cu}_{0.01}\text{Ag}_{0.97}\text{Sb}_{0.99}$ was followed from our previous report [37, 53]. In briefly, high-purity raw elements were directly weighed according to the nominal composition $\text{Mg}_{0.99}\text{Cu}_{0.01}\text{Ag}_{0.97}\text{Sb}_{0.99}$, subsequently carried out by the two-step high energy ball milling method: firstly, Mg, Ag, and Cu according to the

designed ratio were loaded into a stainless steel jar in an argon-filled glove box, followed by ball milling for 10 hours; next, Sb chunks were added to the ball milled mixture then ball milled for another 8 hours; finally, the resultant powder was sintered using spark plasma sintering (SPS, SPS-1080 System, SPS SYNTEX INC) at 583 K for 10 minutes to get the high-density disks. After checking the properties, the disks were loaded in the stainless-steel ball milling jar in the glovebox, and subjected to a high-energy mill (8000D Mixer/Mill in which the grinding vial is horizontal shaken vigorously under 1060 cycles per minute (cpm) @ 60 Hz, 115 V) with a ball (diameter of 12.7 mm)-to-powder ratio of 32:3 for 5 minutes to obtain the fine powder.

4.2.3 Synthesis of $Mg_{0.99}Cu_{0.01}Ag_{0.97}Sb_{0.99}$ /graphene/PEDOT:PSS films

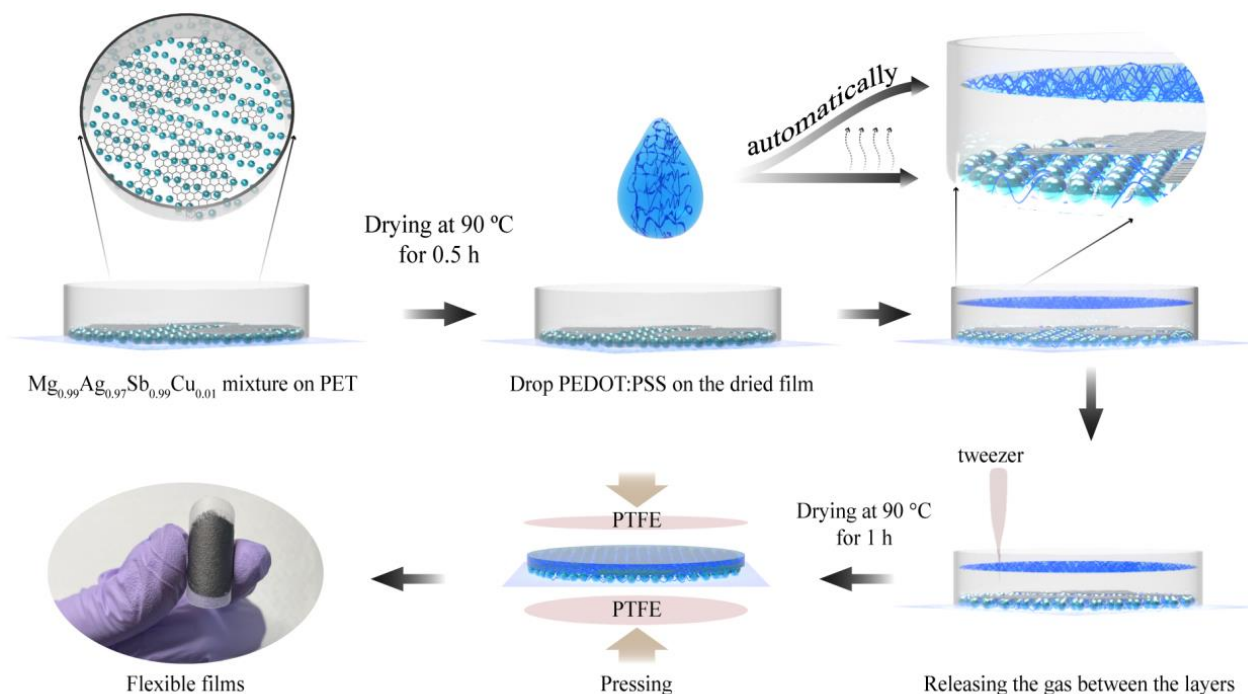


Figure 4.2 Schematic illustration of the process to synthesize the flexible hybrid film supported by PTFE membrane

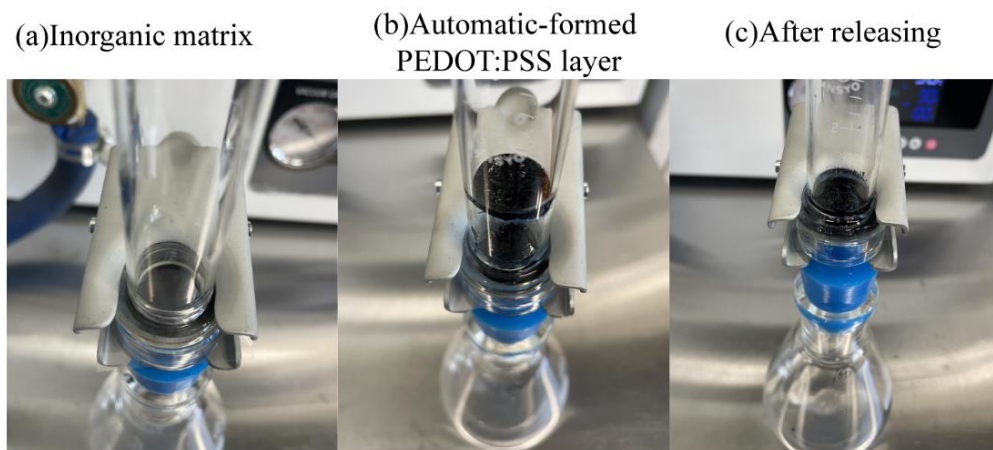


Figure 4.3 The optical photo of the fabrication process of the hybrid film

Considering that the agglomeration of graphene during the process that can limit its functionality in improving the TE properties of hybrids [78,79], herein, initially the graphene was first ball milled with MCAS powder to get good dispersion meanwhile wrap the particles. The MCAS/x graphene powder ($x = 10, 20, 30, 40, 50$ wt%) was loaded and sealed in a ball milling jar under argon atmosphere ($O_2 < 0.1$ ppm) with a ball-to-powder ratio of 32:3 and milled for 0.5 h. The resultant mixture was hybrid with PEDOT:PSS by a strategic process to overcome the crack, as depicted in **Figure 4.2**. For one Specific sample, 200 mg mixed powder was dispersed into 800 μ L ethanol, subjected to a vortex mixer (60Hz) for 5 min, followed by 0.5 h ultrasonication (35kHz, 290W) at room temperature to reduce the aggregation of graphene [80]. Then, the mixture was drop-casting on the PET substrate, which is pre-cleaned by O_2 plasma and fixed by a glass holder, dried at 90 °C for 0.5 hours to form the inorganic matrix (see the matrix after drying in **Figure 4.3a**). Later, 500 μ L PEDOT:PSS was drop-casting on the matrix, which was divided into two parts: the first part automatically formed a PEDOT:PSS layer going up along the glass holder (as the optical photo shown in **Figure 4.3b**) in the meantime the other part was filling into the matrix. Releasing the gas between layers by tweezer, the formed PEDOT:PSS layer was fall down (**Figure 4.3c**). After drying at 90 °C for 1 h, the PET-based film was sandwiched between 2 pieces of PTFE membrane and pressed under 40 MPa at 100 °C for 10 minutes. Under this pressing, the hybrid bottom-layer was further embedded into the flexible PEDOT:PSS layer meanwhile the hybrid film was transferred into the PTFE substrate. Afterwards, the final film was obtained by removing the PET substrate. The same fabrication process was repeated for all the films in this experiment.

4.3 Measurement and characterization

The microstructure and elemental distribution were characterized using Hitachi High-Technologies/Bruker (FE-SEM, SU8000+EDS). The crystallographic structure of the as-prepared materials was determined using a simple powder X-ray diffractometer (Rigaku Co., Ltd.). The sizes distribution of the MCAS particle was obtained by the scanning electron microscopy (SEM) image analyzed by the Nano Measurer software. The electrical conductivity and Seebeck coefficient values were obtained simultaneously using a commercial instrument (ZEM-3, Advance Riko). The measurement was carried out in a standard four-probe configuration under a helium atmosphere. Hall measurement was measured on ResiTest 8300 Series (Toyo Technica). Raman spectroscopy of hybrid powders was obtained from the Reninshaw, miro Raman model in Via Reflex at room temperature with 514 nm laser excitation. X-ray photoelectron spectroscopy (XPS; SigmaProbe, Thermo Fisher Scientific) was done to identify the composition and the chemical state of surface elements. Spectra were recorded in a spectrometer using a monochromatic Al K-alpha X-ray source (beam energy 1486.6 eV) and hemispherical electron energy analyzer. Pass energy of 150 eV and 50 eV for survey and core level spectra, respectively, were used. The error bar of TE properties was obtained by repeating 5 times measurements of samples.

4.4 Results and discussion

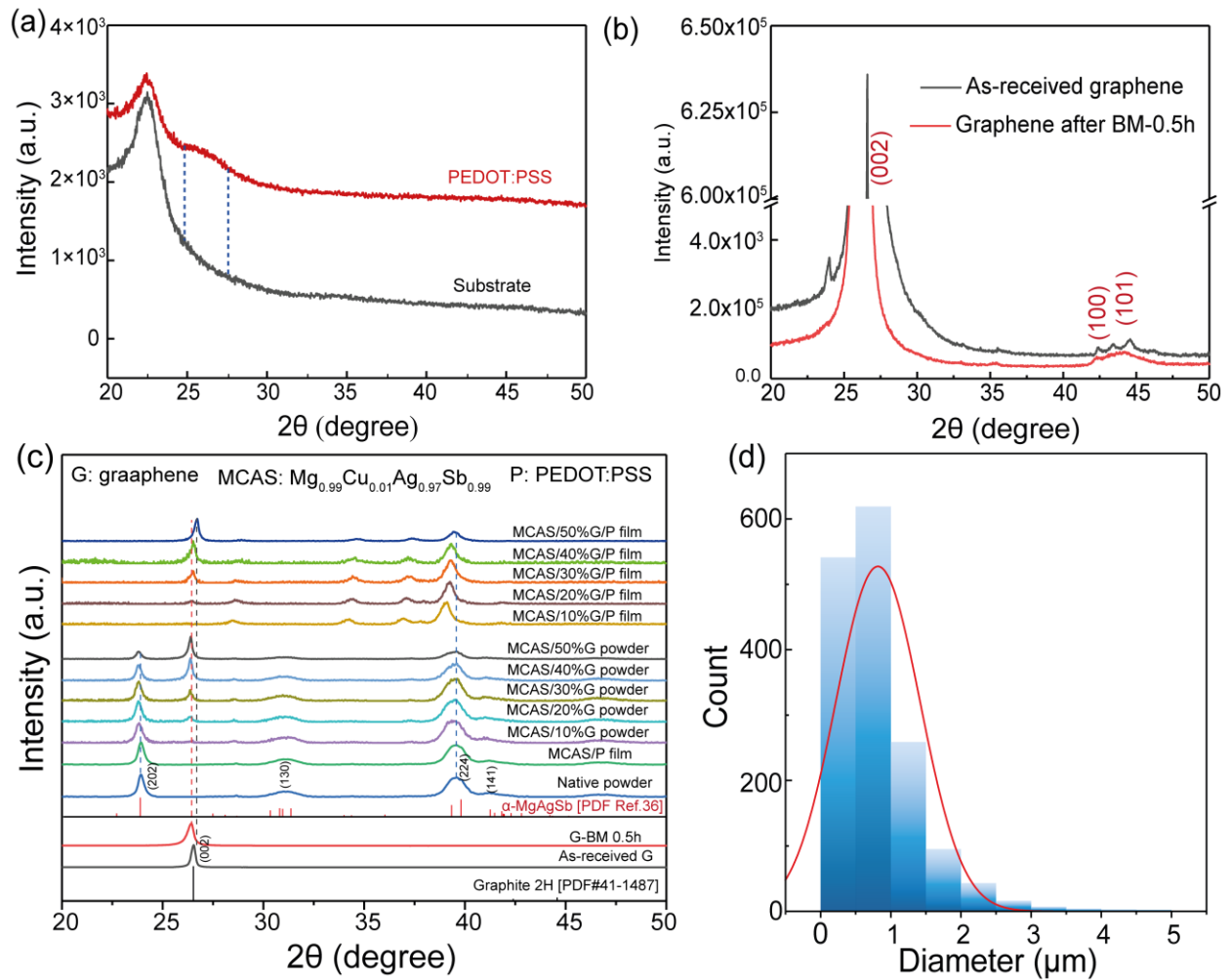


Figure 4.4 The XRD patterns for (a) PEDOT:PSS, PTFE substrate, (b) graphene before and after ball milling, (c) G before and after ball milling, MCAS powder, MACS/x wt% G powder, and MACS/x wt% G/P films (x = 10, 20, 30, 40, 50); (d) size distribution of the MACS particle.

The XRD patterns of PTFE substrate, PEDOT:PSS and graphene before and after ball milling (BM) are shown in **Figure 4.4 (a)** and **(b)**, respectively. The broaden peak between dashed lines in **Figure 4.4a** shows the amorphous crystal structure of pure PEDOT:PSS film on the PTFE substrate. **Figure 4.4b** shows the XRD pattern of graphene before and after ball milling (BM). Compared to the XRD pattern of the G, the wider full-widths at half maximums (FWHMs) and left-shifting of (002) peak was observed in the pattern of G BM-0.5 hours. According to the Scherrer formula,

$$d = \frac{K\lambda}{\beta \cos\theta'}$$

where d is crystal domain size, K is a constant generally taken as 0.9, $\lambda = 0.15406$ nm is the wavelength used, β corresponds to the full widths at half-maximums (FWHMs) in radians which is always used to estimate the crystallite size, and θ is the half of corresponding peak angle. Thus, FWHMs for graphene before and after ball milling calculated based on the (002) reflection plane are 0.268° and 0.472° , respectively, indicating that the BM process not only reduces the size of graphene nanoplate but also is helpful to increase its interplanar spacing. In **Figure 4.4c**, all peaks of native MCAS powder are indexed to the crystal structure of the α -MgAgSb, which is consistent with the previous report[36,40,53]. Only the diffraction peaks corresponding to the (202), (130), (224), and (141) planes are detected due to the reduced crystallite size after ball milling. As shown in **Figure 4.4d**, the size of obtained MCAS particle mainly distributes at 1 μm , and has an overall size distribution in the range of 0 ~ 5 μm . The real chemical composition of the native MCAS powder determined by EDS point-composition analysis is in good agreement with the nominal composition as shown in **Figure 4.5**. In the case of hybrid powder and films (**Figure 4.4c**), except for the peaks contributed by the strong graphite-2H phase, all peaks are consistent with native powder. Besides, the (202) diffraction peak of MCAS disappears in the all hybrid films indicating that the MCAS grains prefer growing along the (224) orientation. The FWHMs of the (224) characteristic peak of hybrid film are reduced as compared to the peaks in the corresponding hybrid powder demonstrating the increased crystallite size of MCAS after hot pressing (FWHMs = 0.989° and 0.635° for MCAS/40 wt% G powder and MCAS/40 wt% G/P film, respectively). In comparison, the peak (224) around $2\theta = 40^\circ$ of the hybrid film shifted towards the lower angle for the sample with 10 wt% graphene as compared to the corresponding hybrid powder. The origin of this shift is most likely due to the residual tensile stress of MCAS powder after the hot pressing process. Also, the narrow FWHMs indicate that the crystallite size of the MCAS is increased after the hot pressing. Moreover, the peak (224) shifted towards the higher angle with increasing graphene content, speculating that the graphene wraps on the surface of MCAS particles and impede the growth of MCAS under hot pressing. No PEDOT:PSS peak are detected in the hybrid film because of the strong peak intensity of MCAS and G.

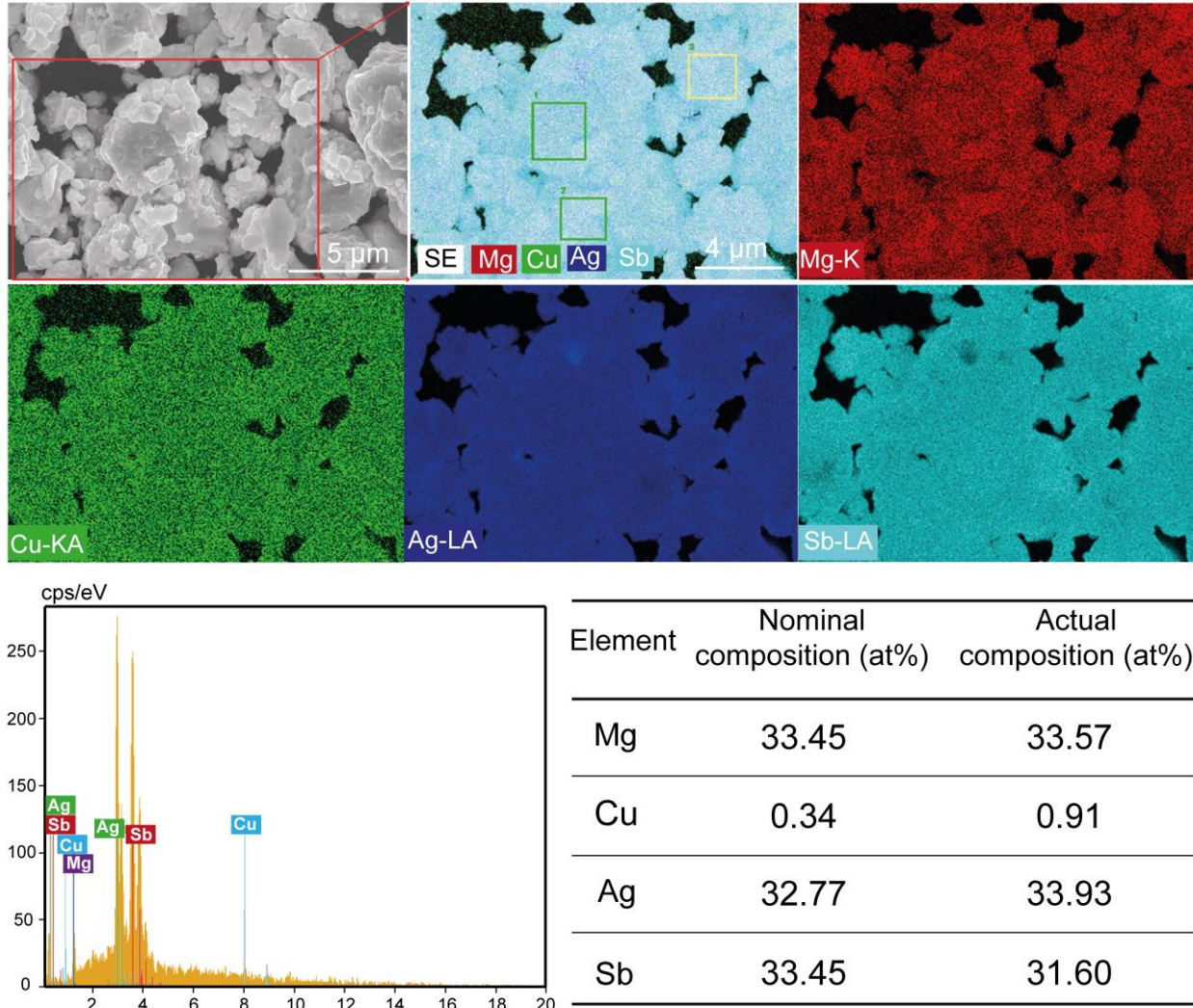


Figure 4.5. EDS analysis of the native MCAS powder and its point-composition analysis

Raman spectroscopy shown in **Figure 4.6** further confirms the presence of graphene. Raman spectra for the G before and after ball milling as well as in the hybrid powder show typical peaks at about 1350, 1580, and 2700 cm^{-1} , which corresponds to the D band, G band and 2D band of graphene, respectively. Generally, the structural defects of graphene are related to the intensity ratio of D band to G band (I_D/I_G) in Raman spectroscopy, where a higher ratio corresponds to the higher defect density of graphene structure. Here, I_D/I_G ratio of G before and after BM increases from 0.622 to 0.681 due to the damage of structure and reduction of crystallite size of graphene[81,82]. However, the I_D/I_G ratio in the hybrid powder decreases with the wt% increase of graphene, suggesting that the ball milling process brought less damage to the integrity of graphene in the hybrid powder. The ratio of I_{2D}/I_G is used to estimate the layers of graphene[83]. Compared to the as-received G, the intensity ratio of the I_{2D}/I_G decreases from 0.784 to 0.772 after BM-0.5 h, which keeps decreasing trend in the hybrid powders (**Table 4.1**), indicating the existence of multiple graphene layers[81].

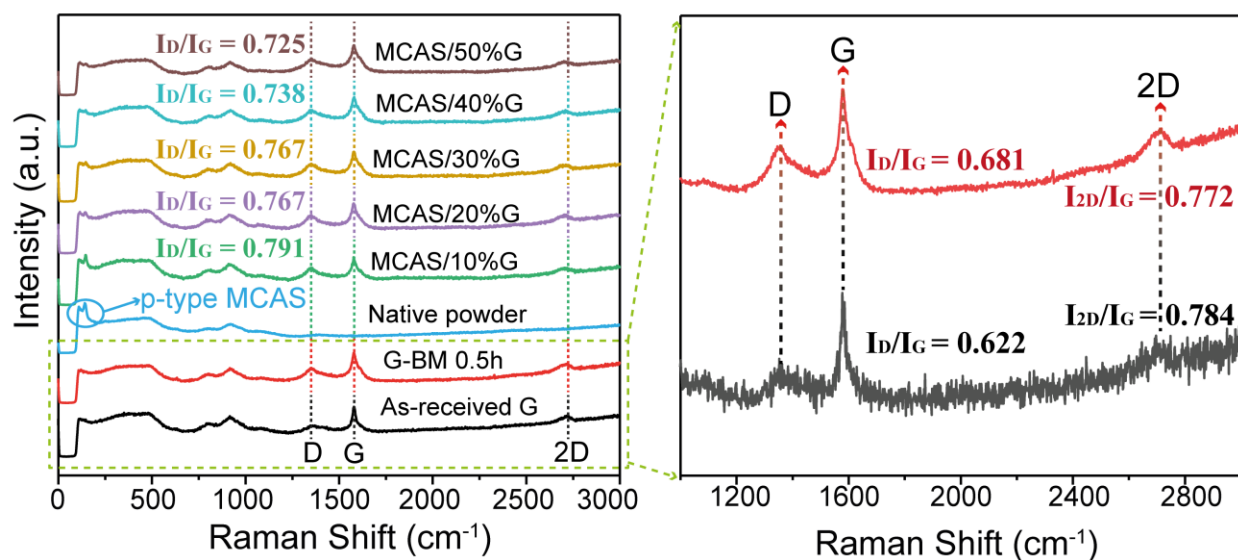


Figure 4.6 Raman spectra of G and MACS/x wt% G powder (x=10, 20, 30, 40, 50).

Table 4.1 Raman data for graphene (G) before and after ball milling and hybrid with $Mg_{0.99}Cu_{0.01}Ag_{0.97}Sb_{0.99}$ (MCAS) powder

Sample	Raman shift(cm^{-1})			Intensity ratio
	D	G	2D	I_{2D}/I_G
MCAS/10%G	1353.8	1580.3	2706.2	0.816
MCAS/20%G	1352.1	1577.1	2707.6	0.767
MCAS/30%G	1352.1	1578.7	2710.4	0.743
MCAS/40%G	1355.4	1580.4	2711.8	0.728
MCAS/50%G	1355.4	1578.8	2714.6	0.666

The scanning electron microscope (SEM) images in **Figure 4.7** show the microstructures of hybrid films formed at different fabrication steps. **Figure 4.7(a)** shows the microstructure of native MCAS powder, in which the particles are randomly distributed and connect with each other by the way of “point to point”. Although the boundary of particles becomes blurry and porosity is reduced after hot pressing at 100 °C under a pressure of 40 MPa (**Figure 4.7b**), the gaps can still be observed in the hybrid film. Therefore, graphene is intercalated to wrap the particles and form 3D conductive paths for carriers, as schematically illustrated in **Figure 4.7(c)**, which is partially supported by the SEM-EDS result. As shown in **Figure 4.8**, the C element mapping indicates that the introduced graphene not only wrapped

on the MCAS particles but also existed in the gap bridging the particles. In such a structure, the graphene surface acts as a connecting point between the particles, which provides a conductive path that may greatly promote carrier mobility, proved by the Hall measurement result and discussed in the TE properties part. The SEM image of MCAS/40 wt% graphene film is shown in **Figure 4.7(d)**, which reveals the formation of a dense film. However, the presence of individual MCAS particles (red circle) and clear interfaces (red arrows) of graphene agglomerated is observed, which can be detrimental to the transport of carriers and may lead to a poor σ [58]. In contrast, the MCAS/G/P film shows the homogenous distribution of graphene, and no clear graphene interfaces are observed, which is ascribed to the π - π interaction between graphene and PEDOT:PSS, which is further proved by C 1s spectra in XPS measurement[84]. The stacked graphene nanoplates in the hybrid binary film interact with each other or with particles through the van der Waals force[77]. However, after drop-casting the PEDOT:PSS, the greater π - π interaction between graphene and PEDOT:PSS makes the graphene nanoplates redistribute more homogeneously in the matrix (**Figure 4.7e**)[58,84]. The elemental distribution and homogeneity of the pure powder and ternary hybrid film are further investigated by the EDS (**Figure 4.9**). The results show that all the elements are homogeneously distributed throughout the sample and graphene homogeneously wraps the particles.

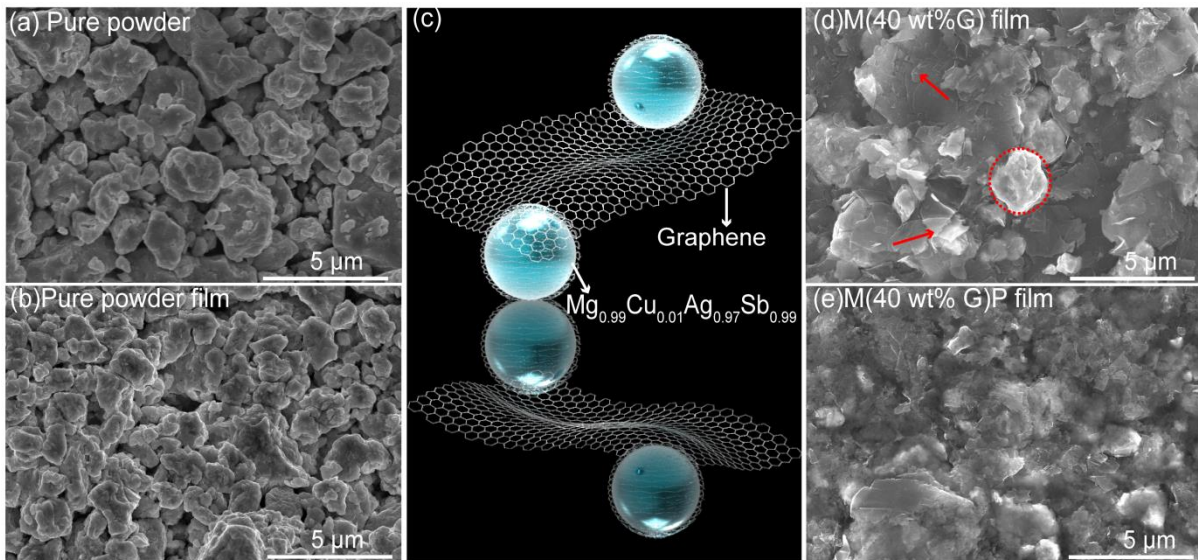


Figure 4.7 SEM images of (a) native MCAS powder; (b) MCAS powder after hot press; (c) schematic illustration of the interaction between MCAS particle and graphene; (d) MCAS/40 wt% G film (e) MCAS/40 wt% G/P film. The ternary film characterized here is constituted by 200 mg mixed powder and 500 μ L PEDOT:PSS.

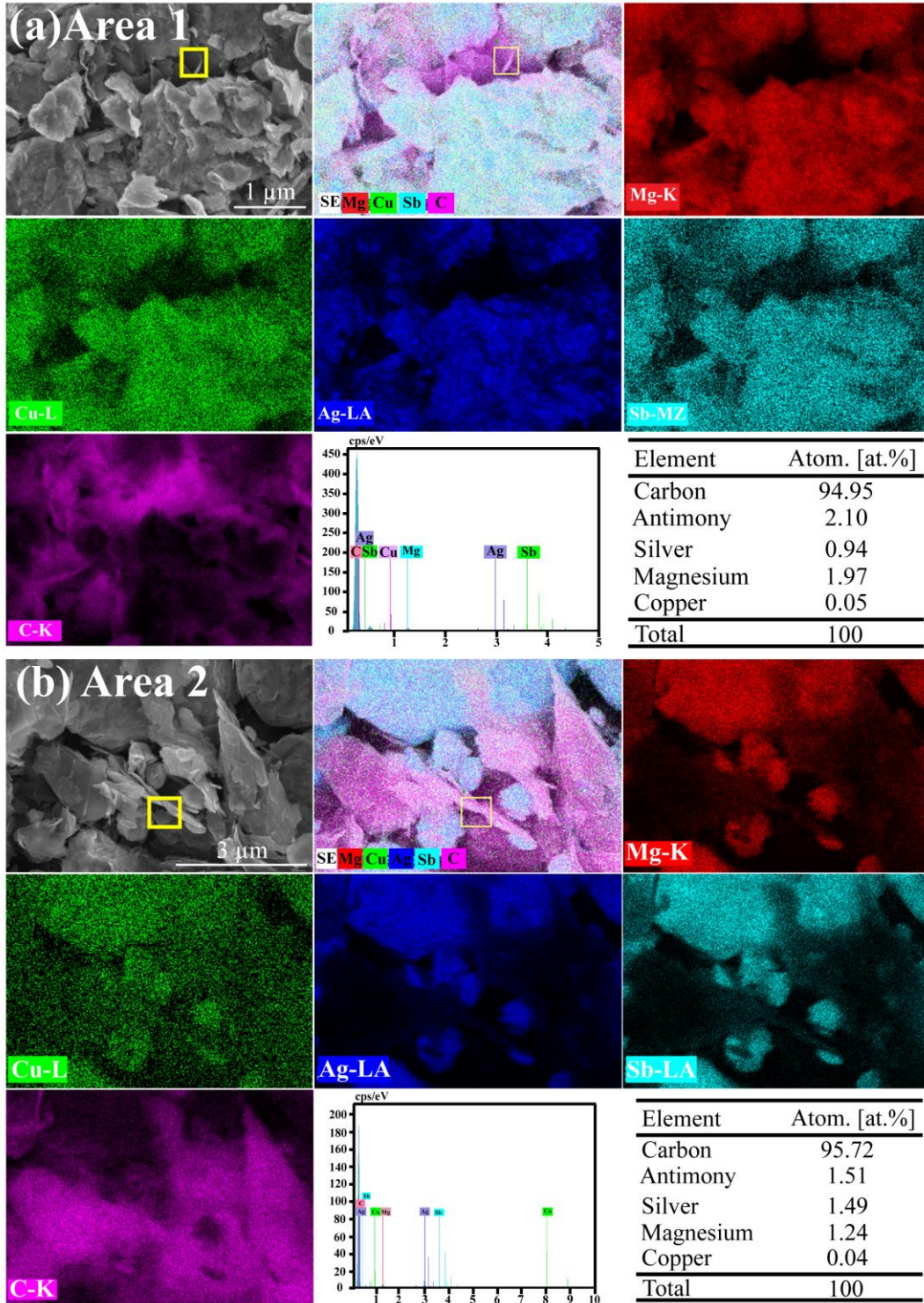


Figure 4.8. (a) and (b) SEM-EDS images of different areas of MCAS/40 wt% G powder and the corresponding point-composition analysis

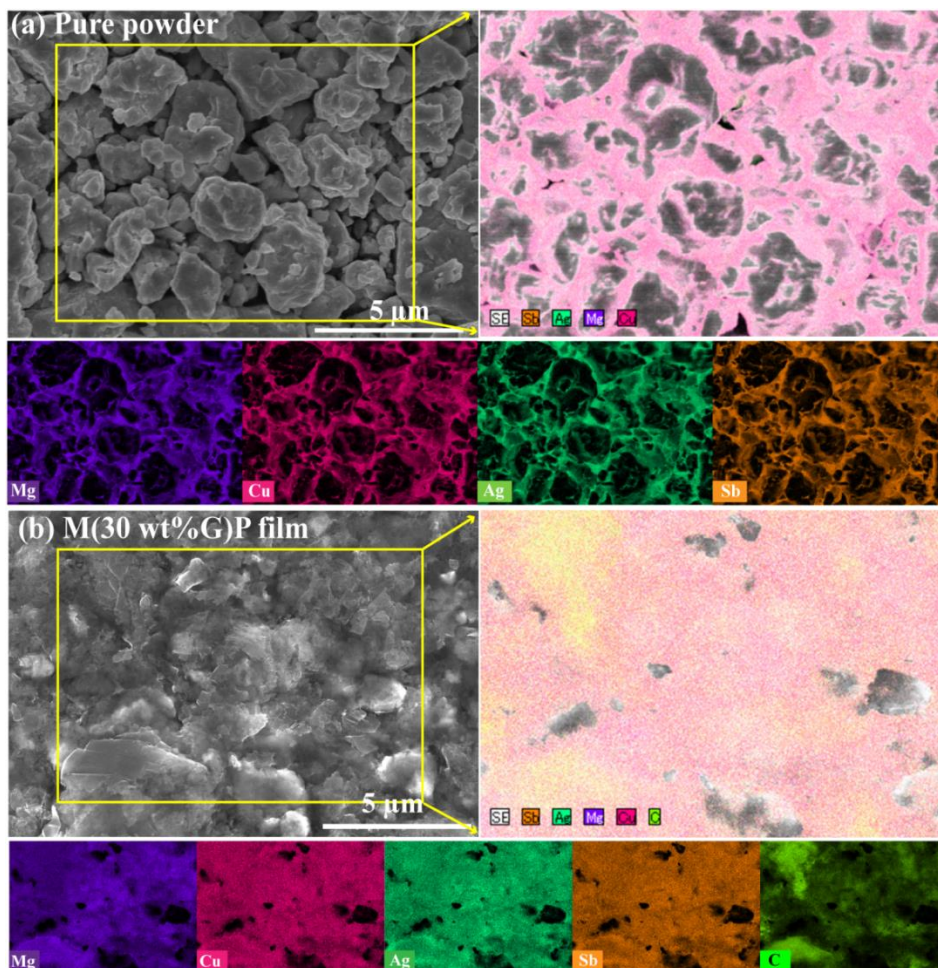


Figure 4.9 The comparison of elemental distributions determined by energy dispersive X-ray spectroscopy (EDX) between pure powder (a) and M(40 wt% G)P hybrid film (b)

Figure 4.10(a) shows XPS survey spectra of G before and after BM, MCAS, and MCAS/40 wt%G hybrid powder as well as MCAS/40 wt%G/P films with different MCAS/G mass loading (79.1 wt% and 88.3 wt%, respectively). The spectra of G before and after BM keep consistent binding energy (BE) of C 1s and O 1s, suggesting that the ball milling process does not influence the element composition of graphene. The C 1s was detected in all hybrid samples indicating the inclusion of graphene in all hybrid samples. Note, it is speculated that the O 1s is contributed by the O₂ absorbed on the surface of the samples because the XRD results (**Figure 4.4c**) indicate the graphite 2H phase of both graphene before and after ball milling samples[85,86]. The spectrum of native MCAS powder confirms the presence of Mg, Cu, Ag, and Sb of native powder. In contrast, the S 2p belonging to PEDOT:PSS was only detected in the MCAS/G/P hybrid films.

Figure 4.10(b, c) shows the C 1s, S 2p core level spectra of the samples. In C 1s spectra, except the C-C group (at ~284.5 eV) belonging to graphene, it is observed that the characteristic C-O (~285.9 eV) and C=O (~287.3 eV) group raised by PEDOT:PSS[87,88]. In addition, the strong π - π interaction between graphene and PEDOT:PSS contributes

to the slightly left-shifting C-C peak in the hybrid films[89]. The similar peaks ratio in the S 2p spectra suggests the PEDOT:PSS is stable in the process of film fabrication.

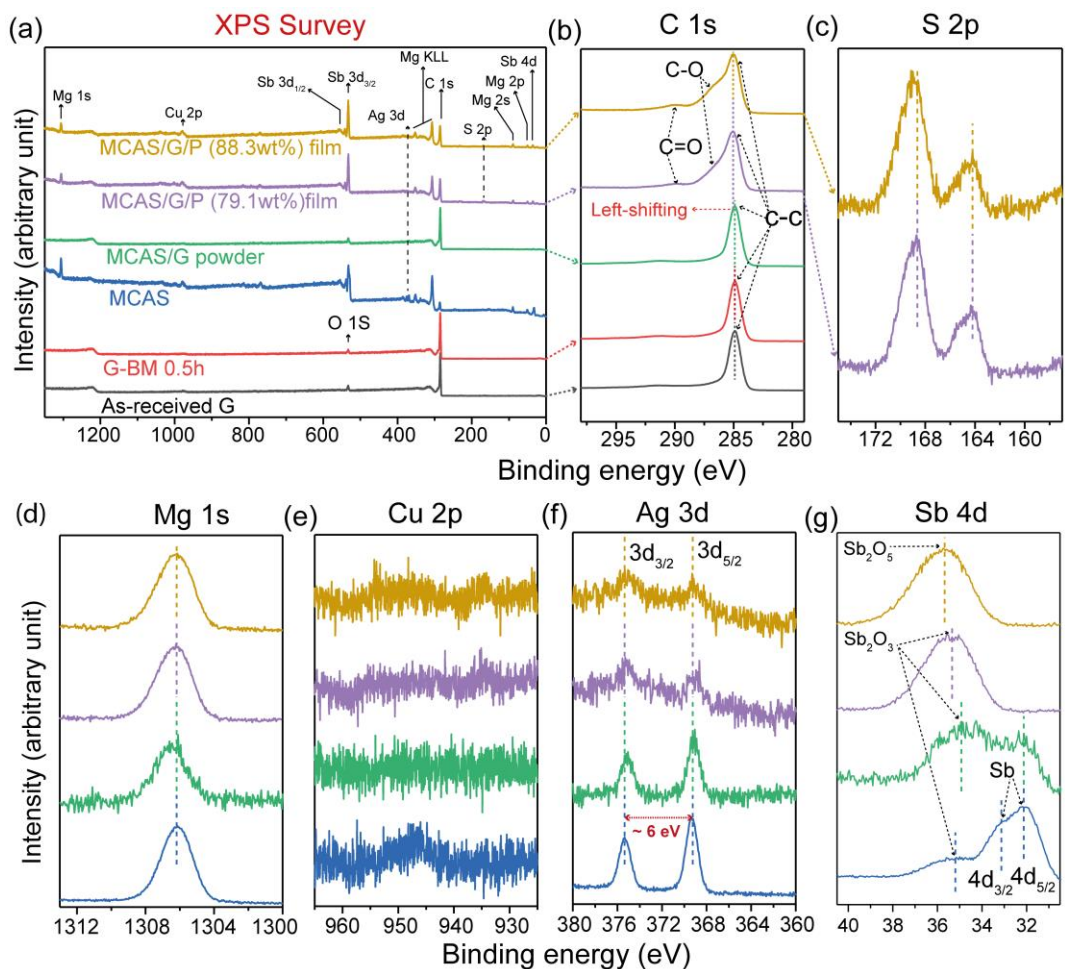


Figure 4.10. (a) XPS survey spectra of pure G, G BM-0.5h, MCAS powder, MCAS/G powder, MCAS/G/P film at 79.1 wt% and MCAS/G/P film at 88.3 wt%. All the spectra have been staggered vertically for clarity of presentation. High resolution (b) C 1s, (c) S 2p, (d) Mg 1s, (e) Cu 2p, (f) Ag 3d, and (g) Sb 4d spectra of MCAS and MCAS/40 wt%G hybrid powder as well as MCAS/G/P films.

Mg 1s, Cu 2p, Ag 3d, and Sb 4d core level spectra were shown in **Figure 4.10(d-g)**. No appreciable change in the BE and line shape of core levels were observed excepting the Sb 4d spectra. The peak position at ~ 1306.2 eV in the Mg 1s spectra implies the Mg^{2+} oxidation state (1305.0 eV) on the surface of MCAS alloy. In contrast, the detected peaks for Cu were too weak to identify the BE position (**Figure 4.10e**). In the spectra of Ag 3d, the two peaks at 369.4 eV and 375.4 eV correspond to Ag $3d_{3/2}$ (368.3 eV) and Ag $3d_{5/2}$ (374.3 eV), and the value of spin-orbit splitting is calculated to be ~ 6 eV, which implies that the Ag ion is in the +1 oxidation state. In comparison, the signal intensity of Ag 3d gradually decreases from native powder to hybrid powder to hybrid films, proving that the Ag signal of MCAS was weakened by the layers of graphene in the hybrid powder and graphene with PEDOT:PSS in the hybrid,

respectively, which is also in accordance with its atomic distribution (**Table 4.2**). From the spectra of Sb 4d, it is known that the part of Sb (pure Sb 4d_{5/2} at 32.1 eV, 4d_{3/2} at 33.3 eV) is oxidized state (4d_{5/2} at 34.56 eV for Sb₂O₃, 4d_{3/2} at 35.74 eV for Sb₂O₅) on the surface of MCAS powder. Compared with the MCAS powder, the oxidation of Sb is serious on the surface of hybrid powder even in the hybrid films. Moreover, the BE position all the peaks measured in this study slightly move to the higher BE position compared to the corresponding standard position (all BE position mentioned in the brackets was obtained from the Handbook[90]), indicating that the element states of MCAS are contributed by both of oxidation and interaction among elements. Nevertheless, combining the XRD results (**Figure 4.4c**), it concludes that the oxidation amount of samples is negligible because no impurity phase was detected by XRD.

Table 4.2 XPS atomic % of Mg, Cu, Ag, and Sb attributed to the surface of samples

	Atomic %			
	Mg 1s	Cu 2p	Ag 3d	Sb 4d
MCAS	68.12	1.01	3.31	27.55
MCAS/G powder	0.54	0.05	0.07	0.33
MCAS/G/P (79.1 wt%) film	6.55	0	0.01	2.04
MCAS/G/P (88.3 wt%) film	7.54	0.25	0.04	2.52

To optimize the graphene content in the hybrid film, the electrical properties σ , S , and PF of hybrid films at room temperature as a function of graphene content are shown in **Figure 4.11a**. The σ of the hybrid film increases slowly with the graphene content up to 30 wt%, then it increases abruptly at 40 wt% and decreases at 50 wt% (**Figure 4.11a**). The σ value increases from 12 S cm⁻¹ for 0 wt% hybrid film to a maximum of 933 S cm⁻¹ for the 40 wt% hybrid film. The optimization of graphene content leads to an increase in the σ ($\sigma = ne\mu$), which is mainly attributed to either increase in concentration (n) or the mobility (μ) of the hybrid films. **Figure 4.11b** shows the n and μ of the hybrid films measured at room temperature. As the graphene content varies from 0 wt% to 50 wt%, the n value increases from $\sim 5 \times 10^{17}$ cm⁻³ (0 wt%) to $\sim 4.5 \times 10^{20}$ cm⁻³ (50 wt%), which is most likely a result of graphene that introduces additional carriers into the matrix.[91-93] Moreover, the μ value increases from ~ 1 cm² V⁻¹ s⁻¹ (0 wt %) to ~ 5 cm² V⁻¹ s⁻¹ (40 wt%) because of the reduced void volume fraction between matrix particles by the addition of graphene content. However, the decreased of both μ and σ for the 50 wt% graphene sample is due to the segregation of graphene nanoplates at the particle boundaries, creating new microstructural interfaces and providing extra boundaries.[58,94]

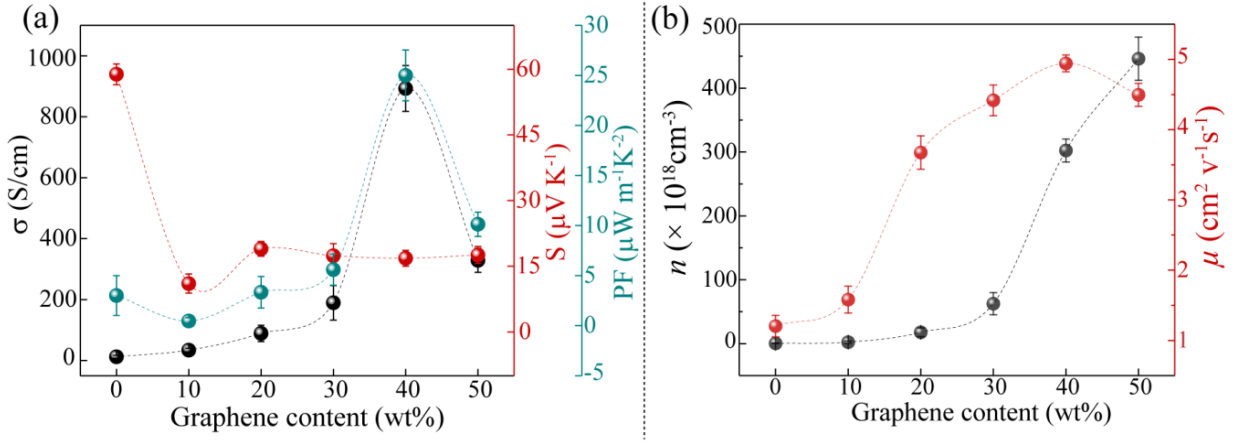


Figure 4.11 TE properties of hybrid film as a function of graphene content by hybrid 200 mg mixed powder with 500 μL PEDOT:PSS: (a) σ , S , and PF ; (b) carrier concentration (n) and mobility (μ)

The positive Seebeck coefficients at room temperature for all the hybrid films show that the majority of carriers are the holes (**Figure 4.11a**). The S decreases significantly with an increase of graphene content up to 10 wt%, whereas it shows similar S values with further increase of graphene content. The S follows the $n^{-2/3}$ dependence according to the Mott's formula,[95] i.e., expressed as

$$S = \frac{8\pi^2 \kappa_B^2}{3eh^2} m^* T \left(\frac{\pi}{3n}\right)^{2/3} \quad (4.1)$$

where κ_B , e , h , m^* , and n are the Boltzmann constant, the carrier charge, Planck's constant, the effective mass, and the carrier concentration, respectively. The S value of hybrid film decreases from $\sim 60 \mu\text{V K}^{-1}$ (0 wt%) to $\sim 15 \mu\text{V K}^{-1}$ (10 wt%), which is owing to the increase of n from $5 \times 10^{17} \text{ cm}^{-3}$ (0 wt%) to $\sim 2 \times 10^{18} \text{ cm}^{-3}$ (10 wt%). The S value of $\sim 15 \mu\text{V K}^{-1}$ is observed for all the hybrid films (10 wt% – 50 wt% of graphene). This result is most likely ascribed to the energy filtering effect,[58,96] where n increases and S is almost invariant. As a result of optimum graphene content at 40 wt%, σ of $\sim 933 \text{ S cm}^{-1}$ and S of $\sim 15 \mu\text{V K}^{-1}$, leads to a maximum power factor of $25 \mu\text{W m}^{-1} \text{ K}^{-2}$ at room temperature, which is 8 times higher than the binary film with 0 wt% graphene (**Figure 4.11a**).

We have successfully demonstrated the preparation of crack free hybrid film with good TE properties. However, mechanical flexibility is essential for the social implementation of hybrid film TE devices. Therefore, the influence of hybrid mass fraction on both TE properties and mechanical flexibility of the ternary hybrid film is further investigated.

Figure 4.12(a) shows the σ , S , and PF of hybrid films as a function of MCAS/40 wt% G mass fraction. The σ increases with the mass fraction whereas the S is almost invariant, leading to the high PF with a similar trend as σ . The increase of σ from 258 S cm^{-1} (79.1 wt%) to 922 S cm^{-1} (93.8 wt%) is mainly due to the increase of μ . **Figure 4.12(b)** shows similar n values whereas the μ increases with varying mass fraction. The μ increases from $\sim 1 \text{ cm}^2 \text{ V}^{-1} \text{ s}^{-1}$ (79.1 wt%) to $\sim 3 \text{ cm}^2 \text{ V}^{-1} \text{ s}^{-1}$ (93.8 wt%), whereas the n value is $\sim 0.5 \times 10^{20} \text{ cm}^{-3}$ for all the hybrid films. As a

combined effect of high σ and moderate S , a maximum PF ($S^2\sigma$) of $31 \mu\text{W m}^{-1} \text{K}^{-2}$ is obtained for the 93.8 wt% mass fraction hybrid film.

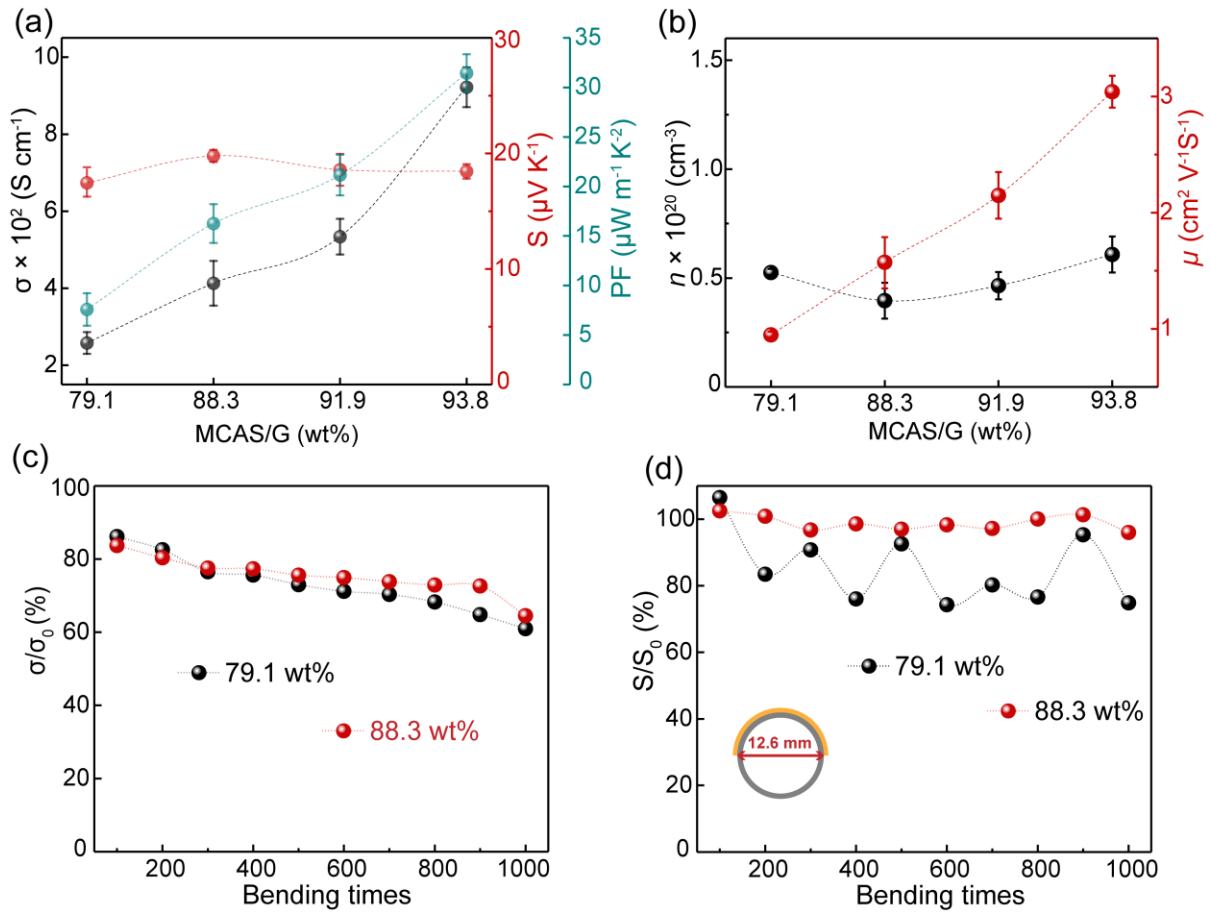


Figure 4.12 (a) σ , S , and PF of the hybrid films as a function of MCAS/G mass fraction; (b) the evolution of carrier concentration and mobility with the mass fraction varying; (c) the variation of σ and (d) S of the hybrid films loading with different MCAS/G mass fraction as a function of bending times.

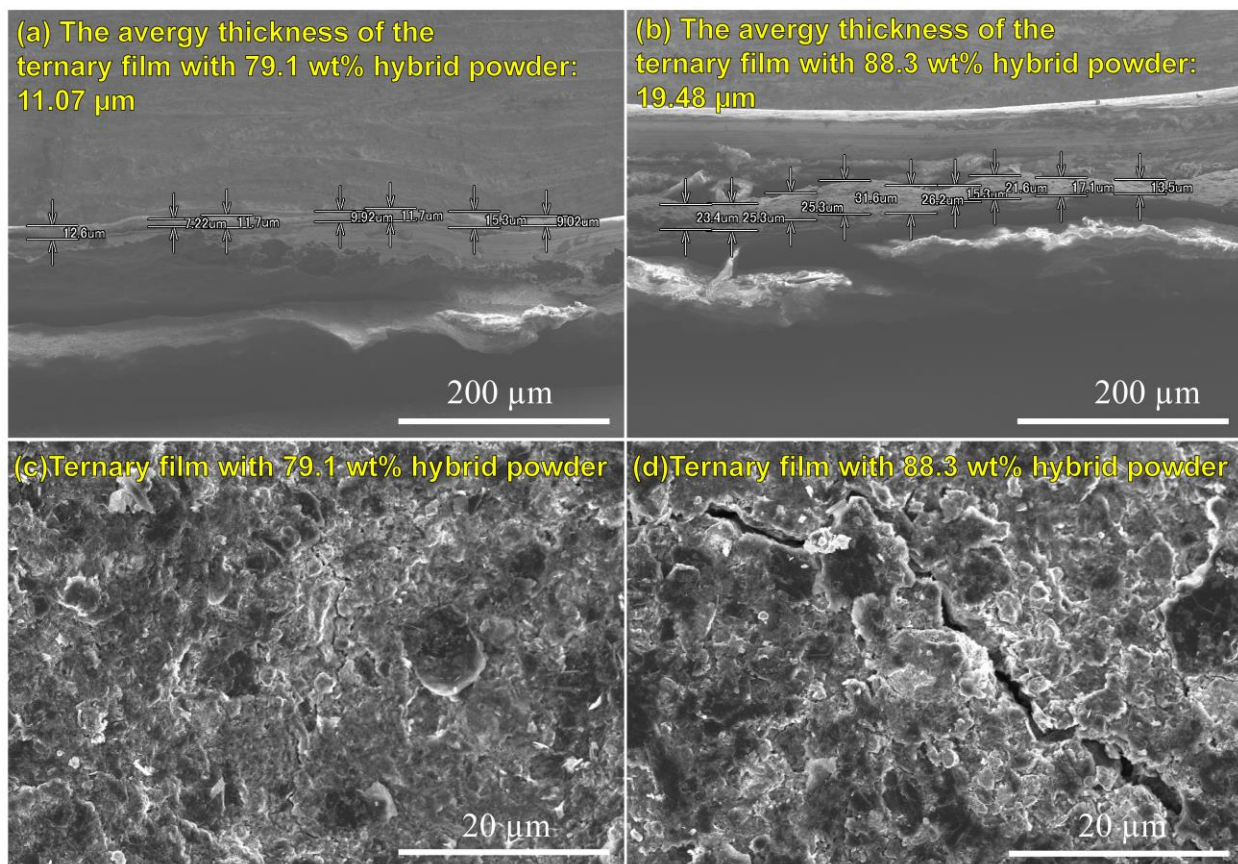


Figure 4.13 (a) and (b) are the thickness of ternary hybrid film with 79.1 wt% and 88.3 wt% hybrid powder, respectively; (c) and (d) are the surface microstructure of corresponding ternary film after 1000 bending tests.

Although the mobility shows the unsaturated trend in the mass fraction range studied, the mechanical bending tests confirm that 88.3 wt% mass fraction is optimum to get a hybrid film with the required flexibility. **Figure 4.12** (c) and (d) show the σ and S as a function of bending times at 79.1 wt% and 88.3 wt% mass fraction. The bending tests are performed by applying the hybrid film around a glass rod with a diameter of 12.6 mm. Within 1000 bending times, the σ of both films (79.1 wt% and 88.3 wt%) shows a similar evolving trend and has a slight decrease in σ (retaining 70.8% at 79.1 wt% and 77% at 88.3 wt% after 1000 bending times). In particular, the film at 88.3 wt% mass fraction shows a relative obvious decrease trend from 900 to 1000 bending times compared to that of the film at 79.1 wt%, indicating the flexibility of the hybrid films at higher mass fraction is easily sacrificed with the increasing of bending times. As shown in **Figure 4.13** (a and b), the thickness of the hybrid film increased with the increase of hybrid powder content. Consequently, the hybrid film with higher mass loading (88.3 wt%) demonstrates the bigger crack (**Figure 4.13** c and d), leading to a more obvious

decrease of σ at higher bending times. In contrast, the S of film at 88.3 wt% is invariant as the function of bending time in comparison to the S at 79.1 wt%. This result shows a significant variation and is possibly caused by the hybrid ratio of three components (inorganic TE material, PEDOT:PSS, and graphene). The hybrid film is expected to be detrimental for TE properties at different areas and bending times with lower mass fraction, therefore, the resultant S is obtained by their respective S ratio in the hybrid film. However, with the increase of mass fraction, the S of an inorganic material part may become dominant, so that the hybrid film at 88.3 wt% shows the similar S value with increasing bending times. The σ and S evolution as a function of bending times of the hybrid films at 91.9 wt% and 93.8 wt% are not obtained because the films are seriously damaged during the first 100 times bending tests. The electrical conductivity of the hybrid film in the present work is comparable with reported data, however, it is less flexible in comparison to the hybrid films fabricated by the nanowire based inorganic components[97-100], which mainly resulted from the “point to point” connection way of inorganic particles.

4.5 Summary

We successfully demonstrated a facile method for the fabrication of crack free *p*-type flexible $\text{Mg}_{0.99}\text{Cu}_{0.01}\text{Ag}_{0.97}\text{Sb}_{0.99}$ /graphene/PEDOT:PSS hybrid film. The electrical properties of the TE films were optimized by varying the graphene content. The TE film with the optimized graphene content (40 wt%) showed a maximum electrical conductivity of 933 S cm^{-1} and power factor of $25 \mu\text{W m}^{-1} \text{ K}^{-2}$ at room temperature. The enhanced *PF* of the hybrid film at 40 wt% graphene results from the optimized conductive path in the $\text{Mg}_{0.99}\text{Cu}_{0.01}\text{Ag}_{0.97}\text{Sb}_{0.99}$, which not only enhanced the σ but also endow the hybrid film with excellent flexibility. Moreover, the mechanical bending tests confirmed that the σ and S of the hybrid film were retained more than 75% after the 1000 bending times. This result indicates that there is still room to improve the flexibility and TE properties of $\text{Mg}_{0.99}\text{Cu}_{0.01}\text{Ag}_{0.97}\text{Sb}_{0.99}$ /graphene/PEDOT:PSS hybrid film. However, the present work may facilitate to develop novel high performance thermoelectric materials with flexibility for harvesting the waste heat.

Reference

- [1] L. Li, W.D. Liu, Q. Liu, Z.G. Chen, *Adv. Funct. Mater.* 32 (2022) 2200548.
- [2] L.E. Bell, *Science* 321 (2008) 1457-1461.
- [3] T. Mori, S. Priya, *MRS Bull.* 43 (2018) 176-180.
- [4] R.A. Kishore, S. Priya, *Materials* 11 (2018) 1433.
- [5] L. Yang, Z.-G. Chen, M.S. Dargusch, J. Zou, *Adv. Energy Mater.* 8 (2018) 1701797.
- [6] S. Hooshmand Zaferani, M. Jafarian, D. Vashaee, R. Ghomashchi, *Energies* 14 (2021) 5646.
- [7] I. Petsagkourakisa, K. Tybrandta, X. Crispin, I. Ohkubo, N. Satoh, T. Mori, *Sci. Technol. Adv. Mater.* 19 (2018) 836-862.
- [8] D. Qu, X. Li, H. Wang, G. Chen, *Adv. Sci.* 6 (2019) 1900584.

- [9] N. Nandihalli, C.-J. Liu, T. Mori, *Nano Energy* 78 (2020) 105186.
- [10] Q. Xu, B. Deng, L. Zhang, S. Lin, Z. Han, Q. Zhou, J. Li, Y. Zhu, F. Jiang, Q. Li, P. Zhang, X. Zhang, G. Chen, W. Liu, *Cell Rep. Physical Science* 3 (2022) 100780.
- [11] J. He, T.M. Tritt, *Science* 357 (2017) 1369.
- [12] T. Mori, *Small* 13 (2017) 1702013.
- [13] X. Zhou, Y. Yan, X. Lu, H. Zhu, X. Han, G. Chen, Z. Ren, *Mater. Today* 21 (2018) 974-988.
- [14] Y. Xiao, L.-D. Zhao, *Science* 367 (2020) 1196-1197.
- [15] Z. Liu, T. Mori, *Nanostructured Bulk Thermoelectric Materials for Energy Harvesting*, In: Wakayama; Yutaka; Ariga; Katsuhiko, *System-Materials Nanoarchitectonics*, (2022) 199-231.
- [16] B. Poudel, Q. Hao, Y. Ma, Y. Lan, A. Minnich, B. Yu, X. Yan, D. Wang, A. Muto, D. Vashaee, X. Chen, J. Liu, M.S. Dresselhaus, G. Chen, Z. Ren, *Science* 320 (2008) 634-638.
- [17] K. Biswas, J. He, I.D. Blum, C.I. Wu, T.P. Hogan, D.N. Seidman, V.P. Dravid, M.G. Kanatzidis, *Nature* 489 (2012) 414-418.
- [18] C. Fu, S. Bai, Y. Liu, Y. Tang, L. Chen, X. Zhao, T. Zhu, *Nat. Commun.* 6 (2015) 8144.
- [19] L.-D. Zhao, G. Tan, S. Hao, J. He, Y. Pei, H. Chi, H. Wang, S. Gong, H. Xu, V.P. Dravid, C. Uher, G.J.S. Snyder, C. Wolverton, M.G. Kanatzidis, *Science* 351 (2016) 141-144.
- [20] A.U. Khan, K. Kobayashi, D.-M. Tang, Y. Yamauchi, K. Hasegawa, M. Mitome, Y. Xue, B. Jiang, K. Tsuchiya, D. Golberg, Y. Bando, T. Mori, *Nano Energy* 31 (2017) 152-159.
- [21] H. Zhu, J. Mao, Z. Feng, J. Sun, Q. Zhu, Z. Liu, D.J. Singh, Y. Wang, Z. Ren, *Science advances* 5 (2019) eaav5813.
- [22] J. Yu, Y. Xing, C. Hu, Z. Huang, Q. Qiu, C. Wang, K. Xia, Z. Wang, S. Bai, X. Zhao, L. Chen, T. Zhu, *Adv. Energy Mater.* 10 (2020) 2000888.
- [23] X. Hu, P. Jood, M. Ohta, M. Kunii, K. Nagase, H. Nishiata, M.G. Kanatzidis, A. Yamamoto, *Energy Environ. Sci.* 9 (2016) 517-529.
- [24] P. Jood, M. Ohta, A. Yamamoto, M.G. Kanatzidis, *Joule* 2 (2018) 1339-1355.
- [25] J.R. Salvador, J.Y. Cho, Z. Ye, J.E. Moczysgemba, A.J. Thompson, J.W. Sharp, J.D. Koenig, R. Maloney, T. Thompson, J. Sakamoto, H. Wang, A.A. Wereszczak, *Phys. Chem. Chem. Phys.* 16 (2014) 12510-12520.
- [26] S. El Oualid, I. Kogut, M. Benyahia, E. Geczi, U. Kruck, F. Kosior, P. Masschelein, C. Candolfi, A. Dauscher, J.D. Koenig, A. Jacquot, T. Caillat, E. Alleno, B. Lenoir, *Adv. Energy Mater.* 11 (2021) 2100580.
- [27] A. Nozariasbmarz, U. Saparamadu, W. Li, H.B. Kang, C. Dettor, H. Zhu, B. Poudel, S. Priya, *J. Power Sources* 493 (2021) 229695.
- [28] Y. Du, J. Xu, B. Paul, P. Eklund, *Appl. Mater. Today* 12 (2018) 366-388.
- [29] Q. Jiang, J. Yang, P. Hing, H. Ye, *Adv. Mater.* 1 (2020) 1038-1054.
- [30] X. Wang, J. Cheng, L. Yin, Z. Zhang, X. Wang, J. Sui, X. Liu, J. Mao, F. Cao, Q. Zhang, *Adv. Funct. Mater.* 32 (2022) 2200307.
- [31] D.W. Ao, W.D. Liu, Y.X. Chen, M. Wei, B. Jabar, F. Li, X.L. Shi, Z.H. Zheng, G.X. Liang, X.H. Zhang, P. Fan, Z.G. Chen, *Adv. Sci.* 9 (2022) e2103547.
- [32] O. Norimasa, T. Chiba, M. Hase, T. Komori, M. Takashiri, *J. Alloys Compd.* 898 (2022) 162889.

- [33] Y. Lei, R. Qi, M. Chen, H. Chen, C. Xing, F. Sui, L. Gu, W. He, Y. Zhang, T. Baba, T. Baba, H. Lin, T. Mori, K. Koumoto, Y. Lin, Z. Zheng, *Adv. Mater.* 34 (2021) 2104786.
- [34] J. Liang, T. Wang, P. Qiu, S. Yang, C. Ming, H. Chen, Q. Song, K. Zhao, T.-R. Wei, D. Ren, Y.-Y. Sun, X. Shi, J. He, L. Chen, *Energy Environ. Sci.* 12 (2019) 2983-2990.
- [35] X. Li, Y. Lu, K. Cai, M. Gao, Y. Li, Z. Wang, M. Wu, P. Wei, W. Zhao, Y. Du, S. Shen, *Chem. Eng. J.* 434 (2022) 134739.
- [36] M.J. Kirkham, A.M. dos Santos, C.J. Rawn, E. Lara-Curzio, J.W. Sharp, A.J. Thompson, *Phys. Rev. B* 85 (2012) 144120.
- [37] H. Zhao, J. Sui, Z. Tang, Y. Lan, Q. Jie, D. Kraemer, K. McEnaney, A. Guloy, G. Chen, Z. Ren, *Nano Energy* 7 (2014) 97-103.
- [38] D. Kraemer, J. Sui, K. McEnaney, H. Zhao, Q. Jie, Z.F. Ren, G. Chen, *Energy Environ. Sci.* 8 (2015) 1299-1308.
- [39] J. Shuai, H.S. Kim, Y. Lan, S. Chen, Y. Liu, H. Zhao, J. Sui, Z. Ren, *Nano Energy* 11 (2015) 640-646.
- [40] J. Sui, J. Shuai, Y. Lan, Y. Liu, R. He, D. Wang, Q. Jie, Z. Ren, *Acta Mater.* 87 (2015) 266-272.
- [41] P. Ying, X. Liu, C. Fu, X. Yue, H. Xie, X. Zhao, W. Zhang, T. Zhu, *Chem. Mater.* 27 (2015) 909-913.
- [42] Z. Liu, H. Geng, J. Mao, J. Shuai, R. He, C. Wang, W. Cai, J. Sui, Z. Ren, *J. Mater. Chem. A* 4 (2016) 16834-16840.
- [43] Z. Liu, J. Shuai, J. Mao, Y. Wang, Z. Wang, W. Cai, J. Sui, Z. Ren, *Acta Mater.* 102 (2016) 17-23.
- [44] Z. Liu, Y. Wang, J. Mao, H. Geng, J. Shuai, Y. Wang, R. He, W. Cai, J. Sui, Z. Ren, *Adv. Energy Mater.* 6 (2016) 1502269.
- [45] Z. Liu, W. Gao, X. Meng, X. Li, J. Mao, Y. Wang, J. Shuai, W. Cai, Z. Ren, J. Sui, *Scripta Mater.* 127 (2017) 72-75.
- [46] Z. Liu, Y. Wang, W. Gao, J. Mao, H. Geng, J. Shuai, W. Cai, J. Sui, Z. Ren, *Nano Energy* 31 (2017) 194-200.
- [47] Z. Liu, Y. Zhang, J. Mao, W. Gao, Y. Wang, J. Shuai, W. Cai, J. Sui, Z. Ren, *Acta Mater.* 128 (2017) 227-234.
- [48] D. Li, H. Zhao, S. Li, B. Wei, J. Shuai, C. Shi, X. Xi, P. Sun, S. Meng, L. Gu, Z. Ren, X. Chen, *Adv. Funct. Mater.* 25 (2015) 6478-6488.
- [49] Naihua Miao, Jian Zhou, B. Sa, Bin Xu, Z. Sun, *Appl. Phys. Lett.* 108 (2016) 213902.
- [50] C. Y. Sheng, H. J. Liu, D. D. Fan, L. Cheng, J. Zhang, J. Wei, J. H. Liang, P. H. Jiang, J. Shi, *J. Appl. Phys.* 119 (2016) 195101.
- [51] J.-F. Wang, X.-N. Fu, X.-D. Zhang, J.-T. Wang, X.-D. Li, Z.-Y. Jiang, *Chin. Phys. B* 25 (2016) 086302.
- [52] P. Ying, X. Li, Y. Wang, J. Yang, C. Fu, W. Zhang, X. Zhao, T. Zhu, *Adv. Funct. Mater.* 27 (2017) 1604145.
- [53] Z. Liu, N. Sato, W. Gao, K. Yubuta, N. Kawamoto, M. Mitome, K. Kurashima, Y. Owada, K. Nagase, C.-H. Lee, J. Yi, K. Tsuchiya, T. Mori, *Joule* 5 (2021) 1196-1208.
- [54] P. Ying, R. He, J. Mao, Q. Zhang, H. Reith, J. Sui, Z. Ren, K. Nielsch, G. Schierning, *Nat. Commun.* 12 (2021) 1121.
- [55] Z. Liu, W. Gao, H. Oshima, K. Nagase, C.H. Lee, T. Mori, *Nat. Commun.* 13 (2022) 1120.
- [56] G. Prunet, F. Pawula, G. Fleury, E. Cloutet, A.J. Robinson, G. Hadziioannou, A. Pakdel, *Mater. Today Phys.* 18 (2021) 100402.
- [57] B. Ni, C. Fu, S. Pan, L. He, Z. Lin, J. Peng, *Chem. Mater.* 34 (2022) 847-853.
- [58] Y. Wang, H. Pang, Q. Guo, N. Tsujii, T. Baba, T. Baba, T. Mori, *ACS Appl. Mater. Interfaces* 13 (2021) 51245-51254.
- [59] D. Yoo, J. Kim, J.H. Kim, *Nano Res.* 7 (2014) 717-730.
- [60] M.N. Gueye, A. Carella, J. Faure-Vincent, R. Demadrille, J.-P. Simonato, *Prog. Mater. Sci.* 108 (2020) 100616.

- [61] W. Li, H. Wang, X. Hu, W. Cai, C. Zhang, M. Wang, Z. Zang, *Solar RRL* 5 (2021) 2000573.
- [62] M. Wang, W. Li, H. Wang, K. Yang, X. Hu, K. Sun, S. Lu, Z. Zang, *Adv. Electron. Mater.* 6 (2020) 2000604.
- [63] M. Wang, H. Wang, W. Li, X. Hu, K. Sun, Z. Zang, *J. Mater. Chem. A* 7 (2019) 26421-26428.
- [64] F. Huang, H. Wu, Y. Cao, *Chem. Soc. Rev.* 39 (2010) 2500-2521.
- [65] M.N. Gueye, A. Carella, R. Demadrille, J.-P. Simonato, *ACS Appl. Mater. Interfaces* 9 (2017) 27250-27256.
- [66] B.D. Paulsen, K. Tybrandt, E. Stavrinidou, J. Rivnay, *Nat. Mater.* 19 (2020) 13-26.
- [67] M. Solazzo, K. Krukiewicz, A. Zhussupbekova, K. Fleischer, M.J. Biggs, M.G. Monaghan, *Journal of Materials Chemistry B* 7 (2019) 4811-4820.
- [68] Z. Fan, J. Ouyang, *Adv. Electron. Mater.* 5 (2019) 1800769.
- [69] X. Hu, K. Zhang, J. Zhang, S. Wang, Y. Qiu, *ACS Appl. Energy Mater.* 1 (2018) 4883-4890.
- [70] D. Ni, H. Song, Y. Chen, K. Cai, *J. Materiomics* 6 (2020) 364-370.
- [71] Y. Du, X. Liu, J. Xu, S.Z. Shen, *Mater. Chem. Front.* 3 (2019) 1328-1334.
- [72] B. Zhang, J. Sun, H.E. Katz, F. Fang, R.L. Opila, *ACS Appl. Mater. Interfaces* 2 (2010) 3170-3178.
- [73] Y. Wang, M. Hong, W.-D. Liu, X.-L. Shi, S.-D. Xu, Q. Sun, H. Gao, S. Lu, J. Zou, Z.-G. Chen, *Chem. Eng. J.* 397 (2020) 125360.
- [74] F. Schedin, A.K. Geim, S.V. Morozov, E.W. Hill, P. Blake, M.I. Katsnelson, K.S. Novoselov, *Nat. Mater.* 6 (2007) 652-655.
- [75] C. Lee, X.W. Wei, J.W. Kysar, J. Hone, *Science* 321 (2008) 385-388.
- [76] A.H. Castro Neto, F. Guinea, N.M.R. Peres, K.S. Novoselov, A.K. Geim, *Rev. Mod. Phys.* 81 (2009) 109-162.
- [77] Y. Liu, N.O. Weiss, X. Duan, H.-C. Cheng, Y. Huang, X. Duan, *Nat. Rev. Mater.* 1 (2016) 1-17.
- [78] M. Alsalama, H. Hamoudi, K.M. Youssef, *J. Alloys Compd.* (2021) 159584.
- [79] K. Ahmad, C. Wan, M.A. Al-Eshaikh, A.N. Kadachi, *Appl. Surf. Sci.* 474 (2019) 2-8.
- [80] P.-a. Zong, X. Chen, Y. Zhu, Z. Liu, Y. Zeng, L. Chen, *J. Mater. Chem. A* 3 (2015) 8643-8649.
- [81] M. Li, H. Gao, J. Liang, S. Gu, W. You, D. Shu, J. Wang, B. Sun, *Mater. Charact.* 140 (2018) 172-178.
- [82] D. Poirier, R. Gauvin, R.A.L. Drew, *Composites Part A: Applied Science and Manufacturing* 40 (2009) 1482-1489.
- [83] F. Chen, J. Ying, Y. Wang, S. Du, Z. Liu, Q. Huang, *Carbon* 96 (2016) 836-842.
- [84] E. Bilotti, O. Fenwick, B.C. Schroeder, M. Baxendale, P. Taroni-Junior, T. Degoussée, Z. Liu, *Comprehensive Composite Materials II* 6 (2018) 408-430.
- [85] Z.-J. Fan, W. Kai, J. Yan, T. Wei, L.-J. Zhi, J. Feng, Y.-m. Ren, L.-P. Song, F. Wei, *ACS nano* 5 (2011) 191-198.
- [86] H.M.A. Hassan, V. Abdelsayed, A.E.R.S. Khder, K.M. AbouZeid, J. Ternner, M.S. El-Shall, S.I. Al-Resayes, A.A. El-Azhary, *J. Mater. Chem.* 19 (2009) 3832.
- [87] G.H. Kim, D.H. Hwang, S.I. Woo, *Physical chemistry chemical physics : PCCP* 14 (2012) 3530-3536.
- [88] D. Yoo, J. Kim, J.H. Kim, *Nano Res* 7 (2014) 717-730.
- [89] Q. Su, S. Pang, V. Alijani, C. Li, X. Feng, K. Müllen, *Adv. Mater.* 21 (2009) 3191-3195.
- [90] J. Chastain, R.C. King Jr, *Perkin-Elmer Corporation* 40 (1992) 221.
- [91] F. Ghahari, H.Y. Xie, T. Taniguchi, K. Watanabe, M.S. Foster, P. Kim, *Phys. Rev. Lett.* 116 (2016) 136802.
- [92] P. Wei, W. Bao, Y. Pu, C.N. Lau, J. Shi, *Phys. Rev. Lett.* 102 (2009) 166808.
- [93] Y.M. Zuev, W. Chang, P. Kim, *Phys. Rev. Lett.* 102 (2009) 096807.

- [94] S.H. Zaferani, R. Ghomashchi, D. Vashae, ACS Appl. Energy Mater. 4 (2021) 3573-3583.
- [95] G.J. Snyder, E.S. Toberer, Complex thermoelectric materials, In: Materials for Sustainable Energy, World Scientific Publishing Co. Pte. Ltd, Singapore, (2010) 101-110.
- [96] J. Choi, J.Y. Lee, S.-S. Lee, C.R. Park, H. Kim, Adv. Energy Mater. 6 (2016) 1502181.
- [97] Y. Lu, Y. Qiu, K. Cai, X. Li, M. Gao, C. Jiang, J. He, Mater. Today Phys. 14 (2020) 100223.
- [98] Y. Lu, Y. Qiu, Q. Jiang, K. Cai, Y. Du, H. Song, M. Gao, C. Huang, J. He, D. Hu, ACS Appl. Mater. Interfaces 10 (2018) 42310-42319.
- [99] Q. Meng, Y. Qiu, K. Cai, Y. Ding, M. Wang, H. Pu, Q. Yao, L. Chen, J. He, ACS Appl Mater Interfaces 11 (2019) 33254-33262.
- [100] Y. Lu, Y. Ding, Y. Qiu, K. Cai, Q. Yao, H. Song, L. Tong, J. He, L. Chen, ACS Appl. Mater. Interfaces 11 (2019) 12819-12829.

Chapter 5 Conclusion and outlook

5.1 Conclusion

We developed the three different hybrid processes for synthesis of $\text{MoS}_2/\text{Bi}_2\text{Te}_3$ composites, flexible $\text{Cu}_{0.98}\text{Zn}_{0.02}\text{FeS}_2/\text{PEDOT:PSS}/\text{graphene}$ and $\text{Mg}_{0.99}\text{Cu}_{0.01}\text{Ag}_{0.97}\text{Sb}_{0.99}/\text{graphene}/\text{PEDOT:PSS}$ hybrid films. By hydrothermal reacting method obtained hexagonal Bi_2Te_3 nanoplates homogeneously covered by 1-T MoS_2 followed by the spark plasma sintering (SPS), the enhanced thermoelectric properties were obtained. The aim of thermoelectric materials with flexibility and Te-free constitutes was achieved by hybrid chalcopyrite and $\text{Mg}_{0.99}\text{Cu}_{0.01}\text{Ag}_{0.97}\text{Sb}_{0.99}$ with conductive polymers.

The synthesis of $\text{MoS}_2/\text{Bi}_2\text{Te}_3$ composites, a series of $\text{Bi}_2\text{Te}_3/\text{X}$ mol% MoS_2 ($X = 0, 25, 50, 75$) bulk nanocomposites have been prepared by hydrothermal reaction followed by reactive Spark Plasma Sintering (SPS). X-ray diffraction analysis (XRD) indicates that the native nanopowders, comprising of $\text{Bi}_2\text{Te}_3/\text{MoS}_2$ heterostructure, are highly reactive during the electric field-assisted sintering by SPS. The nano-sized MoS_2 particles react with the Bi_2Te_3 plates matrix forming a mixed-anion compound $\text{Bi}_2\text{Te}_2\text{S}$ at the interface between the nanoplates. The transport properties characterizations revealed a significant influence of the nanocomposite structure formation on the native electrical conductivity, Seebeck coefficient, and thermal conductivity of the initial Bi_2Te_3 matrix. As a result, enhanced ZT values have been obtained in $\text{Bi}_2\text{Te}_3/25$ mol% MoS_2 over the temperature range of 300 - 475 K induced mainly by a significant increase of the electrical conductivity.

Combining inorganic thermoelectric (TE) materials with conductive polymers is one promising strategy to develop flexible thermoelectric (FTE) films and devices. As most inorganic materials tried up to now in FTE composites are composed of scarce or toxic elements, and furthermore, n-type FTE materials are particularly desired.

The fabrication of flexible n-type TE films, it is combined that the abundant and inexpensive, non-toxic Zn-doped chalcopyrite ($\text{Cu}_{1-x}\text{Zn}_x\text{FeS}_2$, $x = 0.01, 0.02, 0.03$) with a flexible electrical network constituted by poly(3,4-ethylenedioxythiophene) polystyrene sulfonate (PEDOT:PSS) and graphene for n-type FTE films. The hybrid films from the custom-design of binary $\text{Cu}_{1-x}\text{Zn}_x\text{FeS}_2/\text{PEDOT:PSS}$ to optimum-design of ternary $\text{Cu}_{0.98}\text{Zn}_{0.02}\text{FeS}_2/\text{PEDOT:PSS}/\text{graphene}$ are characterized. Compared with the binary film, a 4-fold enhancement on electrical conductivity was observed in the ternary film, leading to a maximum power factor of $\sim 23.7 \mu\text{W m}^{-1}\text{K}^{-2}$. The optimum ternary film could preserve $> 80\%$ of the electrical conductivity after 2000 bending cycles, exhibiting an exceptional flexibility owing to the network constructed by PEDOT:PSS and graphene. A five-leg thermoelectric prototype made of optimum films, generated a voltage of 4.8 mV with a small ΔT of 13°C . Such an evolution of an inexpensive chalcopyrite-based hybrid film with outstanding flexibility exhibits potential for cost sensitive FTE applications.

The fabrication of the flexible $\text{Mg}_{0.99}\text{Cu}_{0.01}\text{Ag}_{0.99}\text{Sb}_{0.97}$ /graphene/PEDOT:PSS (MCAS/G/P) TE film was prepared on a polytetrafluoroethylene (PTFE) substrate. A physical process was developed to resolve the cracking problem during the hybrid process. In this hybrid structure, MCAS particles constitute a matrix, while a conductive network formed by graphene and PEDOT:PSS reduces the interfacial contact resistance between MCAS particles, thereby facilitating carrier transport and in turn enhancing the electrical properties of the hybrid films. The graphene content in MCAS/x wt% G/P hybrid system was optimized by evaluating the TE properties, which reveals that the optimum content of graphene was 40 wt%. Further, the influence of hybrid mass fraction on both TE properties and mechanical flexibility of the ternary hybrid film was systematically investigated. As a result, a maximum power factor (*PF*) of $31 \mu\text{W m}^{-1} \text{K}^{-2}$ was obtained at 93.8 wt% powder ratio. However, mechanical bending tests revealed that the maximum *PF* of $16 \mu\text{W m}^{-1} \text{K}^{-2}$ was obtained for the flexible MCAS/G/P film loading with 88.3 wt% MCAS/G. The hybrid synthesis method proposed in this work may pave the way for a design strategy in the fabrication of novel materials-based flexible TE films and spur the emerging application of new hybrid flexible materials in energy harvesting.

5.2 Outlook

As a green energy material, thermoelectric (TE) materials have attracted increasing attention due to their unique advantages. Polymers have the advantages of abundant resources and simple preparation methods. The study found that organic/inorganic composite materials were prepared by in-situ polymerization of inorganic materials and conductive polymers, and the interface of organic/inorganic composite materials was reasonably designed. Through the interface effect and the synergistic effect between organic and inorganic materials, the performance of the composite TE material can be improved.

The development of wearable electronic devices is increasing the demand for flexible TE devices, and the development of flexible TE devices is becoming promising. Therefore, the fabrication of TE materials not only requires high TE properties but also excellent flexibility. Flexible organic/inorganic composites are prepared by combining flexible materials as substrates with inorganic thermoelectric materials with good thermoelectric properties. It is one of the very promising methods to prepare flexible thermoelectric materials by firmly combining organic and inorganic materials together.

In addition, to improve the output voltage and output power of TE devices, TE materials are required to have the smallest possible internal resistance when assembled into TE devices, and the internal resistance of the devices is not only from the internal resistance of the materials, but also the contact resistance between the thermoelectric legs and the electrode materials is an important source of internal resistance, especially for n-type materials. In the process of device preparation, we can explore the use of ink-jet printing, screen printing and other advanced methods to prepare devices, further optimize the contact interface between electrode material and thermoelectric arm to reduce the generation of internal resistance.

List of Publications

1. “Flexible n-Type Abundant Chalcopyrite/PEDOT:PSS/Graphene Hybrid Film for Thermoelectric Device Utilizing Low-Grade Heat”

Yanan Wang, Hong Pang, Quansheng Guo, Naohito Tsujii, Takahiro Baba, Tetsuya Baba, Takao Mori
ACS Applied Materials & Interfaces 2021, 13, 51245–51254

2. “The Effect of Reactive Electric Field-Assisted Sintering of MoS₂/Bi₂Te₃ Heterostructure on the Phase Integrity of Bi₂Te₃ Matrix and the Thermoelectric Properties”

Yanan Wang, Cédric Bourgès, Ralph Rajamathi, Nethravathi, Michael Rajamathi, Takao Mori
Materials 2022, 15(1), 53.

3. “A facile route of fabricating crack-free Mg_{0.99}Cu_{0.01}Ag_{0.97}Sb_{0.99}/graphene/PEDOT:PSS thermoelectric film on the flexible substrate”

Yanan Wang, Raju chetty, Zihang Liu, Longquan Wang, Takeo Ohsawa, Weihong Gao, and Takao Mori
Journal of Materials Chemistry C, 2022, Advance Article, DOI: 10.1039/D2TC02176E (Paper).